



Simulation of interacting populations in inhomogeneous flows using reduced models

Dissertation

zur Erlangung des akademischen Grades

Doktoringenieur (Dr.-Ing.)

von: M. Sc. Ahmet Alper Öncül
geboren am: 23.02.1979
in: Ankara, Türkei

genehmigt durch die Fakultät für Verfahrens- und Systemtechnik
der Otto-von-Guericke-Universität Magdeburg

Gutachter: Prof. Dr.-Ing. habil. Dominique Thévenin
Prof. Dr.-Ing. Udo Reichl

eingereicht am: 29.06.2010
Promotionskolloquium am: 13.12.2010

Sevgili aileme...

To my dear family...

Danksagung

Mein besonderer Dank gilt Herrn Prof. Dr.-Ing. habil. Dominique Thévenin für die fachlichen Anregungen, seine Diskussionsbereitschaft, die wertvollen Hinweise und die freundliche Unterstützung während meiner Arbeit.

Herrn Prof. Dr.-Ing. Udo Reichl möchte ich für die fachliche Unterstützung und die Bereitschaft zur Übernahme des Zweitgutachtens ebenfalls sehr danken.

Bei Herrn Prof. Dr.-Ing. habil. Kai Sundmacher und Herrn Prof. Dr.-Ing. habil. Andreas Seidel-Morgenstern bedanke ich mich recht herzlich für die Zusammenarbeit und die Unterstützung.

Ich danke auch Herrn Dr.-Ing. Gábor Janiga und Frau Dr. habil. Yvonne Genzel für die hilfreiche Betreuung und die fachlichen Diskussionen.

Bei allen Mitarbeitern des Lehrstuhls für Strömungsmechanik und Strömungstechnik, die mir bei kleinen und großen Problemen stets hilfreich zur Seite standen, möchte ich mich sehr bedanken.

Mein herzlicher Dank gilt meinen Eltern, die mich während meiner Arbeit ständig motiviert und unterstützt haben.

Abstract

Today, applications of Computational Fluid Dynamics (CFD) have a great importance in many engineering fields. This is due to the fact that the sophisticated and realistic numerical techniques employed during the CFD simulations provide powerful predictions. These predictions can not definitely be considered as a substitution for experimental measurements; however, they can be respected as an initial guess and as a complement to experiments for finer analysis.

The aim of the present work was to investigate inhomogeneous flows employing CFD coupled with appropriate population balance models (PBMs) via in-house built user-defined scalars (UDS) and functions (UDF). Therefore, the initial part of the work concentrated on the application of various PBMs in CFD computations. The corresponding initial studies involved various applications in chemical engineering: bulk and microemulsion precipitation of barium sulphate in coaxial pipe mixers and in a semi-batch tank reactor, as well as preferential crystallization of threonine enantiomers in a continuously stirred batch reactor. Various numerical methods and models (such as Eulerian method, turbulence model, etc.) were applied during these initial investigations. Moving mesh techniques for impeller motion such as multiple reference frames (MRF) based on stationary formulation for an initial guess and sliding mesh model (SMM) based on instationary formulation for more realistic predictions were also employed. Furthermore, various hydrodynamic and initial conditions were examined during the computations. The validity of the employed numerical tool was always checked using available experimental data, or in the absence of them, using an analytical solution. All numerical experiences gathered during these initial studies were useful for further investigations.

The most important part of this work concerned a biotechnological application: cultivation of adherent Madin-Darby Canine Kidney (MDCK) cells in a microcarrier system using a disposable bioreactor with wave-induced motion (commercial name: Wave Bioreactor[®]) in 2 L and 20 L cellbag sizes. Firstly, experimental investigations were carried out to characterize the liquid flow conditions in the cellbags. For this purpose, the key parameters like liquid surface level, liquid velocity, liquid and wall shear stress were measured. The measurements showed in particular a low level of shear stress in the Wave Bioreactors[®] compared to classical bioreactors like stirred tanks. This situation represented favorable hydrodynamic conditions for cell cultivation. Afterwards, the flow conditions in the employed cellbags were characterized via CFD simulations for a more detailed analysis. Due to the irregular shape of the flexible cellbags, the numerical domain was realistically reconstructed on the basis of the scanned bioreactor surfaces (under operating conditions) using a laser measuring technique. The unsteady, three-dimensional computations employed the Volume of Fluid (VOF) method, an Eulerian multiphase model which is able to predict correctly the free liquid surface. By this way, the interface between the liquid and gas phases in the cellbags could be clearly described; however, at a higher computational cost. The obtained CFD predictions for the flow conditions in the concerned cellbags were validated since the agreement between the obtained numerical results and the experimental findings was satisfactory. A low level of shear stress was confirmed by the computations. Additionally, it was shown that the obtained flows (under the considered operating conditions) stayed in the laminar regime, confirming gentle mixing conditions, which would result in lower cell damage and consequently higher cell viability. In the last part of the work, computations were carried out to study the cultivation of MDCK cells employing CFD coupled with a two-population balance model (one population for cells in suspension and one for those on microcarriers, with mutual interaction) via UDS and UDF. However, due to the complexity of the three-dimensional configuration, the simulations were finally performed for a zero-dimensional (i.e., homogeneous) case while taking into account the flow conditions (maximum shear stress values) obtained from three-dimensional CFD computations.

Kurzfassung

Heutzutage hat die numerische Strömungsmechanik (Computational Fluid Dynamics, CFD) eine große Bedeutung in vielen Anwendungen des Ingenieurwesens erlangt. Denn die anspruchsvollen numerischen Techniken, die bei den CFD-Simulationen verwendet werden, sind in der Lage, äußerst realistische Schätzungen von Strömungsvorgängen zu liefern. Diese Schätzungen können zwar nicht unbedingt experimentelle Messungen ersetzen. Sie können aber durchaus als Voraussage oder Ergänzung von Messungen für eine verfeinerte Analyse verwendet werden.

Das Ziel dieser Arbeit war die Untersuchung inhomogener Strömungen mit Hilfe von CFD, gekoppelt mit Populationsbilanzmodellen (PBM), welche durch benutzerdefinierte Skalare (UDS) und Funktionen (UDF) implementiert wurden. Der erste Teil dieser Arbeit konzentrierte sich auf die Verwendung verschiedener PBM in CFD-Berechnungen. Die anfänglichen Untersuchungen betrachteten folgende Anwendungen der Verfahrenstechnik: Fällung von BaSO₄ in wässriger Lösung (bzw. in Mikroemulsion) und bevorzugte Kristallisation von Threonin-Enantiomeren in einem kontinuierlichen Rührkessel. Verschiedene numerische Methoden und Modelle (wie z.B. Eulersche Methode, Turbulenzmodell...) wurden während dieser anfänglichen Untersuchungen geprüft. Für die Beschreibung der Impellerrotation wurde die Bewegte-Gitter-Technik (stationäre Formulierung, Multiple Reference Frames - MRF) für eine erste Schätzung und eine instationäre Formulierung (Sliding Mesh Model - SMM) für realistischere Schätzungen verwendet. Außerdem wurden verschiedene hydrodynamische sowie Anfangsbedingungen bei den Berechnungen untersucht. Die Gültigkeit der verwendeten numerischen Methoden wurde soweit möglich größtenteils mittels experimenteller Daten, ansonsten anhand analytischer Lösung geprüft. Alle numerischen Erfahrungen dieser Untersuchungen wurden anschließend auf komplexere Fälle übertragen.

Der wichtigste Teil dieser Arbeit betraf eine biotechnologische Anwendung: die Kultivierung adhärenter tierischer Zellen auf Mikroträgern in Wave-Einwegbioreaktoren (kommerzielle Bezeichnung: Wave Bioreactor[®]) in 2 L und 20 L Beuteln. Zuerst wurden Messungen ausgeführt, um die Fließbedingungen der Flüssigkeit zu charakterisieren. Für diesen Zweck wurden Schlüsselmerkmale wie Flüssigkeitspegel, Geschwindigkeit und Schubspannung gemessen. Die Messungen stellten insbesondere niedrige Schubspannungswerte in den Wave-Bioreaktoren im Vergleich zu klassischen Bioreaktoren wie zum Beispiel Rührkesseln fest. Hiermit wurden günstige hydrodynamische Bedingungen für die Zellkultivierung gezeigt. Danach wurden die Fließbedingungen in den verwendeten Beuteln in einer ausführlicheren Analyse mittels CFD-Simulationen numerisch charakterisiert. Wegen der komplexen Form der flexiblen Beutel wurde die Geometrie mittels einer Lasermesstechnik realistisch rekonstruiert, wobei die Flächen des Bioreaktors unter Betriebsbedingungen anhand eines Lasers gescannt wurden. Die instationären, drei-dimensionalen Berechnungen verwendeten die Volume-of-Fluid (VOF) Methode, ein eulersches Mehrphasenmodell, das für die genaue Beschreibung einer freien Flüssigkeitsoberfläche geeignet ist. Damit konnte die Grenze zwischen Flüssigkeits- und Gasphase verfolgt werden, allerdings mit einer höheren Rechenzeit. Die numerischen Ergebnisse für die Fließbedingungen in den Beuteln wurden anhand vorliegender experimenteller Resultate validiert. Niedrige Schubspannungswerte wurden durch die Simulationen bestätigt. Außerdem wurde festgestellt, dass die berechneten Strömungen unter entsprechenden Betriebsbedingungen laminar bleiben. Hiermit wurden günstige Kultivierungsbedingungen und niedrige Zellschäden bestätigt. Letztendlich wurden Simulationen der Zellkultivierung durchgeführt, wobei CFD mit zwei Populationen (Zellen in der Suspension und auf den Mikroträgern, mit Wechselwirkung) verwendet wurde. Wegen der numerischen Komplexität wurden diese Simulationen für homogene Bedingungen durchgeführt, wobei die maximalen Schubspannungswerte der vollständigen CFD berücksichtigt wurden.

Table of contents

| | |
|--|------------|
| Danksagung | i |
| Abstract | ii |
| Kurzfassung | iii |
| Table of contents | iv |
| Nomenclature | vii |
| 1. Introduction | 1 |
| Part I: Development of methods | 5 |
| 2. Method of moments (MOM): Bulk precipitation of barium sulphate | 7 |
| 2.1 Introduction..... | 7 |
| 2.2 State of the art | 9 |
| 2.3 Reaction kinetics and model equations | 11 |
| 2.4 Numerical and analytical investigations | 13 |
| 2.4.1 <i>Homogeneous (zero-dimensional) analysis</i> | 14 |
| 2.4.2 <i>Coaxial pipe mixers</i> | 17 |
| 2.5 Influence of the activity coefficient | 23 |
| 2.5.1 <i>Numerical investigations</i> | 23 |
| 2.5.2 <i>Results and discussion</i> | 24 |
| 2.6 Conclusions and remarks | 28 |
| 3. Interacting populations: Preferential crystallization of threonine enantiomers | 33 |
| 3.1 Introduction..... | 33 |
| 3.2 State of the art | 34 |
| 3.3 Modelling the crystallization | 35 |
| 3.3.1 <i>Geometries and initial conditions</i> | 36 |
| 3.3.2 <i>Crystallization kinetics and model equations</i> | 36 |
| 3.3.3 <i>Numerical calculations</i> | 39 |
| 3.4 Results and discussion | 40 |
| 3.4.1 <i>Zero-dimensional analysis</i> | 40 |
| 3.4.2 <i>Three-dimensional computation</i> | 43 |
| 3.5 Conclusions and remarks | 45 |
| 4. Model reduction: Microemulsion precipitation of barium sulphate | 47 |
| 4.1 Introduction..... | 47 |
| 4.2 State of the art | 48 |

| | |
|---|-----------|
| 4.3 Experimental setup..... | 49 |
| 4.4 Numerical model..... | 50 |
| 4.4.1 <i>Population balance and reaction kinetics</i> | 51 |
| 4.4.1.1 Model reduction concept..... | 51 |
| 4.4.1.2 Determination of P_{2D}^{eq} | 52 |
| 4.4.1.3 Balance equations..... | 53 |
| 4.4.1.4 Precipitation kinetics | 54 |
| 4.4.2 <i>Numerical computations</i> | 55 |
| 4.4.2.1 Zero-dimensional analysis..... | 55 |
| 4.4.2.2 Three-dimensional CFD simulations..... | 55 |
| 4.5 Results and discussion | 56 |
| 4.5.1 <i>Validation of the reduced model</i> | 56 |
| 4.5.2 <i>Results of CFD simulations</i> | 57 |
| 4.6 Conclusions and remarks | 61 |
| Part II: Application to cell cultivation in bioreactors | 65 |
| 5. Experimental characterization of flow conditions in bioreactors | 67 |
| 5.1 Introduction..... | 67 |
| 5.2 State of the art | 68 |
| 5.3 Materials and methods | 69 |
| 5.3.1 <i>Probe description and calibration</i> | 70 |
| 5.3.2 <i>Measurement procedure</i> | 71 |
| 5.4 Results and discussion | 71 |
| 5.4.1 <i>Liquid level</i> | 72 |
| 5.4.2 <i>Liquid velocity</i> | 74 |
| 5.4.3 <i>Liquid shear stress</i> | 76 |
| 5.4.4 <i>Wall shear stress</i> | 77 |
| 5.4.5 <i>Further hydrodynamic quantities</i> | 78 |
| 5.4.6 <i>Scale-up considerations</i> | 78 |
| 5.5 Conclusions and remarks | 78 |
| 6. CFD simulations for flow characterization in bioreactors | 81 |
| 6.1 Introduction..... | 81 |
| 6.2 State of the art | 82 |
| 6.3 Numerical calculations..... | 83 |
| 6.4 Experimental measurements | 85 |
| 6.5 Results and discussion | 85 |
| 6.5.1 <i>Flow state analysis</i> | 87 |

| | |
|--|------------|
| 6.5.2 Liquid level | 88 |
| 6.5.3 Liquid velocity | 89 |
| 6.5.4 Liquid shear stress | 92 |
| 6.6 Conclusions and remarks | 93 |
| 7. Simulation of animal cell cultivation using reduced PBM..... | 97 |
| 7.1 Introduction..... | 97 |
| 7.2 State of the art | 98 |
| 7.3 Cultivation kinetics and model equations | 99 |
| 7.4 Numerical methods | 101 |
| 7.4.1 MC population | 101 |
| 7.4.2 PBM for animal cells | 102 |
| 7.4.3 Three-dimensional simulation of cultivation | 102 |
| 7.4.4 Zero-dimensional simulation of cultivation | 103 |
| 7.4.5 Optimization of model parameters for cell kinetics in the Wave Bioreactor® | 104 |
| 7.5 Results and discussion | 106 |
| 7.5.1 Evolution of cell concentrations | 106 |
| 7.5.2 Results of parameter optimization | 106 |
| 7.6 Conclusions and remarks | 108 |
| 8. Conclusions and outlook..... | 111 |
| Appendices | 115 |
| A Semi-analytical solution for the zero-dimensional stoichiometric case | 115 |
| B Calculation of the activity coefficient γ according to Bromley's Method..... | 118 |
| C List of publications of A.A. Öncül | 120 |
| D Curriculum vitae of A.A. Öncül..... | 123 |

Nomenclature

Latin symbols

| | | |
|-----------------|---|---|
| a | ionic activity | kmol/m ³ (= M) |
| A_γ | Debye-Hückel constant | kg ^{1/2} /mol ^{1/2} |
| b_i | nucleation rate exponent for preferential crystallization | – |
| $B_{+,-}$ | individual ion values | kg/mol |
| B_i | chemical species nucleation rate for preferential crystallization | 1/s |
| c_A | concentration of Ba ²⁺ ions for microemulsion precipitation | mol/L |
| c_B | concentration of SO ₄ ²⁻ ions for microemulsion precipitation | mol/L |
| c_{feed} | reactant concentration in the feed | mol/L |
| $c_{reactor}$ | reactant concentration inside the reactor | mol/L |
| cv | coefficient of variation | – |
| C_i | chemical species concentration | kmol/m ³ (= M) |
| $d_{4,3}$ | volume-averaged mean crystal size | µm |
| d_{imp} | impeller diameter | cm |
| d_D | droplet diameter | nm |
| \bar{d}_p | mean particle diameter | nm |
| d, D | inner and outer diameter of coaxial pipe mixer, respectively | m |
| f | normalized droplet number distribution | – |
| f_{ref} | reference droplet number distribution | – |
| $f(L)$ | normalized number density function | 1/m |
| F | functions in the activity coefficient equation | – |
| g | growth rate exponent | – |
| G_i | crystal growth rate | m/s |
| H_{center} | liquid surface height along central line in cellbags | m |
| H_l | local liquid surface height in cellbags | mm |
| I | ionic strength | mol/kg |
| J | nucleation rate for bulk precipitation | 1/(m ³ s) |
| k | turbulent kinetic energy | m ² /s ² |
| k_{at} | specific attachment rate of cells | 1/h |
| k_B | Boltzmann constant | J/K |
| $k_{b,i}$ | chemical species nucleation rate constant for preferential crystallization | 1/(m ³ s) for L-threonine 1/s for D-threonine |
| k_d | specific death rate of cells | 1/h |
| k_{det} | specific detachment rate of cells | 1/h |
| k_g | growth rate constant | m/s |
| k_{gro}^{eff} | effective growth rate constant | nm/s |

| | | |
|-----------------|---|---|
| k_{lys} | specific lysis rate of cells | 1/h |
| k_{nuc}^{eff} | effective nucleation rate constant | 1/(m ³ s) |
| k_v | volume shape factor | – |
| k_L | solubility product for microemulsion precipitation | mol ² /L ² |
| K_{sp} | thermodynamic solubility product | kmol ² /m ⁶ |
| l | coaxial pipe length | m |
| L | crystal size for bulk precipitation and preferential crystallization | μm |
| | characteristic liquid level in the cellbag | m |
| $L_{1,0}$ | number-averaged mean crystal size | μm for bulk precipitation m for preferential crystallization |
| $L_{4,3}$ | volume-averaged mean crystal size | μm |
| m_j | j th moment | m ^{j} /m ³ |
| $m(L)$ | mass density function | kg/m |
| M_i | chemical species mass | kg |
| M_M | molecule allocation matrix for nucleation | – |
| M_P | molecular mass of the solid particle | g/mol |
| $n(L)$ | number density function | 1/m |
| N_0 | total number of empty droplets | – |
| N_{crit} | critical number of molecules needed to form a stable nucleus | – |
| N_{feed} | total number of droplets fed per second | 1/s |
| $N_{l,max}$ | maximum number of dissolved reactant molecules per droplet | – |
| N_{rps} | impeller stirring rate | 1/s |
| N_s | total number of BaSO ₄ molecules in solid state | – |
| N_A | number of dissolved Ba ²⁺ ions in one droplet | – |
| N_A^{total} | total number of dissolved Ba ²⁺ ions in the system | – |
| $N_{Avogadro}$ | Avogadro's number | 1/mol |
| N_B | number of dissolved SO ₄ ²⁻ ions in one droplet | – |
| N_B^{total} | total number of dissolved SO ₄ ²⁻ ions in the system | – |
| N_M | total number of droplets in the reactor | – |
| $N_{M,0}$ | initial total number of droplets in the reactor | – |
| N_P | number of BaSO ₄ molecules per solid particle | – |
| \bar{N}_P | mean number of BaSO ₄ molecules per solid particle | – |
| P_{2D} | two-dimensional probability density function distribution | – |
| P_{2D}^{eq} | two-dimensional equilibrium distribution of the reactants | – |
| P_A | one-dimensional Poisson distribution for dissolved Ba ²⁺ ions | – |
| P_B | one-dimensional Poisson distribution for dissolved SO ₄ ²⁻ ions | – |
| Q | volumetric flow rate | m ³ /s |
| Q_c | circulation capacity | m ³ /s |
| r | radial coordinate | m |
| r_{gro} | growth rate for microemulsion precipitation | nm/s |

| | | |
|------------------|---|---|
| r_{nuc} | nucleation rate for microemulsion precipitation | $1/(m^3 s)$ |
| R | outer radius of the coaxial pipe mixer | m |
| SC_i | chemical species saturation constants for preferential crystallization | – |
| S | supersaturation ratio for bulk and microemulsion precipitation | – |
| S_g | specific crystal growth rate | kmol/(m ³ s) for bulk precipitation kg/s for preferential crystallization |
| S_i | chemical species supersaturation ratio for preferential crystallization | – |
| SC_i | chemical species source term for bulk precipitation | kg kmol/(m ⁶ s) |
| SM_i | chemical species source term for preferential crystallization | kg ² /(m ³ s) |
| t | time | s |
| t_{feed} | feeding time | s |
| T | temperature | K |
| u | velocity | m/s |
| u_{mean} | mean liquid velocity | m/s |
| u_x | component of the liquid velocity along the direction of rotation | m/s |
| V_{feed} | volume of the feed | mL |
| \dot{V}_{feed} | feed rate | mL/min |
| $V_{reactor}$ | volume of the reactor | mL |
| V_D | volume of one droplet | m ³ |
| V_W | volume of the water phase in the reactor | m ³ |
| W_i | chemical species molecular weight | kg/kmol |
| X_d | concentration of dead cells in suspension | cells/mL |
| X_{sus} | concentration of viable cells in suspension | cells/mL |
| X_{MC} | concentration of cells on microcarriers | cells/mL |
| Y_i | chemical species mass fraction | – |
| Z | charge number | – |

Greek symbols

| | | |
|----------------|--|----------|
| α_{gro} | growth rate law exponent | – |
| α_{nuc} | nucleation rate law exponent | – |
| β | non-dimensional parameter concerning turbulence onset estimation | – |
| γ | activity coefficient | – |
| Γ_{eff} | effective diffusivity | kg/(m s) |
| δ | Dirac-delta function | – |
| $\delta_{+,-}$ | individual ion values | – |
| Δc | concentration difference | mol/L |
| Δx | maximum fluid element displacement in the cellbag during one | m |

| | | |
|----------------------|---|--|
| | cycle | |
| ε | turbulent energy dissipation rate | m^2/s^3 |
| λ_A | mean droplet occupancy with Ba^{2+} ions | – |
| $\lambda_{A,0,feed}$ | initial mean droplet occupancy in the feed with Ba^{2+} ions | – |
| λ_B | mean droplet occupancy with SO_4^{2-} ions | – |
| $\lambda_{B,0}$ | initial mean droplet occupancy the reactor with SO_4^{2-} ions | – |
| μ | viscosity of water | $\text{kg}/(\text{m s})$ |
| μ_{eff} | effective viscosity | $\text{kg}/(\text{m s})$ |
| μ_j | j th moment for preferential crystallization | m^j |
| μ_{max} | maximum specific growth rate of cells | 1/h |
| ν | kinematic viscosity | m^2/s |
| ρ | density of water | kg/m^3 |
| ρ_i | chemical species density | kg/m^3 |
| σ | standard deviation | μm for bulk precipitation m for preferential crystallization |
| σ_{eff} | effective interfacial surface tension | J/m^2 |
| τ | time constant | s |
| τ_l | liquid shear stress | Pa |
| ϕ | sphericity | – |
| Ψ_T | growth rate coordinate transformation correlation | 1/nm |
| ω | angular velocity of oscillating flow | radian/s |

Dimensionless numbers

| | | |
|---------------|--------------------------|---|
| Re | Reynolds number | – |
| Sc_t | turbulent Schmidt number | – |
| Wo | Womersley number | – |

Abbreviations

| | | |
|-------|-------------------------------------|---|
| cGMP | Current Good Manufacturing Practice | – |
| CFD | Computational Fluid Dynamics | – |
| CPU | Central Processing Unit | – |
| CSBR | Continuously Stirred Batch Reactor | – |
| CSD | Crystal Size Distribution | – |
| CTA | Constant Temperature Anemometry | – |
| DQMOM | Direct Quadrature Method of Moments | – |
| LDPE | Low-Density Poly-Ethylene | – |
| MC | Microcarrier | – |
| MDCK | Madin-Darby Canine Kidney | – |
| MOM | Method of Moments | – |
| MRF | Multiple Reference Frames | – |

| | | |
|------|------------------------------|---|
| PBE | Population Balance Equation | — |
| PBM | Population Balance Model | — |
| PC | Personal Computer | — |
| PDF | Probability Density Function | — |
| PET | Poly-Ethylene Terephthalate | — |
| PSD | Particle Size Distribution | — |
| QMOM | Quadrature Method of Moments | — |
| SMM | Sliding Mesh Model | — |
| SMOM | Standard Method of Moments | — |
| STR | Stirred Tank Bioreactor | — |
| UDF | User-Defined Functions | — |
| UDS | User-Defined Scalars | — |
| VOF | Volume of Fluid | — |

Chapter 1

Introduction

Computational Fluid Dynamics (CFD) simulation of inhomogeneous flows employing population balance models (PBMs) has become an interesting subject in the research fields of chemical and biochemical engineering during the last decade. CFD tools have demonstrated their ability to deliver an initial physical guess for the planned applications or scale-up studies and to answer open questions. In this respect, CFD computations have widely been employed as a complementary method to experimental measurements especially for a refined analysis. Therefore, developments in CFD techniques are continuously being made for more accurate numerical predictions in acceptable computational times.

In the present work, CFD was coupled with appropriate PBMs and the resulting numerical tool was employed for the investigation of inhomogeneous flows in the following chemical and biochemical engineering applications (see Fig. 1.1 for the schematic representation of the organization of this work):

- bulk precipitation,
- microemulsion precipitation,
- preferential crystallization,
- animal cell cultivation.

The CFD/PBM tool was further combined with various numerical methods and models, depending on the application as explained below, for realistic computations. Before performing inhomogeneous simulations, a zero-dimensional (spatially homogeneous) analysis was performed in each application so that the obtained numerical results could initially be validated either via a semi-analytical solution or through the available experimental data.

In Chapter 2, numerical investigations on bulk precipitation of barium sulphate (BaSO_4) in a coaxial pipe mixer are presented. The corresponding experiences on:

- (i) the implementation of PBM into a CFD code via supplementary user-defined scalars (UDS) and user-defined functions (UDF),
 - (ii) the reconstruction of the crystal size distribution (CSD) of the resulting population
- are described in the corresponding chapter.

Chapter 3 deals with a similar investigation on the preferential crystallization of threonine enantiomers in a continuously stirred batch reactor (CSBR). The outstanding experiences gained during this study can be summarized as follows:

- (i) application of a moving mesh technique (i.e., sliding mesh model, SMM) for the representation of the impeller motion,
- (ii) application of two-population balance model, each population representing one threonine enantiomer,
- (iii) application of frozen flow conditions to reduce the high computational effort.

The associated numerical experiences showed that reasonable model reductions had to be performed in order to decrease the computational effort, especially in inhomogeneous cases.

In Chapter 4, studies concerning the derivation and the implementation of a reduced PBM in CFD simulations are explained for the microemulsion precipitation of BaSO_4 in a semi-batch reactor. Such model reductions allow numerical studies on process control, optimization and scale-up to become possible in acceptable computational times.

All these numerical experiences from various chemical engineering applications were then targeted to the major issue of this work (see Fig. 1.1): the characterization of the flow conditions in bioreactors (here, Wave Bioreactors[®], see Fig. 1.2) and simulation of the cultivation of animal (Madin-Darby Canine Kidney, MDCK) cells.

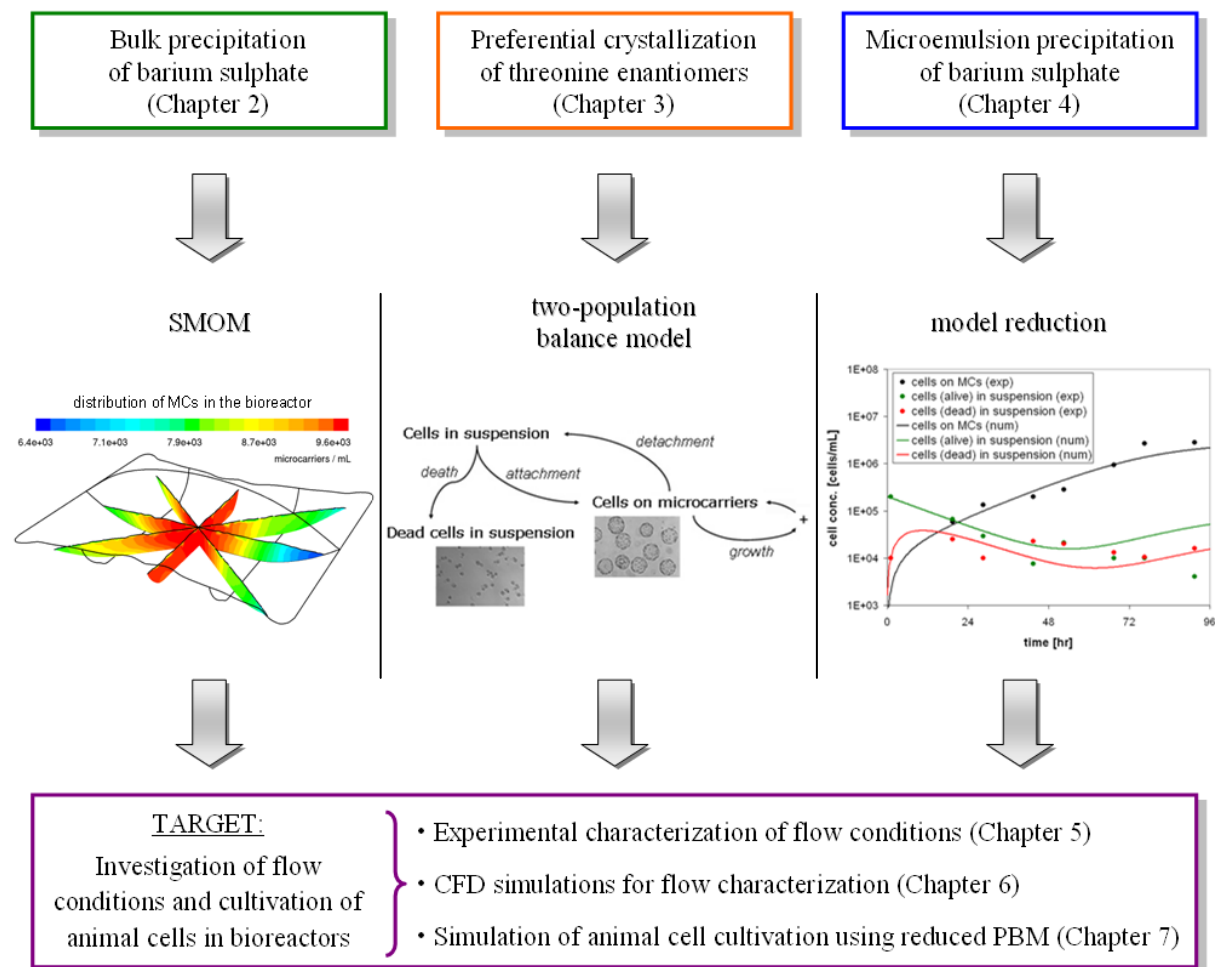


Fig. 1.1. Schematic representation of the organization of the present work.



Fig. 1.2. Wave Bioreactor[®].

Before performing numerical computations, experiments were carried out in order to characterize the flow conditions within the Wave Bioreactors[®] by measuring the most important flow parameters (i.e., liquid surface level, liquid velocity, liquid and wall shear stress). Chapter 5 conveys the obtained experimental results from these experimental studies. In this manner, the validity of the CFD

simulations describing the flow conditions could be checked by comparison with experimental data (Chapter 6). The CFD computations employed the Volume of Fluid (VOF) method for a correct prediction of the free liquid surface in the Wave Bioreactors[®]. The computational demand was considerably increased due to the application of the VOF method. Therefore, the simulations for the cultivation of animal cells were finally carried out for a zero-dimensional, homogeneous case but considering the obtained information on the flow conditions (especially the maximum shear stress values).

In Chapter 7, corresponding simulations for animal cell cultivation in a microcarrier (MC) system are described. These simulations employed an appropriate reduced PBM. In this respect, previous experiences (investigations on the microemulsion precipitation, Chapter 4) were essential (Fig. 1.1). The reduced PBM was based on the two-population balance approach with mutual interaction (Fig. 1.1): animal cells in suspension and animal cells on MCs. Therefore, we referred to the numerical experiences gained during the studies on the preferential crystallization (Chapter 3). The first population had an additional internal property; viable or dead cells. The second population was defined only with its own concentration without considering the size distribution as well as the spatial distribution of MCs. This simplification was decided by considering several assumptions. The MCs were first assumed to be monodisperse in size. As another assumption, the MCs were supposed to be homogeneously distributed in the liquid. In order to check the validity of the latter assumption, a realistic three-dimensional CFD simulation was first performed to analyze the spatial distribution of the MCs, initially located at the reactor bottom. For this purpose, SMOM was employed to describe the MC population (Fig. 1.1). For this particular point, the previous experience from the investigation on bulk precipitation (Chapter 2) was highly useful.

Concluding remarks and perspectives are given in Chapter 8.

Part I: Development of methods

Chapter 2

Method of moments (MOM): Bulk precipitation of barium sulphate

2.1 Introduction

The aim of this first study was to implement an appropriate PBM into CFD. Therefore, the precipitation model was coupled with the standard method of moments (SMOM) to describe the BaSO₄ crystal population, taking the first four moments into account. In this manner, experiences on PBM applications in CFD computations were gathered and were reemployed in further studies.

The initial part of the work considers the bulk precipitation (i.e., reactive crystallization) of BaSO₄ via the reaction of barium (Ba²⁺) and sulphate (SO₄²⁻) ions in turbulent flows using numerical simulations, since many questions are still open for this important process and for the associated numerical methods. The corresponding calculations were performed both for steady-state and for time-dependent conditions, for homogeneous as well as for mixing-controlled flows and for various reactant concentrations. Moreover, we investigated in this work the influence of the value and computational method for the activity coefficient on the crystallization process of BaSO₄. We considered for this a mixing-controlled configuration based on a coaxial pipe mixer. The corresponding flow is turbulent and this problem was solved using numerical simulations until reaching steady-state conditions.

All supplementary physical model equations and source terms were defined as user-defined scalars (UDS) and functions (UDF) in the Eulerian framework and compiled into a commercial CFD code (here FLUENT[®] 6.1). Assuming a prescribed function shape, for example a Gaussian, this further allowed us to depict the crystal size distribution (CSD) as a function of time or of the spatial position in the crystallization reactor.

Time-dependent simulations in a zero-dimensional (i.e., homogeneous) flow were first validated by comparison with the exact semi-analytical solution of the corresponding full reaction kinetic model. After this successful validation, steady-state calculations were performed for the coaxial pipe mixer using two different reference problems available in the literature. The quality of the employed numerical model was first checked by comparing with experimental results from Marchisio et al. (2002). Further simulations were then carried out for a second mixing problem (configuration of Wei and Garside, 1997), for which numerical results are available. For this second case, since the numerical methods and physical models used in the present work were noticeably improved compared to the original publication (finer grid, higher level of convergence, more accurate computation of the activity coefficient...), considerable differences in the findings were observed. Nevertheless, the coupling of the CFD code with SMOM using UDS and UDF, followed by an extensive post-processing of the results led to a detailed prediction of the obtained CSD for crystallization processes in non-homogeneous turbulent flows.

Further simulations were performed for various inlet concentrations with different values and models for computing the activity coefficient in order to analyze its influence on the product quantity and on the crystal size distribution at the pipe outlet. The supersaturation ratio, containing the activity coefficient in its definition, is the driving force for the crystallization process. This is the reason why, as concluded from the present results, it is important to model correctly and accurately the activity coefficient in order to obtain reliable data, a point which has been often neglected in the literature. Even relatively small variations of this coefficient can considerably affect the results, in particular for fast reactions.

Two related publications are presented in this chapter: “Numerical and analytical investigation of barium sulphate crystallization” and “Numerical investigation of the influence of the activity coefficient on barium sulphate crystallization” both published in the scientific journal *Chemical Engineering Science*. Since the theoretical background, the reaction kinetic equations and the employed numerical methods described in these two papers are identical, the papers are presented as a single combined paper by omitting identical explanations and sequencing the rest systematically, so that any unnecessary repetition is avoided.

Related publications

This chapter builds on top of:

Numerical and analytical investigation of barium sulphate crystallization

A.A. Öncül^{a,*}, K. Sundmacher^{b,c}, A. Seidel-Morgenstern^{b,d}, D. Thévenin^a

Chemical Engineering Science (2006) 61:652-664

combined with

Numerical investigation of the influence of the activity coefficient on barium sulphate crystallization

A.A. Öncül^{a,*}, K. Sundmacher^{b,c}, D. Thévenin^a

Chemical Engineering Science (2005) 60:5395-5405

^a*Institut für Strömungstechnik und Thermodynamik, Lehrstuhl für Strömungsmechanik und Strömungstechnik, Otto-von-Guericke-Universität-Magdeburg, 39106 Magdeburg, Germany*

^b*Max-Planck-Institut für Dynamik komplexer technischer Systeme, Sandtorstr. 1, 39106 Magdeburg, Germany*

^c*Institut für Verfahrenstechnik, Lehrstuhl für Systemverfahrenstechnik, Otto-von-Guericke-Universität-Magdeburg, 39106 Magdeburg, Germany*

^d*Institut für Verfahrenstechnik, Lehrstuhl für Chemische Verfahrenstechnik, Otto-von-Guericke-Universität-Magdeburg, 39106 Magdeburg, Germany*

2.2 State of the art

Crystallization and precipitation processes are widely used in the chemical industry. One of the most well-known crystallization processes is the reaction of barium (Ba^{2+}) and sulphate (SO_4^{2-}) ions into barium sulphate (BaSO_4), as shown in Eq. (2.1). This reaction has been widely investigated experimentally and a wealth of results can be found in the literature (e.g. Adityawarman et al., 2005; Bałdyga and Orciuch, 1997, 2001; Nielsen, 1964; Nielsen and Toft, 1984; Schwarzer and Peukert, 2004; Vicum et al., 2003):



In spite of all these experimental investigations, many questions are still open and there is a need for complementary information on this process, in particular in non-homogeneous situations. For this it would be very useful to describe numerically the kinetics of the crystallization together with the turbulent flow equations. This means that a coupling between computational fluid dynamics (CFD) techniques with a description of the chemical reactions and resulting particle population is extremely desirable (Fox, 1998; Schwarzer and Peukert, 2004). It is indeed a formidable task, and it must be admitted that the available numerical and physical models are still unsatisfactory to describe such complex flow systems. Nevertheless, such simulations are highly needed to improve the

* Corresponding author. Tel.: +49-391-6718195; fax: +49-391-6712840.
E-mail address: oncuel@ovgu.de (A.A. Öncül).

understanding, optimization and control of crystallization and precipitation processes. This is why numerous such investigations have been published recently. Gerstlauer et al. (2002), Jaworski and Nienow (2003), Logashenko et al. (2006) and Wei et al. (2001) have for instance modelled the mixing and the crystallization processes in continuously stirred batch reactors. Bałdyga and Orciuch (1997, 2001), Marchisio and Barresi (2003) and Wei and Garside (1997) introduced similar models for pipe mixers, as considered in this work. As a further step, Bałdyga and Bourne (1999), Marchisio and Barresi (2003) and Marchisio et al. (2002), Schwarzer and Peukert (2004) have examined the relevance of the micromixing model in such configurations, an important feature which is not considered in this work but is the subject of current investigations. Such numerical investigations are highly needed to improve the knowledge, optimization and control of crystallization processes as a complement or even as an alternative to costly experimental studies. But, since computing times can become very long, it is generally necessary to employ many assumptions and simplifications for the employed physical models. In this case the influence of such simplifications must be quantified. In the present chapter, we consider specifically the influence of the activity coefficient.

In this chapter two increasingly complex configurations are considered. First the focus is set on validation through an investigation of kinetic processes for crystallization in a homogeneous time-dependent reaction zone, meaning that this is in practice a zero-dimensional case in space. This configuration is in particular useful to identify the characteristic time-scales of this problem. Moreover, considering a stoichiometric mixture, it is simple enough to be solved semi-analytically. This is therefore used as an analytical validation of the numerical solution procedure developed in the present study.

In a second step steady-state operational coaxial pipe mixers involving a turbulent flow are investigated. For this purpose, two geometries previously described in the literature are employed. The first geometry corresponds to the work of Marchisio et al. (2002) and is used to validate for complex cases the results of the present numerical calculations by comparison with their experimental measurements. After this further validation step, a second mixer is considered, as used in the numerical work of Wei and Garside (1997). In this last case, both numerical (grid density, grid dependency, convergence criteria) and physical properties (computation of the activity coefficient) have been improved in the present work to obtain a better accuracy.

The kinetics of the crystallization process involve the nucleation rate and the growth rate of the crystals, which are directly dependent on the supersaturation ratio. The supersaturation ratio thus corresponds to the driving force of the process and includes an activity coefficient in its formulation. However, the effect of the value and of the definition of this activity coefficient is still an open question. For this reason, we find it useful to examine this point using the described numerical model and to analyze the resulting variations. We have for this purpose carried out a large number of simulations in a steady-state operational coaxial pipe mixer involving a turbulent flow. The geometry of this mixer is identical to that used in the work of Wei and Garside (1997) and Öncül et al. (2006).

All computations are carried out using the Computational Fluid Dynamics software FLUENT[®] 6.1, extended using supplementary User-Defined Scalars (UDS) and a compiled set of User-Defined Functions (UDF), taking into account all supplementary model equations and source terms.

For modelling the population balance of the solid particles, the standard method of moments (SMOM) is applied, using the first four moments only. This is now a well-known method and has been used several times to investigate crystallization processes (e.g. Bałdyga and Orciuch, 2001; Hulburt and Katz, 1964; Ramkrishna, 2000; Wang and Fox, 2003). Recently, this method has been extended and improved, leading to the quadrature method of moments (QMOM) and the direct quadrature method of moments (DQMOM), used for example in the numerical calculations of Fan et al. (2004), Marchisio et al. (2003) and Yoon and McGraw (2004). This is the subject of our present work concerning crystallization processes for which the agglomeration and breakage terms must be retained. Nevertheless computational times associated with QMOM/DQMOM are considerably higher than with SMOM, so that this simpler method is still interesting to obtain a first approximation of the solution in a relatively short time.

The size distribution of a crystalline product is an essential criterion for assessing the properties and quality of the product (Mersmann, 1995). It is therefore useful to present estimations of the crystal size distribution (CSD) for the different cases considered. This estimation is for example possible

using only the first three moments of the distribution and calculating the corresponding probability density function (PDF) of the BaSO₄ crystals, assuming a prescribed shape.

2.3 Reaction kinetics and model equations

The homogeneous precipitation model is based on several transport equations involving source terms for the chemical species and the moments of the distribution. As a final post-processing step, the crystal size distribution can be expressed in terms of these moments. To describe the fluid flow, the standard Reynolds-averaged Navier-Stokes equations are applied. The transport equations of the different chemical species, described in terms of their molar concentration C_i ($i = \text{Ba}^{2+}_{(\text{aq})}$, $\text{SO}_4^{2-}_{(\text{aq})}$, $\text{Na}^+_{(\text{aq})}$, $\text{Cl}^-_{(\text{aq})}$, $\text{BaSO}_{4(\text{s})}$) are given as

$$\frac{\partial(\rho C_i)}{\partial t} + \nabla \cdot (\rho u C_i - \Gamma_{\text{eff}} \nabla C_i) = S_{C_i}. \quad (2.2)$$

The effective turbulent diffusivity, Γ_{eff} , is computed by dividing the effective viscosity, μ_{eff} , with the turbulent Schmidt number, Sc_t , which is assumed here to be equal to 0.7. The source term S_{C_i} , divided by the density of the transporting fluid (in this case water), is taken equal to the specific crystal growth rate, S_g (Eq. 2.3), with a negative sign for Ba^{2+} and SO_4^{2-} (species consumption) and a positive sign for BaSO_4 (species generation). For the non-reacting species Na^+ and Cl^- this source term is set to zero. The specific crystal growth rate is related to the second moment of the crystal size distribution, m_2 (Jaworski and Nienow, 2003) by

$$S_g = \pm \frac{S_{C_i}}{\rho} = (3m_2 G) k_v \frac{\rho_{\text{BaSO}_4}}{W_{\text{BaSO}_4}}, \quad (2.3)$$

where the volumetric crystal shape factor, k_v , is $\pi/6$ for short residence times (Jaworski and Nienow, 2003), such as found in the present study. The density of BaSO₄ crystals, ρ_{BaSO_4} , is 4480 kg/m³ and their molecular weight, W_{BaSO_4} , is 233.39 kg/kmol.

The moments m_j of the CSD are computed according to the following moment transport equation, taking only the first four moments into account:

$$\frac{\partial(\rho m_j)}{\partial t} + \nabla \cdot (\rho u m_j - \Gamma_{\text{eff}} \nabla m_j) = \rho 0^j J + \rho j G m_{j-1} \quad (j = 0-3). \quad (2.4)$$

The crystal growth rate, G , and the nucleation rate, J , are calculated as functions of the supersaturation ratio S (Jaworski and Nienow, 2003):

$$G = k_g (S - 1)^2, \quad (2.5)$$

$$J = B \exp\left[-\frac{A}{\ln^2 S}\right], \quad (2.6)$$

where $B = 1 \times 10^{36}$ number of crystals/(m³ s) and $A = 2686$ for $S \geq 1000$, $B = 1.46 \times 10^{12}$ number of crystals/(m³ s) and $A = 67.3$ for $1 < S < 1000$. This nucleation kinetics has been first proposed by Nielsen (1964) and shows good agreement with the experimental measurements of Nielsen and Toft (1984). Here, it is worth noting that the crystal growth rate has been taken as a function of the local concentrations, as in many previous works, e.g. Bałdyga and Orciuch (1997); Falk and Schaer (2001); Jaworski and Nienow (2003); Wei and Garside (1997); Wei et al. (2001). Dirksen and Ring (1991) and Garside (1984) have further interpreted the crystal growth rate not only as a function of the

concentrations but also as a function of the crystal size, L , a point which is not considered here. Menon et al. (2005) have furthermore combined the crystal-size dependent growth rate approach with a two-population balance model in order to improve the description of the dynamic behavior of industrial crystallizers and validated their numerical results by comparison with experiments. The crystal growth rate constant, k_g , is equal in this work to 4×10^{-11} m/s for barium sulphate crystallization (Jaworski and Nienow, 2003).

The supersaturation ratio can be defined as (Jaworski and Nienow, 2003):

$$S = \gamma \left(\frac{C_{Ba} C_{SO_4}}{K_{sp}} \right)^{0.5}, \quad (2.7)$$

where γ is the activity coefficient and K_{sp} is the solubility product of $BaSO_4$ that is equal to 1.1×10^{-10} kmol^2/m^6 at 25°C . The activity coefficient is a factor that relates the activity of an ion in a solution, a , to its concentration:

$$a = \gamma C. \quad (2.8)$$

The activity coefficient decreases progressively as the ionic concentration increases (i.e. as the ionic interactions increase). Therefore, both the rate and the extent of a chemical reaction are determined by the ionic activity rather than by the concentration. This explains why the activity coefficient plays an important role in the modelling of such crystallization processes involving ionic species.

In the present study we will consider different models to compute the activity coefficient. The simplest one (model M1) considers that the activity coefficient is constant and takes its maximum possible value, $\gamma = 1$. To improve this first estimation, we then consider (model M2) a constant value of the activity coefficient, $\gamma = \text{constant}$, but compute the real value of γ corresponding to the initial conditions, using Bromley's method (Bromley, 1973). In an effort to get even better results, we finally consider the results obtained when computing at every point in the numerical domain and depending on the instantaneous concentrations the actual value of the activity coefficient (model M3), once again using Bromley's method, since this method supplies accurate data up to 6 M ionic strengths (Vicum et al., 2003). All the concentrations considered in this work lie within this range (max. 6 M ionic strength in the mixture for 2 M inlet concentrations). As a possible alternative, the modified Debye-Hückel method (Davies, 1962) is accurate only for mixtures with up to 0.6 M ionic strengths. For this reason this method is not applicable here, though it would be much simpler to solve the Debye-Hückel equation modified by Davies than to use Bromley's method.

To analyze the results we will consider the chemical conversion towards the product, since this is a very important aspect for practical applications. The chemical conversion is calculated as (Jaworski and Nienow, 2003):

$$Conv_{BaSO_4} = \frac{C_{BaSO_4, end}}{f C_{i, initial} - \sqrt{K_{sp}}} \quad \text{for } i = Ba^{2+}, SO_4^{2-}. \quad (2.9)$$

For the homogenous (zero-dimensional) simulations $f = 1$. The chemical conversion of $BaSO_4$ in the coaxial mixer pipe is expressed by the same equation, but with $f = 0.5$, to take into account the fact that there are two separate inlet streams.

In addition to all these equations, two supplementary quantities characterizing the CSD are also computed during the simulations. These are the number-averaged crystal size

$$L_{1,0} = \frac{m_1}{m_0} \quad (2.10)$$

and the coefficient of variation which is used to represent the width of the crystal size distribution:

$$cv = \left(\frac{m_0 m_2}{m_1^2} - 1 \right)^{1/2}. \quad (2.11)$$

The CSD is first assumed in this work to be of Gaussian shape, to simplify the computation but also considering available experimental results, which often show a nearly Gaussian shape. The shape of the CSD is assumed in the further work (i.e., study on the influence of the activity coefficient) to be a standard β -function (Heinz, 2003), since this function was found to be more appropriate than a Gaussian shape in a previous work (Öncül et al., 2006). This function has been already employed for chemical engineering applications for example by Bałdyga (1994), Frankel et al. (1991) and Li and Toor (1986).

The standard deviation, σ , (or the square root of the population variance, σ^2) used in the calculation of the Gauss-and β -functions is simply defined as the product of the number-averaged crystal size with the coefficient of variation (Chen et al., 1996):

$$\sigma = cvL_{1,0}. \quad (2.12)$$

More accurate and flexible possibilities to reconstruct the distribution from its known moments are considered in detail in John et al. (2007), but are not the subject of the present work.

2.4 Numerical and analytical investigations

The model equations explained above have been defined in terms of supplementary UDS and are solved using an external in-house UDF file. This UDF is compiled together with and integrated within the CFD package FLUENT[®] 6.1.

As explained previously, two configurations are considered: first a fully homogeneous case, mainly for extensive validation purposes, and then coaxial pipe mixers. In the first case (zero-dimensional analysis) no turbulence model is needed since the process is homogeneous, without any gradient in space. This first system is therefore quite simple, allowing even in some cases a semi-analytical solution, as shown later. The only evolution of the system takes place as a function of time. Iterations at each time-step continue until all residual values fall below 0.001.

For the coaxial pipe mixers, the flow is always steady-state but fully turbulent: $Re = 10\,000$ (resp. $12\,700$) for Marchisio et al. (2002) (resp. Wei and Garside, 1997). The standard k - ε approach is retained to compute turbulence effects, since this model should supply a reasonable accuracy and short computing times for this simple flow configuration. Moreover, this is the model employed in the previous works of Marchisio et al. (2002) and Wei and Garside (1997). In these steady-state computations, under-relaxation factors are used for continuity, momentum, turbulence and further transport equations. Aggregation and sedimentation of the solid phase and the effect of the gravity on this phase are neglected. In addition to this, a uniform inlet velocity is retained. The influence of micromixing is not considered in this work, but is the subject of our present activity (Öncül et al., 2009). All these simplifying hypotheses have been retained in these first comparisons since they have already been used by Wei and Garside (1997).

Table 2.1 represents the values of the fixed physical parameters used in all simulations. These values have been obtained from Jaworski and Nienow (2003), Wei and Garside (1997) and Wei et al. (2001).

Table 2.1. Physical parameters used in the simulations

| Parameter | Value | Unit |
|-----------------|-----------------------|-----------------------------------|
| ρ | 1000 | kg/m ³ |
| ρ_{BaSO_4} | 4480 | kg/m ³ |
| μ | 0.001 | kg/(m s) |
| K_{sp} | 1.1×10^{-10} | kmol ² /m ⁶ |
| k_g | 4×10^{-11} | m/s |
| k_v | $\pi/6$ | - |
| W_{BaSO_4} | 233.39 | kg/kmol |

2.4.1 Homogeneous (zero-dimensional) analysis

With FLUENT[®] it is not possible to perform directly a zero-dimensional computation. In order to carry out this computation, one therefore considers a fully homogeneous two-dimensional reaction zone for the 0-D analysis of the crystallization process. The Ba²⁺ and SO₄²⁻ ions are present in this zone initially at given amounts without any prior reaction.

For this 0-D analysis, both semi-analytical and numerical calculations have been performed in order to validate the population model implemented into FLUENT[®] through UDS/UDF. The semi-analytical solution, which relies on a direct solution of the moment equations in the stoichiometric case, is presented in Appendix A. For this zero-dimensional analysis two different cases have been simulated, first assuming a constant activity coefficient equal to 1. The corresponding initial values for these two cases are given in Table 2.2.

Table 2.2. Initial values for zero-dimensional analysis ($t = 0$)

| Case | C_{Ba} (M) | C_{SO_4} (M) | S ($\gamma = 1$) |
|------|--------------|----------------|----------------------|
| 1 | 0.04 | 0.04 | 3814 |
| 2 | 1 | 0.25 | 47673 |

The concentration profiles for the reactants and the product obtained from the numerical calculations using FLUENT[®] coupled with UDS/UDF are plotted as a function of the physical time in Fig. 2.1. The corresponding chemical conversion data and the used time-steps are listed in Table 2.3.

Table 2.3. Chemical conversion times and characteristic time-steps for 2 different initial concentrations ($\gamma = 1$)

| Case | Time at 50% conv. | Time at 90% conv. | Time at 99% conv. | Time-step | Unit |
|------|-------------------|-------------------|-------------------|-----------|---------|
| 1 | 2.14 | 6.95 | 55.2 | 0.01 | ms |
| 2 | 1.103 | 1.806 | 2.693 | 0.001 | μ s |

These concentration profiles represent qualitatively quite coherent results, which could be also expected from the chemical kinetics point of view. In the stoichiometric mixtures, the Ba²⁺ and SO₄²⁻ concentrations diminish in an identical manner. When Ba²⁺ is initially in excess, the reaction stops as soon as all initially available SO₄²⁻ has been consumed. From Tables 2.2 and 2.3, it can be seen that the used time-steps are roughly indirectly proportional to the values of the supersaturation ratio. In other words, when the initial concentrations increase, i.e. when the supersaturation ratio increases, the reaction rate increases and it is necessary to decrease the time-step in order to obtain accurate results.

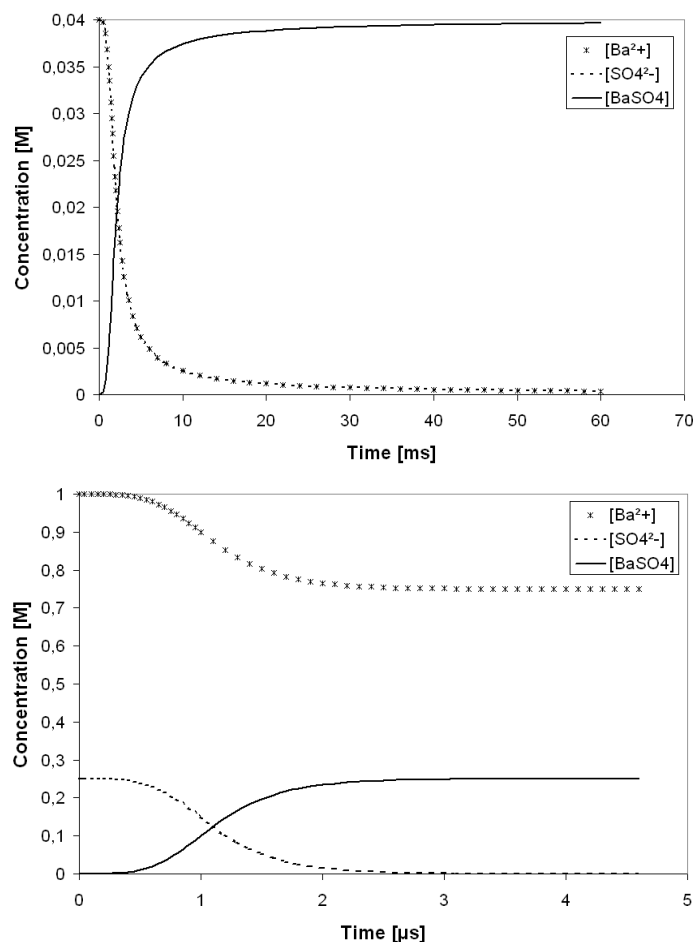


Fig. 2.1. Species concentrations versus time ($\gamma = 1$) for Case 1 (top) and Case 2, Ba^{2+} -rich (bottom).

For the stoichiometric configuration (Case 1), a semi-analytical solution of the full precipitation process can be obtained by solving directly the single ordinary differential equation (A.16) (see Appendix A). This semi-analytical solution can take into account any constant value of the activity coefficient. The corresponding semi-analytical result is exactly identical with the full numerical solution obtained using the coupled FLUENT[®]/UDS/UDF tool, as can be seen in Fig. 2.2.

For this comparison the activity coefficient, γ , has been taken constant and equal to its initial value ($\gamma = 0.23$) instead of taking it equal to 1 as in Table 2.2 and Fig. 2.1. As a consequence, the time needed to reach 90% chemical conversion becomes much longer, as can be observed by comparing the values in Table 2.3 and Fig. 2.1 (top) with Fig. 2.2. For this comparison, please take into account the fact that the x-axis of Fig. 2.2 is graduated in seconds while this of Fig. 2.1 (top) is expressed in milliseconds. This overwhelming effect of the activity coefficient for the crystallization of barium sulphate has been considered in great detail in a companion paper (Öncül et al., 2005). Considering the results of this chapter, it is reasonable for the present parameter values to assume a constant activity coefficient, equal to its initial value, rather than calculating it as a function of the local and instantaneous reactant concentrations. All further details concerning the practical computation of the activity coefficient following Bromley's method (Bromley, 1973) and the employed parameters can be found in Öncül et al. (2005). This computation relies on the parameters listed in Table 2.4. For an initial mixture with 0.04 M reactant concentrations (Case 1), these parameters lead to an initial activity coefficient $\gamma = 0.23$.

The perfect agreement between the semi-analytical and the numerical solutions observed in Fig. 2.2 proves that the extension developed on top of the available CFD software provides reliable data for the modelling of the $BaSO_4$ precipitation. This validates the full numerical procedure in the homogeneous case.

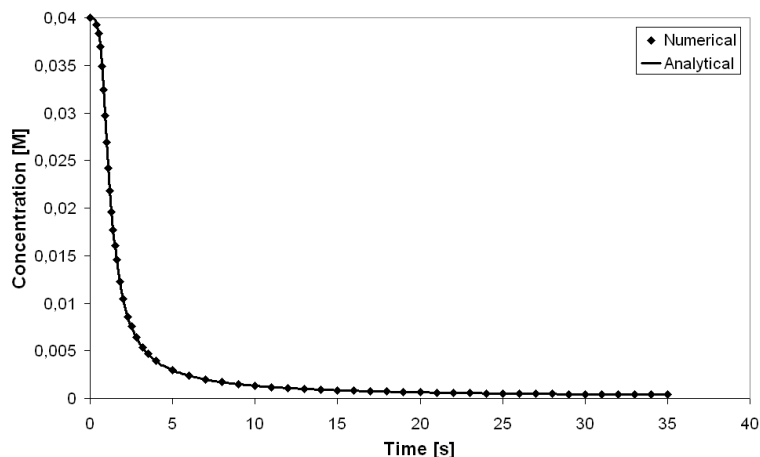


Fig. 2.2. Comparison of the numerical and semi-analytical results for a homogeneous stoichiometric reaction using a constant activity coefficient ($\gamma = 0.23$).

Table 2.4. Individual ion values in an aqueous solution at 25 °C (Bromley, 1973)

| Cation | B_+ (kg/mol) | δ_+ | Anion | B_- (kg/mol) | δ_- |
|------------------|----------------|------------|--------------------|----------------|------------|
| Na^+ | 0.0000 | 0.028 | Cl^- | 0.0643 | -0.067 |
| Ba^{2+} | 0.0022 | 0.098 | SO_4^{2-} | 0.0000 | -0.400 |

Additional simulations have been also performed using different initial stoichiometric concentrations, in order to obtain the physical time needed to reach 90% chemical conversion as a function of these initial conditions. In order to obtain accurate results for all the conditions considered, it is now necessary to compute the activity coefficient as a function of the time-dependent reactant concentrations (see again Öncül et al., 2005 for further explanations). Fig. 2.3 presents the corresponding results and shows clearly how fast the reaction typically proceeds (for instance only 1 ms is needed to reach 90% chemical conversion at 5 M). It also demonstrates the considerable influence of the initial concentrations on the time needed for chemical conversion, since this conversion is greatly accelerated for higher initial concentrations (note the logarithmic time-scale on the y-axis of Fig. 2.3).

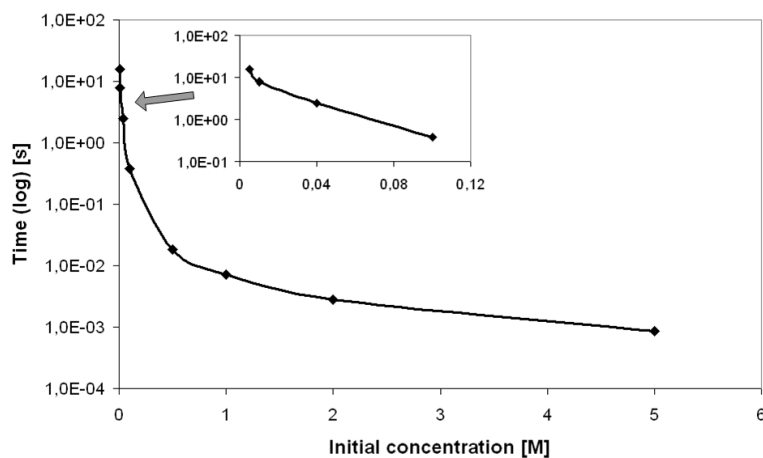


Fig. 2.3. Time needed to reach 90% chemical conversion using the exact value of the activity coefficient γ during the computation. Inlaid is a zoom on the region with low initial concentrations.

The values of all parameters (total number of crystals, mean crystal size and coefficient of variation) obtained from the CFD and needed to describe the CSD compare well with results from the literature, obtained for the same process but in other configurations (e.g. Wei and Garside, 1997; Wei et al., 2001).

Using these parameters it is possible to try to reconstruct the underlying CSD. This is indeed a difficult task and many different possibilities can be tested for this purpose (John et al., 2007). Using here a very simple assumption (the distribution shows a Gaussian shape), the obtained crystal size distributions for the two previously defined cases are displayed for different chemical conversion values (and thus indirectly as a function of time) in Fig. 2.4. As it can be seen from Fig. 2.4a, as the reaction proceeds, i.e., as the conversion increases, the mean size of the crystals increases whereas the variance and the number of crystals per length unit remain roughly constant. This result is expected for the standard growth model of the crystals with time, leading to crystals with larger mean sizes during the process.

The fact that the reconstructed CSD sometimes predicts a non-zero quantity of crystals with zero length (Fig. 2.4a) is related to the assumption of a Gaussian shape. Assuming another shape, for instance a standard β -function (Heinz, 2003), this problem can be solved, as seen in Fig. 2.4a. The β -function is widely used in the combustion and flow turbulence community but has also been already employed for chemical engineering applications for example in Bałdyga (1994), Frankel et al. (1991) and Li and Toor (1986). Considering the observed improvement, and in the light of many further tests (John et al., 2007), it is usually better to rely on such β -functions to describe CSD using an assumed distribution shape.

It is also worth noting that for higher initial concentrations, i.e., for faster reactions, the CSD is narrower and spikier with a lower mean size (Fig. 2.4b). This kind of particle distribution is usually more interesting in practical applications.

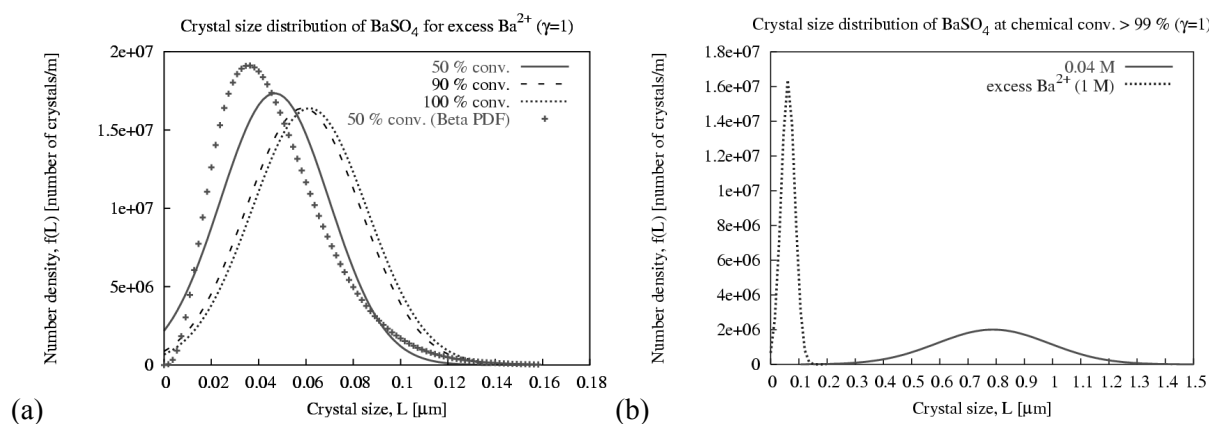


Fig. 2.4. (a) Reconstructed distribution for Case 2, including a comparison of the CSD obtained assuming a Gaussian resp. a β -function shape; (b) Comparison of the CSD obtained for Cases 1 and 2.

2.4.2 Coaxial pipe mixers

After this first, semi-analytical validation step, two different coaxial pipe mixers involving a turbulent flow are now considered. The geometries with all dimensions and flow parameters of these mixers are given in Fig. 2.5 and Table 2.5. Since a rotational symmetry exists, the coaxial mixers are simulated in two dimensions using an axi-symmetric formulation. This reduces the needed computational time and memory. Similar structured grids with 26405 (resp. 22650) cells have been used for Geometry 1 (Marchisio et al., 2002) and Geometry 2 (Wei and Garside, 1997), respectively. A part of this grid near the inlet of the Geometry 2 is shown in Fig. 2.6. We have checked carefully the grid independency of the presented results, obtained for a second-order discretization and high convergence requirements. For the Geometry 1, Na₂SO₄ is fed through the inner pipe while BaCl₂ is

fed in the surrounding annular pipe and vice versa for the Geometry 2. The factor α given in Table 2.5 for Geometry 1 controls the inlet concentration of BaCl_2 by taking the values 0.1, 1.0, 1.5 and 3.0 (Marchisio et al., 2002).

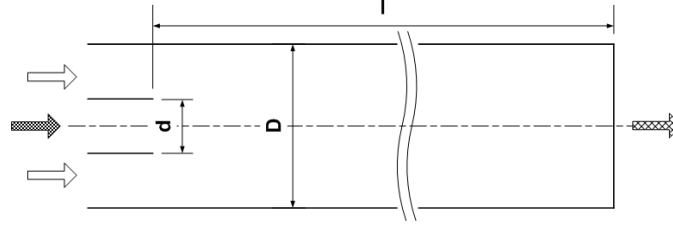


Fig. 2.5. Geometry of the coaxial pipe mixers.

Table 2.5. Dimensions and flow parameters of the two coaxial pipe mixers

| Dimension | Geometry 1 | Geometry 2 | Unit |
|---|---|--------------------|-----------------------|
| D | 0.01 | 0.1 | m |
| d | 0.001 | 0.0333 | m |
| l | 2 | 2 | m |
| Re | 10 000 | 12 700 | - |
| $Q_{\text{Na}_2\text{SO}_4,\text{inlet}}$ | 7.85×10^{-7} | 5×10^{-4} | m^3/s |
| $Q_{\text{BaCl}_2,\text{inlet}}$ | 7.85×10^{-5} | 5×10^{-4} | m^3/s |
| $C_{\text{Na}_2\text{SO}_4,\text{inlet}}$ | 0.0341 | 0.08 | M |
| $C_{\text{BaCl}_2,\text{inlet}}$ | $\alpha \times C_{\text{Na}_2\text{SO}_4,\text{inlet}}$ | 0.08 | M |

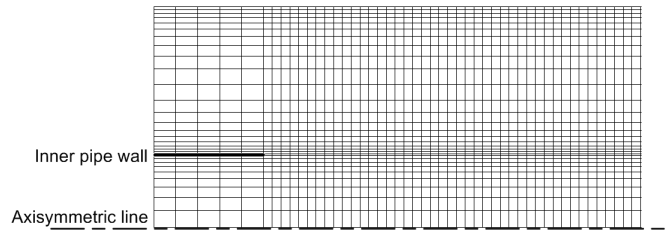


Fig. 2.6. Structured grid employed for Geometry 2, near the inlet.

A time-scale analysis can be carried out in order to assess the effect of micromixing on the reaction. For this, the characteristic reaction time (τ_R) and the molecular diffusion time constant (τ_G) are compared. The diffusion time is estimated by (Vicium et al., 2004):

$$\tau_G = 17.24 \left(\frac{\nu}{\varepsilon} \right)^{0.5} \left(0.03 + \frac{17050}{\text{Sc}_t} \right)^{-1}, \quad (2.13)$$

where ν is the kinematic viscosity and ε is the energy dissipation rate. The values for this time constant in Geometry 1 and 2 are found to be 6.0×10^{-6} and 7.0×10^{-4} s, respectively. The characteristic reaction time at 90% chemical conversion for the same initial mixture concentration but for a homogeneous reaction is about 47 s for Geometry 1 with $\alpha = 0.1$ (resp. 2.5 s for Geometry 2 as can be seen in Fig. 2.3). Since in both cases $\tau_R \gg \tau_G$ the influence of molecular diffusion can be considered negligible in both geometries.

As previously explained the first geometry is that used by Marchisio et al. (2002) and has been employed here in order to validate the numerical model for a complex problem by comparison with

their experimental data. Since Marchisio et al. (2002) have reported the mean crystal sizes in terms of the third and fourth moments ($d_{4,3}$), the fourth moment has been defined as an additional transport equation in the UDF file for this case.

During the simulations, the under-relaxation factors associated with the transport equations describing the moments are adjusted in a stepwise increasing manner, due to the extremely stiff numerical character of the rapid crystal growth. The iteration process is therefore started with very small values of the under-relaxation factors, down to a value of 1×10^{-6} and after sufficient (at least a factor of 10) reduction of the normalized residuals these values are increased by a factor of 10, repeating this procedure up to reaching a maximum under-relaxation factor of 0.9. When starting the computation with higher values for the under-relaxation factors, divergence is observed within the first iterations. A similar method has also been applied by Jaworski and Nienow (2004) to solve a similar numerical issue. Both simulations have been pursued until all concentration changes remain at the level of machine precision. On a single Pentium-IV Linux PC (2.7 GHz) the corresponding computation takes between 2 and 20 h until convergence depending on the initial supersaturation ratio.

Considering the findings of Öncül et al. (2005), the activity coefficient, γ , has been calculated exactly for both coaxial pipe mixers, as a function of the local, instantaneous reactant concentrations. As the reaction proceeds the ionic strength of the mixture changes since BaSO_4 crystals precipitate as a non-ionic compound. Hence, the activity coefficient changes as well since it is a function of the ionic strength. In other words, as the reaction takes place the ionic strength of the solution decreases, due to decreasing ionic concentrations, and accordingly the activity coefficient increases. Theoretically, for extremely dilute solutions, the activity coefficient approaches its maximum value, 1.0. To carry out the practical computation, the activity coefficient has been defined as a supplementary variable and is computed inside the in-house UDF file as a function of the time-dependent and spatially inhomogeneous ion concentrations along the pipe (Öncül et al., 2005).

The results obtained by the developed numerical procedure are compared with the experimental and numerical data of Marchisio et al. (2002) in Fig. 2.7. As it can be seen, the numerical results (square symbols in Fig. 2.7) obtained in the present work for the mean crystal size $d_{4,3}$ compare quite well with the experimental measurements of Marchisio et al. (2002). Taking into account the experimental uncertainty (error bars), the agreement is at least as good as that achieved by the original authors themselves (see diamonds in Fig. 2.7). The sphericity, ϕ_c , used in this work to convert the computed characteristic mean crystal size, $L_{4,3}$, to $d_{4,3}$ following Eq. (2.14) is equal to 1, since the volume shape factor, k_v , is assumed here to be equal to $\pi/6$ (spheres):

$$d_{4,3} = \phi_c L_{4,3}. \quad (2.14)$$

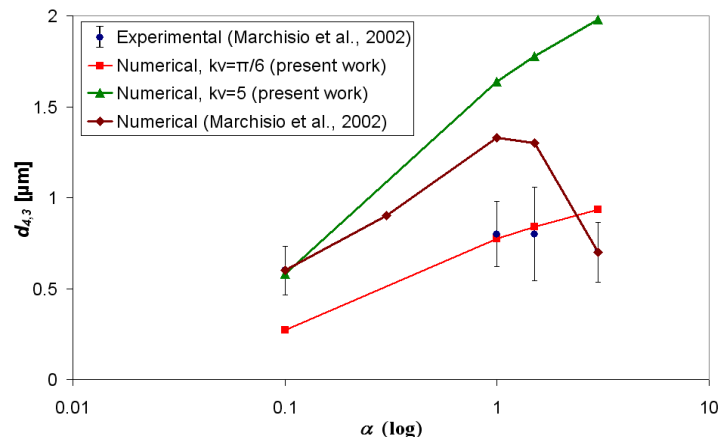


Fig. 2.7. Comparison of the numerical results obtained in this work (square and triangular symbols, depending on sphericity) with the experimental (filled circles with error bars) and numerical (diamonds) data reported by Marchisio et al. (2002).

On the other hand, Marchisio et al. (2002) have assumed the volume shape factor to be equal to 5 for their corresponding calculations (diamonds in Fig. 2.7). That is why further calculations have also been performed taking this value into consideration for comparison (triangles symbols in Fig. 2.7). In that case, a good agreement is only found for the lowest values of α . An important difference between the present numerical model and that of Marchisio et al. (2002) is that the micromixing effects are neglected in the present formulation. This might explain why some discrepancies are observed between the present numerical results and those of Marchisio et al. (2002) for higher values of α . Since the issue of micromixing is the subject of our present activity, this might be cleared up in the future (Öncül et al., 2009). Nevertheless, the numerical data obtained in this work already show an acceptable agreement with the experimental measurements, even without considering micromixing effects.

Wei and Garside (1997) have performed numerical simulations of a similar coaxial pipe mixer using Geometry 2 and parameters listed in Table 2.5. They employ a constant value for γ , not listed explicitly in the paper. Considering the results they show and back-computing the activity coefficient leads to a guessed value of $\gamma=0.63$, but with a considerable uncertainty. Computing directly the value of γ using Bromley's method with the known inflow conditions leads to $\gamma=0.23$. Since Wei and Garside (1997) mention explicitly that they also use Bromley's method, $\gamma=0.23$ is adopted in the present work to start the simulations. The further evolution of γ is directly given by the exact computation depending on the local, instantaneous concentrations (Öncül et al., 2005). In order to try to explain the discrepancies described later on, another computation using a constant activity coefficient, $\gamma=0.63$, has also been performed.

The velocity field in the inlet region is shown in Fig. 2.8, and contour plots along the full numerical domain are presented in Fig. 2.9. The corresponding mass-averaged resulting values obtained along the outlet at convergence for both $\gamma=0.23$ (initial value, spatially-varying) and $\gamma=0.63$ (constant) are listed in Table 2.6.

Table 2.6. Mass-averaged results at the outlet of the coaxial mixer

| Parameter | $\gamma=0.63$ (constant) | $\gamma_{\text{initial}}=0.23$ (variable) | Unit |
|------------------------------|--------------------------|---|---------------|
| S | 378.5 | 885.9 | - |
| C_{Ba} | 0.0063 | ~ 0.04 | M |
| C_{SO_4} | 0.0063 | ~ 0.04 | M |
| C_{BaSO_4} | 0.0337 | 1.22×10^{-6} | M |
| Chem. conversion | 84.25% | 0.003% | - |
| Mean crystal size, $L_{1,0}$ | 0.236 | 0.1356 | μm |
| Coeff. of variation, cv | 0.1555 | 0.5898 | - |

Fig. 2.8 shows that the velocity vectors in the inlet region all point in the axial direction. No recirculation occurs at the mixing point between the two inlet streams since the separating wall has no thickness, as in the reference geometry. It is therefore unclear why such a recirculation was obtained in Wei and Garside (1997), since it is quite surprising for this simple flow configuration. According to Table 2.6 the chemical conversion at the outlet of the pipe is 84.25% for $\gamma=0.63$ (constant), a value of γ probably similar to that used in Wei and Garside (1997). This would be quite a good value for a crystallization process, but Wei and Garside (1997) have themselves reported a chemical conversion of around 3% for the same geometry and parameters (at least to the best of our knowledge). They have further obtained a cv of 0.5 and a $L_{1,0}$ of 1.4 μm . The agreement with the present values, listed in Table 2.6, is thus poor.

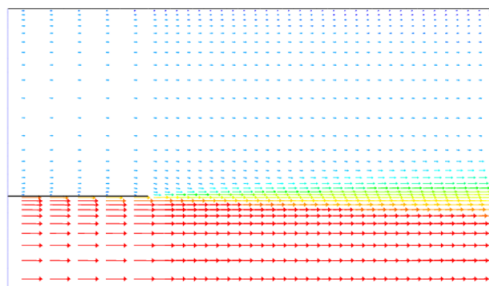


Fig. 2.8. Velocity field in the vicinity of the inlets (min: 0; max: 0.588 (m/s)).

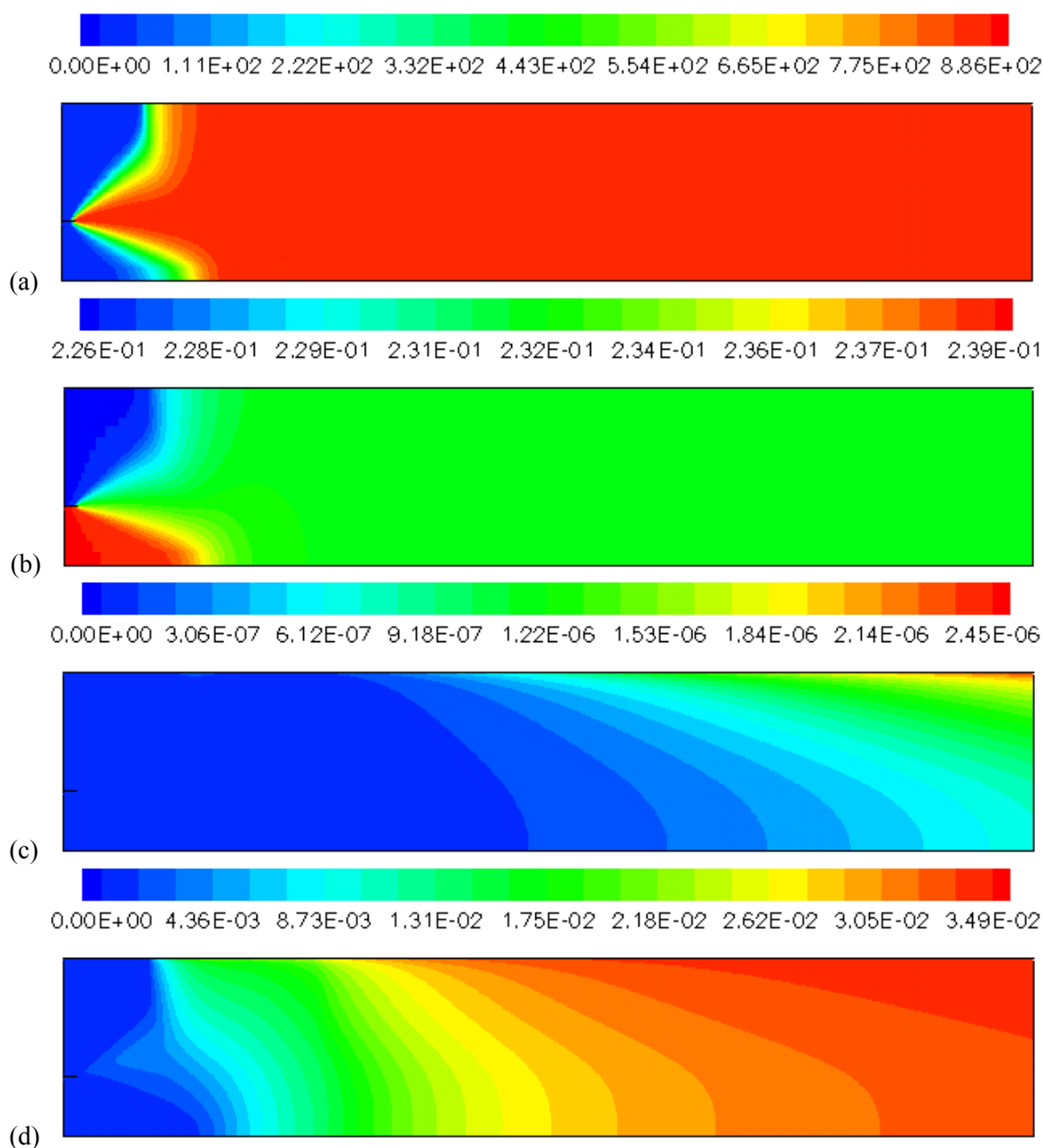


Fig. 2.9. Contour plots for the coaxial pipe mixer simulation, Geometry 2: (a) supersaturation ratio, (b) activity coefficient and (c) BaSO_4 concentration (M) for varying activity coefficient (initially $\gamma = 0.23$), and (d) BaSO_4 concentration (M) for constant activity coefficient ($\gamma = 0.63$) (the radial direction has been magnified by a factor of 8 in each picture to improve visualization).

Many reasons can be proposed to explain the observed discrepancies. First, Wei and Garside (1997) used a coarse grid (60 x 108 points), almost four times coarser than the present grid. They have already stopped the simulation as soon as the residuals have been reduced by a factor of 1000. The present computation is pursued until all concentration changes remain at the level of machine precision, which is by comparison associated with a considerably stronger residual reduction. In the present work, grid independency of the results has been investigated in detail by refining locally the grid with respect to the supersaturation ratio gradient in a repetitive manner. All observed relative differences stayed below 1%, showing that the initial numerical parameters and grid are sufficient for this case. It has also been checked that the obtained results are not modified noticeably by using 2nd-order discretization. Considering all these points together with the previous validation procedure, we feel confident that the results shown in the present work represent correctly the main processes controlling this configuration. The obtained discrepancies for Geometry 2 are therefore not interpreted as a failure of the developed numerical procedure, but as a consequence of improved numerical and physical parameters.

When using the exact initial value ($\gamma = 0.23$) and calculation methodology for the activity coefficient (Öncül et al., 2005), the chemical conversion obtained at the outlet becomes almost negligible (around 0.003%), as shown in Table 2.6. In spite of the long tube considered here (2 m), and since the reaction is quite slow in this case due to a low activity coefficient (see also Fig. 2.3, showing the fastest possible conversion times, obtained for a homogeneous case), it is only beginning at the end of the pipe. For such inlet concentrations, the computed activity coefficient almost does not change along the pipe (Fig. 2.9b) since the reaction proceeds extremely slowly. That is why the supersaturation ratio remains almost constant, too (Fig. 2.9a).

In addition to the contour plots of the simulation results, shown in Fig. 2.9, the crystal size distributions observed at the outlet of the pipe for the spatially-varying activity coefficient ($\gamma = 0.23$ initially) are also plotted as a function of the radial position in Fig. 2.10. As it can be seen, the CSD at the outlet is narrower near the pipe axis but much wider near the outer pipe wall ($r = 5$ cm). This result can be related to the contour plot of the BaSO₄ concentration given in Fig. 2.9c. Near the outlet, new crystals tend to form near the pipe axis and show naturally smaller mean lengths with a narrower size distribution, since crystal growth is only beginning. On the other hand, near the pipe wall, where the first crystals have already been produced earlier, the necessary time has been achieved for a first crystal growth. The mean size of the crystals in this case approaches the one obtained in the 0-D analysis with similar initial concentrations (see Fig. 2.4b).

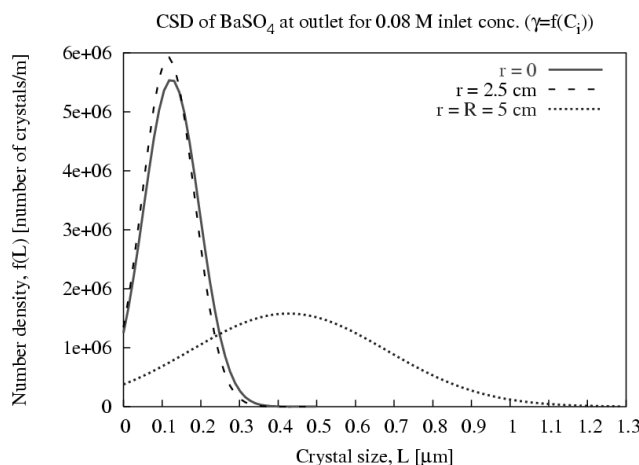


Fig. 2.10. Distribution of the BaSO₄ crystals at the pipe outlet as a function of the radial position for the exact computation of the activity coefficient.

2.5 Influence of the activity coefficient

2.5.1 Numerical investigations

The geometry and all dimensions of the coaxial pipe mixer in this part of the work are given in Fig. 2.5 and Table 2.5 (Geometry 2).

A total number of 12 simulations (see Table 2.7 for a summary) have been carried out in order to investigate the effect of the activity coefficient on the chemical conversion of the barium sulphate crystallization and on the CSD. These include four different stoichiometric inlet concentrations (0.08, 0.3, 0.7 and 2 M) each case being simulated either for $\gamma = 1$ (i.e., without really considering the activity coefficient, model M1), for $\gamma = \text{constant}$ corresponding to the initial concentrations (model M2) and for $\gamma = f(C_i)$ (i.e., as a function of the instantaneous local species concentrations, model M3).

The value of the activity coefficient, γ , is calculated according to Bromley's method (Bromley, 1973) for models M2 and M3. The step-by-step calculation of the activity coefficient of a BaCl_2 and Na_2SO_4 mixture is presented in Appendix B to illustrate the procedure. Here, only the corresponding initial activity coefficient values are given in Table 2.7 (in parenthesis, for model M2), for the four inlet concentrations described above.

Table 2.7. Conditions associated with the 12 simulations performed in this work (activity coefficients in parenthesis are the initial values for the corresponding inlet concentrations)

| Case number | Concentration | Model |
|-------------|---------------|---------------------------|
| #1 | } 0.08 M | M1 |
| #2 | | M2 ($\gamma = 0.23229$) |
| #3 | | M3 |
| #4 | } 0.3 M | M1 |
| #5 | | M2 ($\gamma = 0.12185$) |
| #6 | | M3 |
| #7 | } 0.7 M | M1 |
| #8 | | M2 ($\gamma = 0.07567$) |
| #9 | | M3 |
| #10 | } 2 M | M1 |
| #11 | | M2 ($\gamma = 0.03889$) |
| #12 | | M3 |

As it can be seen from the table above, as the inlet concentration increases the initial value of the activity coefficient decreases as explained in the previous sections. As the reaction proceeds the ionic strength of the mixture changes in reality since BaSO_4 crystals precipitate as a non-ionic compound along the coaxial pipe. Thus, the activity coefficient changes as well since it is a function of the ionic strength. In other words, as the reaction proceeds the ionic strength of the solution decreases, due to decreasing ionic concentrations, and accordingly the activity coefficient increases. Theoretically, for extremely dilute solutions, the activity coefficient approaches its maximum possible value, 1.0. The activity coefficient has been defined as a supplementary variable and is either taken as a constant (models M1 and M2) or computed inside the developed UDF file as a function of the time-dependent and spatially inhomogeneous ion concentrations along the pipe in order to carry out the practical computation for $\gamma = f(C_i)$ (model M3).

The under-relaxation factors associated with the transport equations describing the moments are adjusted in a stepwise increasing manner during the simulations, due to the extremely stiff numerical character of the rapid crystal growth. For this reason, the iteration process is started with very small

values of the under-relaxation factors, for instance down to a value of 1×10^{-6} for a molarity of 0.08 M and 1×10^{-10} for a molarity of 2 M, and after sufficient (at least a factor of 10) reduction of the normalized residuals these values are increased by a factor of 10, repeating this procedure up to reaching a maximum under-relaxation factor of 0.9. When starting the computation with higher values for the under-relaxation factors, divergence is observed within the first iterations. All simulations have been pursued until the changes of all concentrations have reached the level of machine precision. The corresponding computations take 20–40 h depending on the initial conditions when working with a single Pentium-IV Linux PC (2.7 GHz/2 GB memory).

2.5.2 Results and discussion

Complementary information concerning for example the flow velocity can be found in Öncül et al. (2006), but are not relevant for the present investigation.

As explained previously, simulations for different values and models of the activity coefficient have been performed (Table 2.5). The contour plots of the simulation results for 0.08 M inlet concentrations and $\gamma = f(C_i)$ (computation #3) are displayed in Fig. 2.9 as an example.

As it can be seen from Fig. 2.9c, the mass-averaged chemical conversion obtained at the outlet is almost negligible in this case (around 0.003%), in spite of the long tube considered here (2 m). This is due to the fact that the reaction is very slow under these conditions because of the relatively low chemical activity. However, since the fluid velocity is lower near the pipe wall (no-slip conditions), the crystals experience a longer time for crystal growth in this region, due to the higher residence time. In contrary to this, only young crystals exist near the pipe axis close to the outlet. For these inlet concentrations, the computed activity coefficient almost does not change along the pipe (it stays very close to the initial value $\gamma = 0.23229$) since the reaction proceeds extremely slowly (Fig. 2.9b). That is why the supersaturation ratio is almost constant as well (Fig. 2.9a). The incompleteness of mixing in this configuration has already been observed in Garside and Wei (1997).

If a longer pipe, higher inlet concentrations or lower inlet flow rates are used, the change of the activity coefficient along the pipe can be seen clearly. In order to observe this effect, we consider here more concentrated inlet streams while keeping the length of the pipe and the inlet velocity constant. In Fig. 2.11 the contour plot of the activity coefficient along the pipe is represented for the highest inlet concentration used in this work (2 M). In this case, the variation of the activity coefficient can be seen very clearly: γ is about 2.53 times larger at the end of the pipe compared to its initial value.

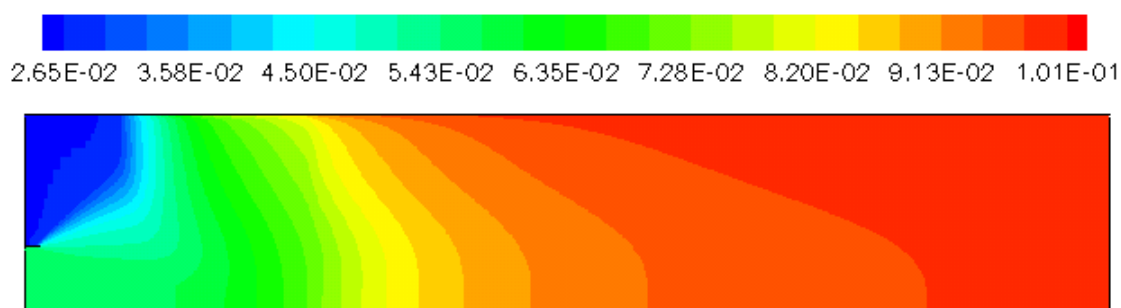


Fig. 2.11. Contour plot for activity coefficient results of the coaxial pipe mixer simulations with 2 M inlet concentrations and $\gamma = f(C_i)$ (computation #12). Compare to Fig. 2.9b for differences (the radial direction has been magnified by a factor of 8).

In Figs. 2.13 and 2.14 the simulation results for all 12 cases are represented along the coaxial pipe mixer as a function of the axial position (along the thick black line ending at point A depicted in Fig. 2.12), starting from the end of the separation wall between the two inlet streams, where the mixing and consequently the reaction starts.

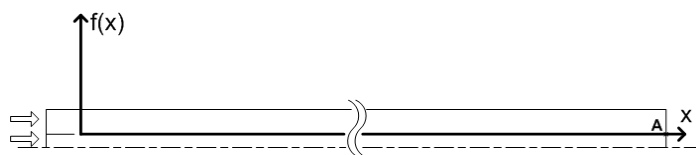


Fig. 2.12. Location of the simulation results shown in the next figures: solid black line leading to point A (for Figs. 2.13, 2.14 and 2.16). Point A (for Figs. 2.15 and 2.17).

When comparing models M1, M2 and M3, it can be observed that the supersaturation ratio (Fig. 2.13) starts from considerably higher values for $\gamma = 1$ and decreases drastically along the axial direction. Note that all plots in Figs. 2.13 and 2.14 use a logarithmic scale, so that these changes concern several orders of magnitude. For example, in Fig. 2.13c, the supersaturation ratio decreases by almost three orders of magnitude along the pipe for model M1. These extremely large changes predicted by model M1 are due to the fact that a considerable amount of crystals are produced from the start due to a higher initial supersaturation and thus a higher initial ionic activity. Even if $\gamma = 1$ is a hypothesis which is quite often found in the literature, it appears to be completely wrong for the present configuration. Considering for comparison the models M2 and M3, the supersaturation ratio starts at a lower and (of course, since it is the basic hypothesis underlying model M2) at the same values for $\gamma = \text{initial value}$ (model M2) and $\gamma = f(C_i)$ (model M3) and then decreases slowly along the pipe. For 0.08 M the supersaturation ratio almost does not change with models M2 and M3 since the chemical activity for this case is extremely low (see again Fig. 2.9a-c). The behavior obtained with models M2 and M3 is thus completely different from the results obtained with the simplest model, M1, which leads to an extremely poor approximation. On the other hand, models M2 and M3 behave in a similar manner. For low inlet concentrations, they are even almost identical. When increasing the molarity, noticeable differences appear (remember the log scale). For example, for Fig. 2.13c, a maximum relative difference of 50% is obtained at point A between models M2 and M3.

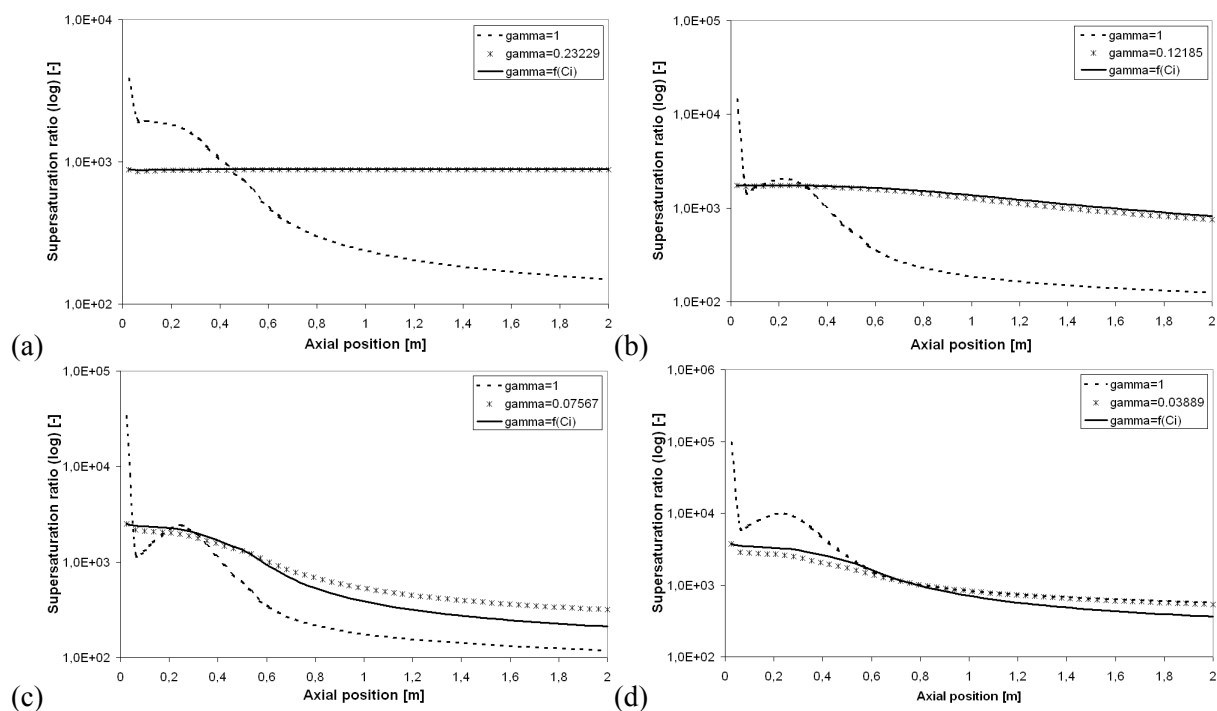


Fig. 2.13. Supersaturation ratio (note the log scale) along the axial direction for all 12 different cases: (a) 0.08 M, computations #1 to 3, (b) 0.3 M, computations #4 to 6, (c) 0.7 M, computations #7 to 9, and (d) 2 M inlet concentrations, computations #10 to 12.

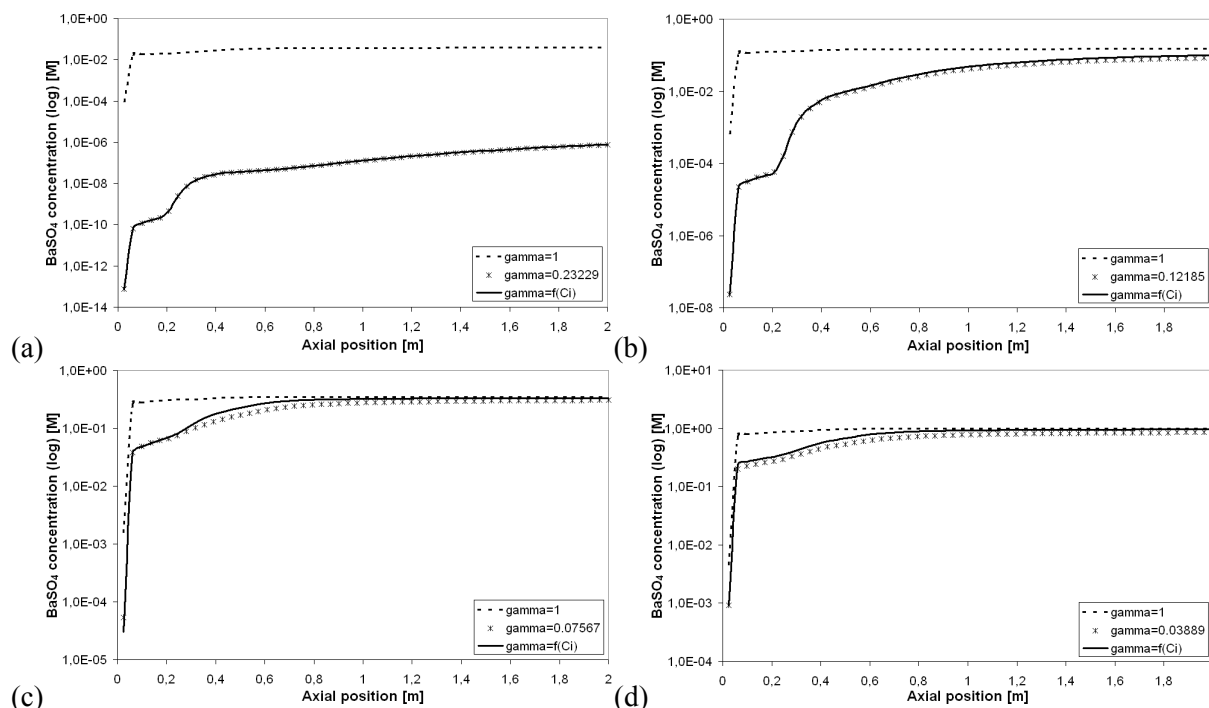


Fig. 2.14. BaSO₄ concentration (note the log scale) along the axial direction for all 12 different cases: (a) 0.08 M, computations #1 to 3, (b) 0.3 M, computations #4 to 6, (c) 0.7 M, computations #7 to 9, and (d) 2 M inlet concentrations, computations #10 to 12.

Fig. 2.14 shows clearly that a noticeable amount of barium sulphate is already produced near the inlet region for all cases considered here. The BaSO₄ concentration, thus the chemical conversion, increases along the pipe, and this increase is particularly fast along the first 20–30 cm. Once again, model M1 delivers completely wrong results compared to the better models, M2 and M3. On the other hand, due to the logarithmic scale in Fig. 2.14, one gets the feeling that models M2 and M3 deliver almost identical results.

In order to check this point in a more quantitative manner, we have computed the relative difference between the different models for the chemical conversion obtained at point A, for all 12 configurations. Corresponding results are presented in Fig. 2.15. As the inlet concentration increases, the relative difference between models M1 and M3 decreases (due to an increasing chemical activity) and the relative difference between models M2 and M3 increases (due to increasing chemical conversion obtained by model M3). Fig. 2.15 shows that the chemical conversion at the outlet is not much affected by the definition of the activity coefficient for high inlet concentrations, when such a long pipe is taken into consideration. The difference between models M1 and M3 at point A stays below 10% for an initial molarity higher than roughly 0.5 M. However, this conclusion would be of course very different if we would consider only the first part of the coaxial pipe mixer, for example 10 cm after mixing starts. This shows that the quality of a simplifying hypothesis will be problem-dependent, as expected.

When comparing models M2 and M3, we observe in Fig. 2.15 that the relative difference in the chemical conversion between $\gamma = \text{initial value}$ (model M2) and $\gamma = f(C_i)$ (model M3) is always lower than 15% at the pipe outlet. For this reason, the activity coefficient might be in general taken as constant and equal to its initial value (especially for very dilute mixtures) in order to shorten the computational times for such relatively long pipes. For very complex problems this might be an interesting alternative to the calculation of the actual value of γ at every iteration and at every grid point. Nevertheless, from a theoretical point of view, the most accurate results are obtained when the activity coefficient is computed correctly, i.e., when it is defined as a function of the local ionic concentrations, of course.

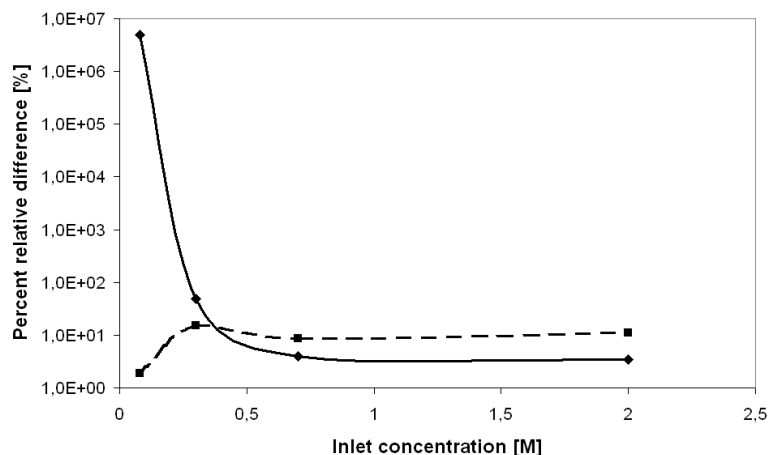


Fig. 2.15. Relative difference (log scale) in the obtained chemical conversion at Point A between $\gamma = 1$ (model M1) and $\gamma = f(C_i)$ (model M3): solid line; respectively between $\gamma = \text{initial value}$ (model M2) and $\gamma = f(C_i)$ (model M3): dashed line.

From a practical point of view, the computation of the actual value of γ is associated to an increase of computing time by roughly 28% compared to model M2. This increase is mainly due to the two additional UDS taken into account in the UDF for Na^+ and Cl^- . Considering this small supplementary requirement, it will probably be generally as easy to implement and use directly the best model, M3.

In Fig. 2.16, the change in the value of the activity coefficient along the pipe mixer (same line as in Figs. 2.13 and 2.14, shown as a solid black line in Fig. 2.12) is represented for all four inlet concentrations used in this work. Although γ is almost not changing for 0.08 M, the variation of the activity coefficient becomes quite important for higher inlet concentrations. It is interesting to note that a plateau is observed for all initial concentrations at least over the first 20 cm near the inlet, before the increase in γ really starts. It is also remarkable that the activity coefficient for initial molarities of 0.7 M locally exceeds that observed for 0.3 M, a fact which was not expected and demonstrates the high impact of the coupling between the different physical processes involved.

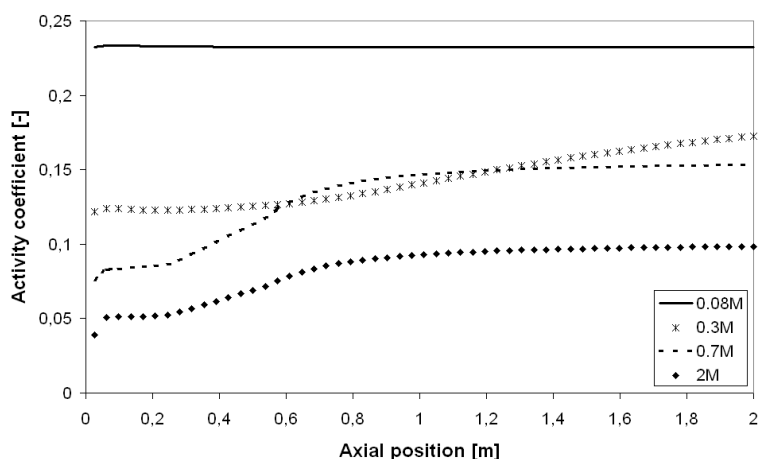


Fig. 2.16. Axial variation of the activity coefficient (model M3) for different inlet concentrations.

In addition to these results, the crystal size distributions observed at Point A are also plotted for the 12 different computations (Fig. 2.17). As it can be seen from this figure, the crystal size distribution is strongly affected by the definition of the activity coefficient as well. First of all, we note that the number-averaged crystal size, $L_{1,0}$ (not shown) is much higher for $\gamma = \text{initial value}$ (model M2) and $\gamma = f(C_i)$ (model M3) than for $\gamma = 1$ (model M1). For example in Fig. 2.17c, the crystal size

associated to the peak of the distribution is roughly 100 times larger for models M2/M3 compared to M1, demonstrating the remarkable influence of the model used for the activity coefficient on the CSD. This is due to the fact that the nucleation rate is much higher than the crystal growth rate for $\gamma = 1$ compared to the other two cases. Secondly, the total number of crystals is lower for $\gamma = \text{initial value}$ (model M2) and $\gamma = f(C_i)$ (model M3) in comparison to $\gamma = 1$ (model M1). This point can directly be related to the conversion of BaSO_4 . The higher the chemical conversion, the higher the number of crystals. It is also interesting to point out that the CSDs obtained for these two models ($\gamma = \text{initial value}$ and $\gamma = f(C_i)$) are almost identical when considering only Point A, at the outlet of the coaxial pipe mixer (Fig. 2.12), even if slight differences can be seen on Fig. 2.17c (and also on Fig. 2.17d although it is not clearly observed here due to the scaling). This conclusion is not necessarily true everywhere within the computational domain, of course.

Anyway, all these results show that the definition of the activity coefficient has indirectly a very large influence on the chemical conversion and crystal size distribution in the configuration considered here.

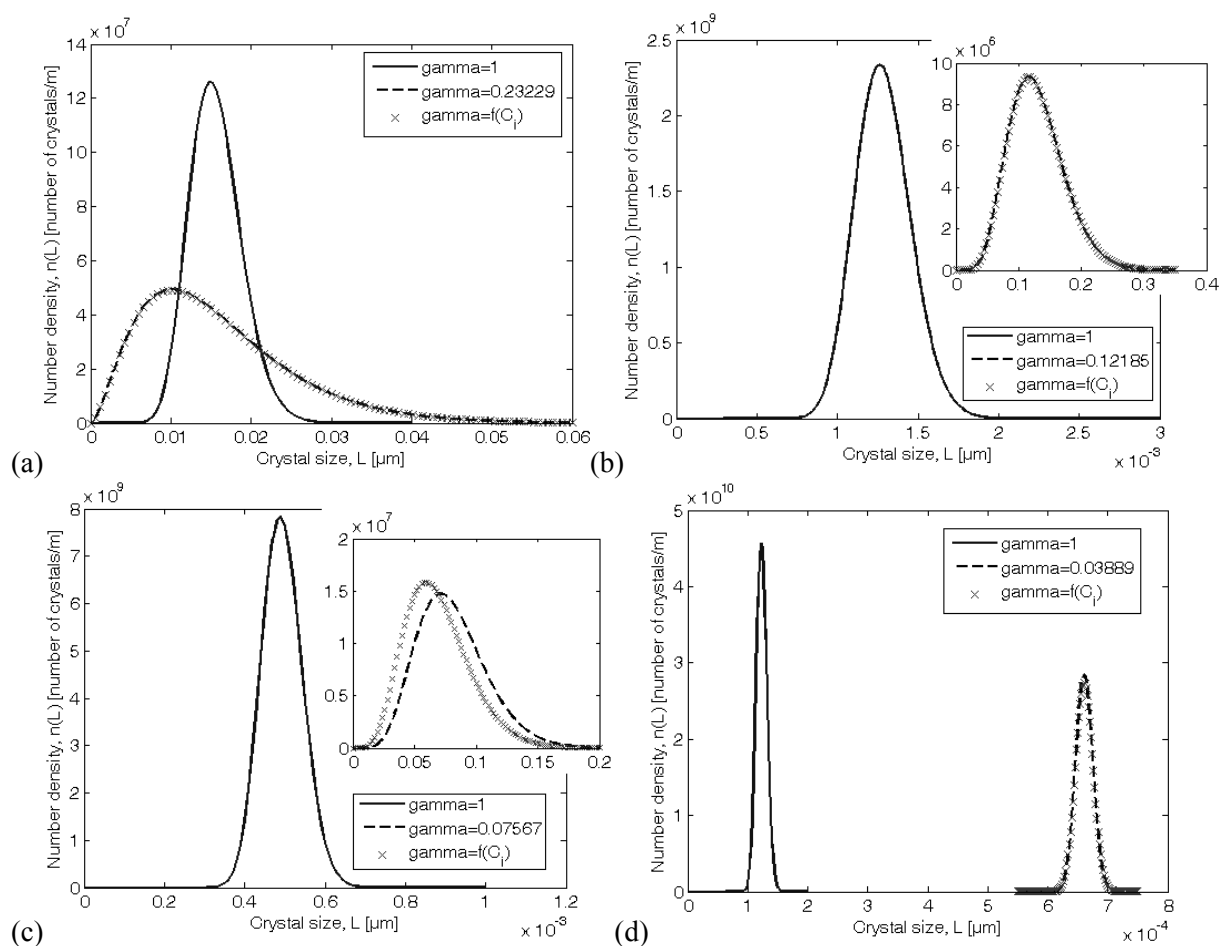


Fig. 2.17. CSD plots for BaSO_4 crystals at Point A: (a) 0.08 M, (b) 0.3 M, (c) 0.7 M and (d) 2 M inlet concentrations. In all cases, the CSD is supposed to have the shape of a β -function.

2.6 Conclusions and remarks

The aim of this chapter was to develop appropriate numerical methods coupled with SMOM for the corresponding PBM and perform a numerical investigation for homogeneous BaSO_4 crystallization. For this purpose an extensive validation procedure has been carried out. First a semi-

analytical solution obtained for a time-dependent zero-dimensional stoichiometric configuration has been considered, leading to a perfect agreement. Moreover, these first computations have shown that the reaction is generally quite fast and that the reaction time decreases rapidly for increasing initial concentrations.

In a second step two different geometrical configurations found in the literature and corresponding to coaxial pipe mixers involving a turbulent flow are simulated in steady-state. Comparisons with previously published experimental results are quite satisfactory for the first geometry, corresponding to the work of Marchisio et al. (2002). For the second comparison, based on the numerical results of Wei and Garside (1997), the results are quite disappointing, since considerable discrepancies are observed. Nevertheless, several reasons could justify the differences obtained in the present work: a better and finer grid, a higher numerical convergence and in particular the influence of the value of the activity coefficient.

Most of these simulations have been found to be very stiff. It was therefore necessary to use extremely small time-steps (time-dependent computations) resp. under-relaxation factors (steady-state cases), in particular for high concentrations. In order to obtain reliable data, it is useful to quantify convergence by considering the changes of all concentrations, which leads to a stronger constraint compared to the standard built-in residuals.

Considering the evolution of the CSD, it can be noticed that, for initial higher concentrations, i.e., higher supersaturation ratios, the mean particle size of the product diminishes rapidly in the zero-dimensional, fully homogeneous case. For the coaxial pipe mixer, broader crystal size distributions are obtained near the outer pipe wall.

The purpose of the final step was to analyze the effect of the value of the activity coefficient on barium sulphate crystallization. After having developed and validated a numerical procedure to compute BaSO_4 crystallization in the previous work, we have therefore carried out 12 computations, using three different modelling levels and four compositions.

Using these results, we show that the value and modelling level of the activity coefficient is very important for such crystallization processes. For high initial concentrations, the value of the activity coefficient, γ , completely determines the beginning of the process, just after mixing starts. For low initial concentrations, γ controls the chemical conversion at the end of the coaxial pipe mixer. Considering only the outlet values, the relative difference observed between $\gamma = 1$ and the most accurate model $\gamma = f(C_i)$ decreases for increasing initial concentrations. The results obtained with the intermediate modelling level $\gamma = \text{initial value}$ are in much better agreement with the results of the exact model, $\gamma = f(C_i)$. Depending on the requested accuracy, this intermediate model might be sufficient for most studies.

Similar conclusions have been obtained for the CSD at the output of the coaxial pipe mixer. For $\gamma = 1$, much lower number-averaged crystal sizes but a higher total number of crystals are obtained in comparison with the more accurate models, $\gamma = \text{initial value}$ and $\gamma = f(C_i)$. However, the differences in the CSD obtained for these two better models, $\gamma = \text{initial value}$ and $\gamma = f(C_i)$, are small, confirming the result stated above.

As a conclusion of the final step, the activity coefficient might be generally taken constant and equal to its initial value in order to reduce the computational times, leading to differences typically below 15% compared to the most accurate model, $\gamma = f(C_i)$. On the other hand, taking a constant activity coefficient with a value of 1 is a very bad approximation for the kind of problems considered in this work, apart for situations involving very high molarities.

Beyond applying the developed numerical tool to other geometries, the influence of further physical processes (micromixing, but also agglomeration and breakage, which are essential for many crystallization processes) is now taken into consideration.

As a whole, it can be concluded that the basis of the PBM applications in CFD computations via in-house built UDS and UDF was firmly established during this initial study. Hence, the gained numerical experiences will be very useful for further studies considering disperse particle populations in inhomogeneous flows.

References of Chapter 2

- Adityawarman, D., Voigt, A., Veit, P., Sundmacher, K. (2005). Precipitation of BaSO₄ nanoparticles in a non-ionic microemulsion: Identification of suitable control parameters. *Chem. Eng. Sci.*, 60, 3373-3381.
- Baldyga, J. (1994). A closure model for homogeneous chemical reactions. *Chem. Eng. Sci.*, 49, 1985-2003.
- Baldyga, J., Orciuch, W. (1997). Closure problem for precipitation. *Trans. Inst. Chem. Eng.*, 75A, 160-170.
- Baldyga, J., Bourne, J.R. (1999). Turbulent mixing and chemical reactions. New York: Wiley.
- Baldyga, J., Orciuch, W. (2001). Barium sulphate precipitation in a pipe – an experimental study and CFD modelling. *Chem. Eng. Sci.*, 56, 2435-2444.
- Bromley, L.A. (1973). Thermodynamic properties of strong electrolytes in aqueous solutions. *AIChE J.*, 19, 313-320.
- Chen, J.F., Zheng, C., Chen, G.T. (1996). Interaction of macro- and micromixing on particle size distribution in reactive precipitation. *Chem. Eng. Sci.*, 51, 1957-1966.
- Davies, C.W. (1962). *Ion Association*. Washington: Butterworths.
- Dirksen, J.A., Ring, T.A. (1991). Fundamentals of crystallization: kinetic effects on particle size distribution and morphology. *Chem. Eng. Sci.*, 46, 2389-2427.
- Falk, L., Schaer, E. (2001). A PDF modelling of precipitation reactors. *Chem. Eng. Sci.*, 56, 2445-2457.
- Fan, R., Marchisio, D.L., Fox, R.O. (2004). Application of the direct quadrature method of moments to polydisperse gas-solid fluidized beds. *Powder Technol.*, 139, 7-20.
- Fox, R.O. (1998). On the relationship between Lagrangian micromixing models and computational fluid dynamics. *Chem. Eng. Process.*, 37, 521-535.
- Frankel, S.H., Madnia, C.K., Givi, P. (1991). Modelling of the unmixedness in homogeneous reacting turbulence. *Chem. Eng. Commun.*, 104, 117-125.
- Garside, J. (1984). Advances in the characterisation of crystal growth. *AIChE Symp. Ser.*, 80, 23-38.
- Garside, J., Wei, H. (1997). Pumped, stirred and maybe precipitated: Simulation of precipitation processes using CFD. *Acta Polytech. Scand. Chem. Technol. Ser.*, 244, 9-15.
- Gerstlauer, A., Motz, S., Mitrovic, A., Gilles, E.-D. (2002). Development, analysis and validation of population models for continuous and batch crystallizers. *Chem. Eng. Sci.*, 57, 4311-4327.
- Heinz, S. (2003). *Statistical mechanics of turbulent flows*. Berlin: Springer Verlag.
- Hulburt, H.M., Katz, S. (1964). Some problems in particle technology, a statistical mechanical formulation. *Chem. Eng. Sci.*, 19, 555-574.
- Jaworski, Z., Nienow, A. (2003). CFD modelling of continuous precipitation of barium sulphate in a stirred tank. *Chem. Eng. J.*, 91, 167-174.
- Jaworski, Z., Nienow, A.W. (2004). A strategy for solving a mathematical model of barium sulphate precipitation in a continuous stirred tank reactor. *Chem. Eng. Res. Des.*, 82, 1089-1094.
- John, V., Angelov, I., Öncül, A.A., Thévenin, D. (2007). Techniques for the reconstruction of a distribution from its moments. *Chem. Eng. Sci.*, 62, 2890-2904.
- Li, K.T., Toor, H.L. (1986). Turbulent reactive mixing with a series-parallel reaction-effect of mixing on yield. *AIChE J.*, 32, 1312-1320.
- Logashenko, D., Fischer, T., Motz, S., Gilles, E.-D., Wittum, G. (2006). Simulation of crystal growth and attrition in a stirred tank. *Comput. Visualization Sci.*, 9, 175-183.
- Marchisio, D.L., Barresi, A.A. (2003). CFD simulation of mixing and reaction: the relevance of the micro-mixing model. *Chem. Eng. Sci.*, 58, 3579-3587.
- Marchisio, D.L., Barresi, A.A., Garbero, M. (2002). Nucleation, growth, and agglomeration in barium sulphate turbulent precipitation. *AIChE J.*, 48, 2039-2050.
- Marchisio, D.L., Vigil, R.D., Fox, R.O. (2003). Implementation of the quadrature method of moments in CFD codes for aggregation-breakage problems. *Chem. Eng. Sci.*, 58, 3337-3351.

- Menon, A.R., Kramer, H.J.M., Grievink, J., Jansens, P.J. (2005). Modelling the cyclic behaviour in a DTB crystallizer – a two-population balance model approach. *J. Cryst. Growth*, 275, 1373-1381.
- Mersmann, A. (1995). *Crystallization technology handbook*. New York: Marcel Dekker Inc.
- Nielsen, A.E. (1964). *Kinetics of precipitation*. Oxford: Pergamon Press.
- Nielsen, A.E., Toft, J.M. (1984). Electrolyte crystal growth kinetics. *J. Cryst. Growth*, 67, 278-288.
- Öncül, A.A., Janiga, G., Thévenin, D. (2009). Comparison of various micromixing approaches for computational fluid dynamics simulation of barium sulfate precipitation in tubular reactors. *Ind. Eng. Chem. Res.*, 48, 999-1007.
- Öncül, A.A., Sundmacher, K., Seidel-Morgenstern, A., Thévenin, D. (2006). Numerical and analytical investigation of barium sulphate crystallization. *Chem. Eng. Sci.*, 61, 652-664.
- Öncül, A.A., Sundmacher, K., Thévenin, D. (2005). Numerical investigation of the influence of the activity coefficient on barium sulphate crystallization. *Chem. Eng. Sci.*, 60, 5395-5405.
- Ramkrishna, D. (2000). *Population balances, theory and application to particulate systems in engineering*. New York: Academic Press.
- Schwarzer, H.-C. Peukert, W. (2004). Combined experimental/numerical study on the precipitation of nanoparticles, *AIChE J.*, 50, 3234-3247.
- Vicum, L., Mazzotti, M., Bałdyga, J. (2003). Applying a thermodynamic model to the non-stoichiometric precipitation of barium sulphate. *Chem. Eng. Technol.*, 26, 325-333.
- Vicum, L., Ottinger, S., Mazzotti, M., Makowski, L., Bałdyga, J. (2004). Multi-scale modeling of a reactive mixing process in a semibatch stirred tank. *Chem. Eng. Sci.*, 59, 1767-1781.
- Wang, L., Fox, R.O. (2003). Application of in situ adaptive tabulation to CFD simulation of nanoparticle formation by reactive precipitation. *Chem. Eng. Sci.*, 58, 4387-4401.
- Wei, H., Garside, J. (1997). Application of CFD modelling to precipitation systems. *Chem. Eng. Res. Des.*, 75, 219-227.
- Wei, H., Wei, Z., Garside, J. (2001). Computational fluid dynamics modelling of the precipitation process in a semibatch crystalliser. *Ind. Eng. Chem. Res.*, 40, 5255-5261.
- Yoon, C., McGraw, R. (2004). Representation of generally mixed multivariate aerosols by the quadrature method of moments: I. Statistical foundation. *J. Aerosol Sci.*, 35, 561-576.

Chapter 3

Interacting populations: Preferential crystallization of threonine enantiomers

3.1 Introduction

The central application considered in this work (cell cultivation in bioreactors) involves several populations (viable or dead cells, attached or in suspension, microcarriers) interacting with each other and with the local flow. As a first step towards this complex issue, only two populations with a simple interaction are first considered: enantiomer crystals.

The preferential crystallization of enantiomers of organic compounds becomes increasingly important, in particular for the pharmaceutical industry. Very often, only one of the enantiomers of a chiral component shows the desired properties for the end-user. For conglomerates an isolation of the target enantiomer is possible using the principle of preferential crystallization (or crystallization by entrainment). A mixture of two threonine ($C_4H_9NO_3$) enantiomers, L- and D-threonine, dissolved in water was chosen in this work as a model system. Based on mass balances a model was developed capable to describe the crystallization of L-threonine. With this model, we investigated numerically the concentration changes occurring in a batch crystallizer after addition of seeds of L-threonine into a metastable solution of racemic composition. The growth of the seeds and the homogeneous nucleation of new particles could also be investigated. The obtained results were compared with available experimental data.

The aim of this study was to obtain the threonine crystal populations with a two-population balance approach (each population representing an enantiomer). Therefore, we coupled the kinetic model with the two-population balance approach based on SMOM and then implemented within the CFD code (FLUENT[®] 6.1) in order to examine the size distribution of the grown and of the nucleated crystals at the end of the process for different hydrodynamic conditions in the crystallizer.

Related publication

This chapter builds on top of:

Numerical analysis of the preferential crystallization of enantiomers

A.A. Öncül^{a,*}, D. Thévenin^a, M.P. Elsner^b, A. Seidel-Morgenstern^{b,c}

11th Workshop on Two-phase Flow Predictions (2005), Merseburg-Halle,
ISBN:3-86010-767-4, pp. 5.10/1-5.10/15

^aInstitut für Strömungstechnik und Thermodynamik, Lehrstuhl für Strömungsmechanik und Strömungstechnik, Otto-von-Guericke-Universität-Magdeburg, 39106 Magdeburg, Germany

^bMax-Planck-Institut für Dynamik komplexer technischer Systeme, Sandtorstr. 1, 39106 Magdeburg, Germany

^cInstitut für Verfahrenstechnik, Lehrstuhl für Chemische Verfahrenstechnik, Otto-von-Guericke-Universität-Magdeburg, 39106 Magdeburg, Germany

3.2 State of the art

The enantioseparation has a great importance in the industry since most organic compounds exist as enantiomers (i.e. as chiral structures). In this work, the preferential crystallization of two threonine enantiomers, L- and D-threonine (Fig. 3.1), is numerically investigated.

Threonine ($C_4H_9NO_3$) is a colourless, in water soluble, crystalline (Fig. 3.2), hydroxylated amino acid which is essential for the metabolism. At the same time, it can not be produced by the metabolism itself. It is found at high concentrations in the heart, skeletal muscles and central nervous system and is needed to maintain the proper protein balance in the body. L-threonine is one of the two chiral compounds (enantiomers) of the threonine and is the naturally occurring form. Large quantities of it are found in most protein-containing food sources. Metabolism needs can thus be covered via nutrition. In the case of a deficiency of L-threonine, it can be supplied using medicals. That is why the production of threonine has a great importance in the pharmaceutical industry. Therefore, the preferential crystallization of the threonine enantiomers in water yielding the desired component (L-threonine) has been often chosen as a model system (Elsner et al., 2003 and 2005).

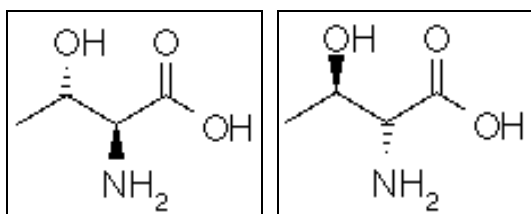


Fig. 3.1. Enantiomer structures: L-threonine (left) and D-threonine (right).

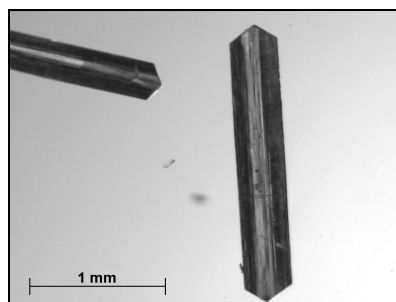


Fig. 3.2. Crystals of threonine (Elsner et al., 2005).

* Corresponding author. Tel.: +49-391-6718195; fax: +49-391-6712840.
E-mail address: oncuel@ovgu.de (A.A. Öncül).

The numerical analysis in this work is associated with computations in a homogeneous, time-dependent (zero-dimensional) reaction zone as well as with time-dependent computations in a continuously stirred batch reactor (CSBR). The obtained results are compared with the experimental data presented by Elsner et al. (2005).

A numerical model coupled with the standard method of moments (SMOM) is developed in order to describe the crystallization process. The method of moments has been first proposed by Hulburt and Katz (1964) as a simpler alternative method to the full population balance model (PBM, see e.g. Ramkrishna, 2000 and Ramkrishna and Mahoney, 2002). This method has been applied by several authors such as by Bałdyga and Orciuch (1997), Falk and Schaer (2001), Jaworski and Nienow (2003), Öncül et al. (2005) and Wei et al. (2001) in the modelling of crystallization processes. It has been further extended towards the quadrature method of moments (QMOM) by McGraw (1997) and the direct quadrature method of moments (DQMOM) by Fan et al. (2004). We have also implemented these two methods (QMOM and DQMOM). Nevertheless, since the SMOM has been already used in our previous chapter and validated by comparison with a semi-analytical solution of the numerical model (Öncül et al., 2005), we keep this simple method here. In this chapter, the results obtained by SMOM are compared with those obtained from the solution of the numerical model relying on the full population balance equation (PBE) for the zero-dimensional analysis. Comparisons with experimental data are also presented.

In addition to the investigation of the kinetic modelling (i.e. nucleation, growth etc.), the crystal size distribution (CSD) plots of the products at different times are shown since the size distribution of a crystalline product is an important criterion for assessing the properties and quality of the product (Mersmann, 1995). For this purpose we calculate the probability density function (PDF) of the threonine enantiomers, presuming its form to be a known mathematical function, such as a Gaussian or β -PDF (Heinz, 2003).

3.3 Modelling the crystallization

The homogeneous crystallization model is based on transport equations with source terms for chemical species and on the crystal size distribution expressed in terms of moment equations. These equations are defined in an external UDF (User-Defined Functions) file and compiled within the commercial CFD package FLUENT[®] 6.1.

The numerical model is developed taking into account the available experimental data of the crystallization process in a continuously stirred batch crystallizer. The aim is to examine the crystallization kinetics numerically by defining a perfect mixture in a time-dependent, zero-dimensional zone as well as in a real 3-dimensional geometry (CSBR) operating in unsteady-state.

In the first case (zero-dimensional analysis) no turbulence model is needed since the process is homogeneous and stationary. The only evolution of the system takes place as a function of time. Therefore, the numerical system is considerably simplified and the effects of the presence of the solid phase onto the flow field are automatically ignored.

In the second case, the flow is fully turbulent ($Re = 25\ 000$) in the batch reactor. We choose for the turbulence model the standard k - ϵ approach. The influence of micromixing is not considered here (Öncül et al., 2009).

The experiments have been described by Elsner et al. (2005). Initially, a saturated solution of the threonine enantiomers in water is present at a temperature of 40 °C. The solution is supersaturated by cooling down to 33 °C so that the driving force for the crystallization process is maintained. In order to establish the priority for the crystallization of the desired enantiomer (L-threonine), seed crystals of this enantiomer are added to the solution at the beginning. The process is stopped at a certain time, at which the crystallization of the undesired enantiomer (counter-enantiomer) starts, in order to prevent the drop in the purity of the desired enantiomer.

For the desired enantiomer a secondary nucleation process is assumed, which might be based on breakage or attrition, whereas primary nucleation is assumed for the counter-enantiomer. Moreover the crystal growth rate is assumed to be identical for both enantiomers. Furthermore it was also assumed

that there is no interdependence between the growth rate of one enantiomer and the supersaturation of the other enantiomer. In addition to these assumptions, the developed numerical model ignores possible aggregation and breakage situations as well.

3.3.1 Geometries and initial conditions

In FLUENT[®], it is not possible to perform a physically homogeneous (zero-dimensional) computation. That is why a two-dimensional reaction zone with 1x1 cm dimensions and 10x10 grid size is defined for the zero-dimensional time-dependent analysis of the crystallization. The dissolved threonine enantiomers and the seed crystals of the desired enantiomer are present in this zone initially at given amounts without any reaction.

The geometry and the dimensions of the three-dimensional CSBR are shown in Fig. 3.3. There are 4 baffles with a 90° arrangement around the reactor and 6 blades with a 60° arrangement on the Rushton-impeller disk. The rotation of the impeller is taken into account by using the sliding mesh model (SMM), already used by many authors (Bakker et al., 2000, Brucato et al., 1998, Ng et al., 1998 and Wei et al., 2001) and found to be suitable for the prediction of the flow patterns in stirred tanks. By this model it is possible to define a moving mesh zone including the impeller whereas the grid in the rest of the domain stays fixed. The interpolation of the variables between these two mesh regions is established through an interface boundary. A total number of 258,131 volume elements exist in the whole domain. The rotational speed of the batch reactor is set to 600 rpm and a perfect mixture of the dissolved threonine enantiomers including the L-threonine seed crystals is defined initially (there is therefore no need for injection of the seed crystals).

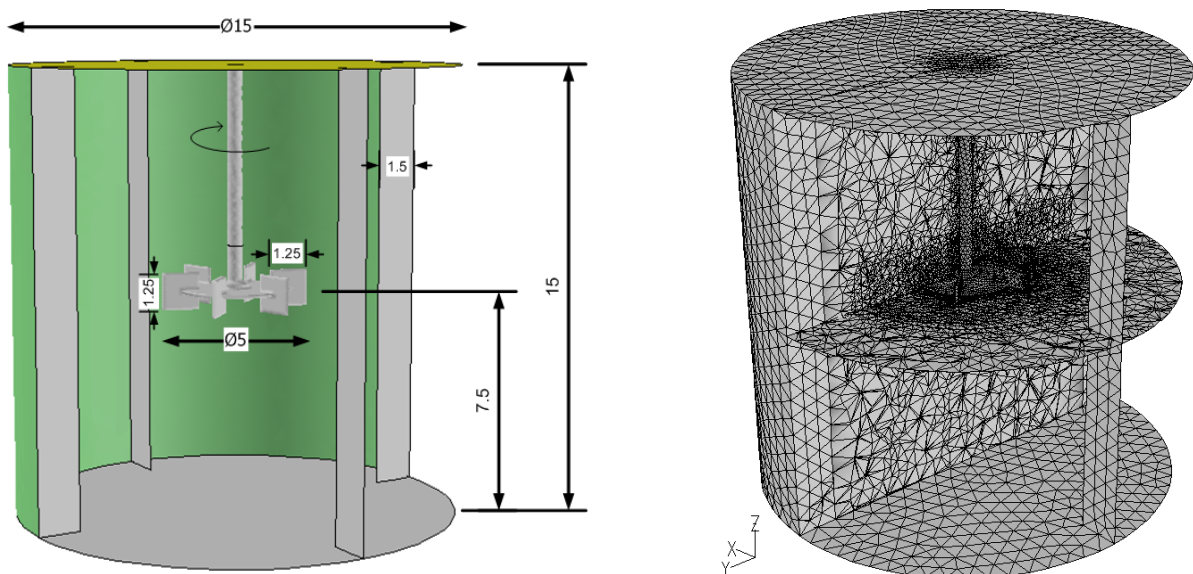


Fig. 3.3. The geometry, dimensions (in cm) and grid for the batch crystallizer.

The seed crystals exist with a known initial number distribution function in both cases. The corresponding distribution is fitted to the data obtained by experimental observations. These data and the fitted function are given later in Fig. 3.6.

3.3.2 Crystallization kinetics and model equations

The standard Reynolds-averaged Navier-Stokes equations are applied by FLUENT[®] as the transport equation of an arbitrary scalar, ϕ .

$$\frac{\partial(\rho\phi)}{\partial t} + \nabla \cdot (\rho \mathbf{u} \phi - \Gamma_{eff} \nabla \phi) = S_\phi \quad (3.1)$$

The effective turbulent diffusivity, Γ_{eff} , is computed by dividing the effective viscosity, μ_{eff} , with the turbulent Schmidt number, Sc_t , which is assumed here to be equal to 0.7. In the zero-dimensional analysis the diffusion and the convection terms in Eq. (3.1) are automatically ignored since the relevant calculations are independent of the external coordinates. Hence, the transport equation in this case simplifies into the following form:

$$\frac{\partial(\rho\phi)}{\partial t} = S_\phi \quad (3.2)$$

A total number of 16 user-defined scalars (UDS) are implemented in the UDF file representing the chemical species (i) in terms of mass, M_i , and the four first moments, $\mu_{j,i}$, with $j = 0$ up to 3.

The source term for the chemical species, S_{M_i} , is related to the specific crystal growth rate, S_g (assuming that the density of the transporting fluid, ρ , is not changing), with a "-" sign for the components in the liquid phase and a "+" sign for those in the solid phase. The specific crystal growth rate is further related to the second moment of the crystal size distribution of the corresponding enantiomer, $\mu_{2,i}$:

$$\frac{S_{M_i}}{\rho} = S_g = \pm (3\mu_{2,i} G_i) k_v \rho_{thr} \quad (3.3)$$

where k_v and ρ_{thr} represent the volumetric crystal shape factor and the density of the threonine crystals, respectively.

The source term for the crystal size distribution moments is computed according to the following equation, taking the first four moments into account:

$$\frac{S_{\mu_{j,i}}}{\rho} = 0^j B_i + j G_i \mu_{j-1,i} \quad (j = 0-3) \quad (3.4)$$

The mass fraction of each enantiomer dissolved in water is defined by the following expression:

$$Y_i = \frac{M_i}{M_{total}} \quad (3.5)$$

where M_{total} represents the total mass of the enantiomers in the liquid phase plus the mass of water:

$$M_{total} = M_{L-thr} + M_{D-thr} + M_{water} \quad (3.6)$$

Accordingly, the supersaturation ratio of the dissolved enantiomers can be defined as a function of the mass fractions and of the saturation concentrations:

$$S_i = \frac{Y_i}{C_{sat_i}} \quad (3.7)$$

In the equation above, the saturation concentration of an enantiomer i , C_{sat_i} , is defined by the following expression:

$$C_{sat_i} = sc_{i,1} - (sc_{i,2} Y_k) \quad (3.8)$$

where the subscript k denotes the opposite enantiomer and the sc values represent the constants at 33 °C for this linear interpolation.

The crystal growth rate, G_i , and the nucleation rate, B_i , are calculated as functions of the supersaturation ratio, S_i :

$$G_i = k_g (S_i - 1)^g \quad (3.9)$$

$$B_{L-thr} = k_{b,L} (S_L - 1)^{b_L} \mu_{3,L} \quad (3.10)$$

$$B_{D-thr} = k_{b,D} e^{\left(\frac{-b_D}{\ln(S_D)^2}\right)} \quad (3.11)$$

where k_g and $k_{b,i}$ indicate the growth rate and nucleation rate constants respectively. Moreover, the constants g and b_i are the growth rate and the nucleation rate exponents, respectively. The values of all parameters and constants expressed in the above equations are listed in Table 3.1.

Table 3.1. List of all parameters and constants used in the numerical modelling

| Parameter | Value | Unit |
|--------------------------|-----------------------|----------------------|
| ρ_{water} | 1000 | kg/m ³ |
| μ_{water} | 1x10 ⁻³ | kg/(m s) |
| M_{water} | 0.8017 | kg |
| $M_{L-thr,initial}$ | 0.09915 | kg |
| $M_{D-thr,initial}$ | 0.09915 | kg |
| $M_{L-thr,seed,initial}$ | 2.5x10 ⁻³ | kg |
| $\mu_{0,L-thr,seed}$ | 22421 | – |
| $\mu_{1,L-thr,seed}$ | 27.058 | m |
| $\mu_{2,L-thr,seed}$ | 0.04 | m ² |
| $\mu_{3,L-thr,seed}$ | 6.94x10 ⁻⁵ | m ³ |
| ρ_{thr} | 1250 | kg/m ³ |
| k_v | 0.0288 | – |
| g | 0.73 | – |
| k_g | 2.31x10 ⁻⁷ | m/s |
| b_L | 2.07 | – |
| $k_{b,L}$ | 3x10 ⁸ | 1/(m ³ s) |
| b_D | 0.029 | – |
| $k_{b,D}$ | 590 | 1/s |
| $sc_{L,1}$ | 0.0985 | – |
| $sc_{L,2}$ | 0.0072/0.0913 | – |
| $sc_{D,1}$ | 0.0986 | – |
| $sc_{D,2}$ | 0.0073/0.0913 | – |

In addition to all the equations above, three more equations characterising the crystal size distributions of the enantiomers are also computed during the simulations. These are the number-averaged crystal size,

$$L_{1,0} = \frac{\mu_1}{\mu_0} \quad (3.12)$$

the coefficient of variation which is used to represent the width of the crystal size distribution,

$$cv = \left(\frac{\mu_0 \mu_2}{\mu_1^2} - 1 \right)^{1/2} \quad (3.13)$$

and the standard deviation, σ , (or the square root of the population variance, σ^2) that is simply the product of the number-averaged crystal size with the coefficient of variation:

$$\sigma = cvL_{1,0} \quad (3.14)$$

These last three equations are used to reconstruct the CSD plots during the post-processing stage of the work. Once the number density function, $n(L)$, is reconstructed, the mass density function, $m(L)$, is consequently calculated by:

$$m(L) = n(L)k_v\rho_{thr}L^3 \quad (3.15)$$

3.3.3 Numerical calculations

The numerical calculations are performed for zero- and three-dimensional time-dependent cases as described above by employing FLUENT[®] 6.1 and the compiled UDF file.

During the zero-dimensional calculations an adaptive time-step method is used in such a way that the time-step is quite small (in order of 10^{-11} s) at the beginning of the process and slowly increasing up to a certain value (max. 1 min) as L-threonine crystallizes. At each time-step the iterations are carried out until the residuals fall below the value 0.001. The computations take about 10 minutes under these circumstances by employing a single Pentium-IV Linux PC (2.7 GHz/2 GB memory).

On the other hand the 3-dimensional computations are performed in two stages. In the first stage the flow field is simulated with a certain constant time-step and without any chemical species. According to the sliding mesh model this time-step must be chosen in such a way that a volume element in the rotating mesh region should not pass more than one volume element in the stationary mesh region at the interface boundary. This is essential for the correct execution of the interpolation between the two mesh regions. For the turbulence model, the $k-\varepsilon$ approach has been used since this model should supply a reasonable accuracy and short computing times for such a flow configuration. This model is recommended e.g. by Brucato et al. (1998) and Montante and Bakker (2004) for such baffled tanks in which no strong, swirling flow occurs. Each time-step is continued until the residuals fall below 0.0001 for continuity and 0.001 for the other variables. The simulation at this stage converges in about 8 days on the same PC as above. After having obtained the proper flow field (i.e. the right flow periodicity), the chemical species and the crystallization process are implemented by activating the UDF. In this second stage the flow and the turbulence model are switched off in order to reduce the computational times. This is obtained by defining a time-step as a multiple of one impeller rotational time in order to keep the same location of the impeller and the same velocity field. The limits for the maximum absolute residuals are set to 0.001 for the variables. This further computation took about 40 hours. Note that this decoupling between the flow and the separation process is only possible due to the very different time-scales between both physical processes, so that the flow appears to be frozen for the crystallization.

For both cases, 1st-order discretization is used in space and a 2nd-order implicit time formulation is chosen for the three-dimensional analysis. All computations are carried out until 300 minutes of real

time. This corresponds in the experiments to the time at which the purity of the L-threonine starts to decrease noticeably due to the newly nucleating counter-enantiomer.

3.4 Results and discussion

3.4.1 Zero-dimensional analysis

The mass profiles for the components obtained from the zero-dimensional numerical calculations using the previously explained SMOM with 4 moments are presented in Fig. 3.4. These profiles represent qualitatively quite logical results, which could also be expected from the chemical kinetics point of view. As it can be seen from the figure, L-threonine starts to crystallize immediately at the beginning whereas the noticeable generation of D-threonine starts first at around 250 min, in agreement with experimental observations. Until this time a considerable purity of the desired product, L-threonine, can be achieved. The priority of the crystallization of the L-threonine is due to the fact that a surface for the crystallization process of this enantiomer is offered initially through the presence of the seed crystals, as explained previously.

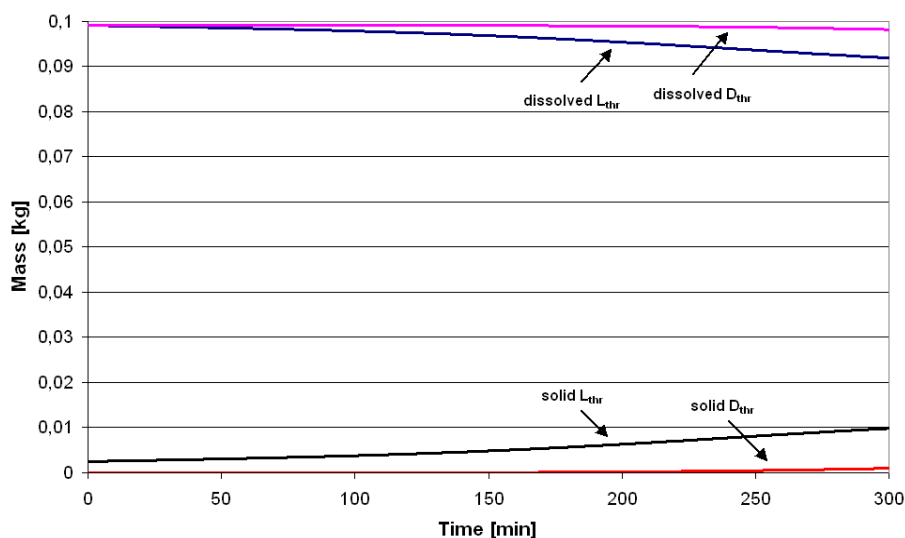


Fig. 3.4. Mass profiles of the chemical components.

In Fig. 3.5 the nucleation rates for both enantiomers are represented as a function of time. It is worth noting that both nucleation rates increase at the beginning (due to high supersaturation) and after a certain point (at around 100 min) they start to decrease (due to decreasing supersaturation).

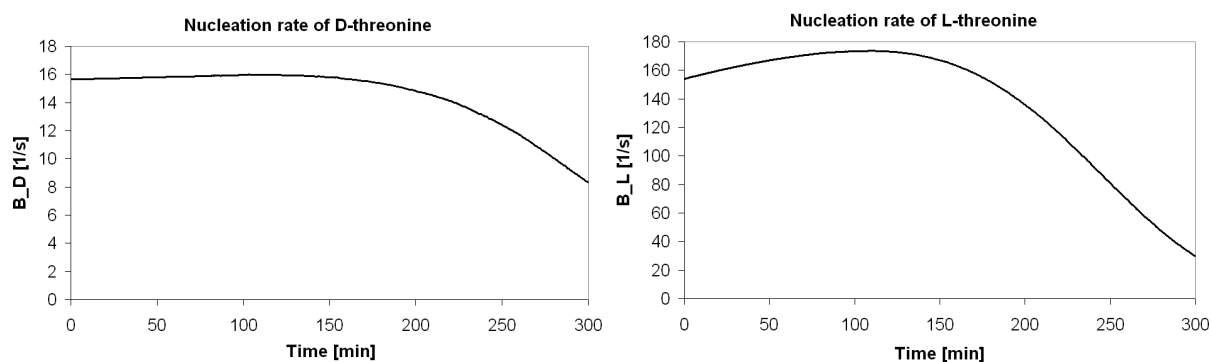


Fig. 3.5. Nucleation rate profiles of the enantiomers.

The most important point among the results is actually the comparison of the reconstructed CSDs obtained using the SMOM with those obtained by experimental and full PBE-based numerical investigations. In Fig. 3.6 the CSD plots for the seed crystals are shown in comparison with the experimental data, demonstrating an excellent agreement. The CSD curve shifts in time towards the bigger particle size region since the seeds grow with time, as expected. Here, the seed CSD plots are drawn using the assumption that the distribution follows a β -function shape. This assumption is made since the measured function for the initial seeds already showed a form quite similar to a β -PDF. A small drop in the total number of crystals can be seen when the upper parts of the CSD curves are observed. In an ideal case this situation is not expected since it was assumed that the number of the seed crystals is not changing (no agglomeration or breakage). This result is most probably due to the numerical error induced by the reconstruction of the CSDs using the first three moments.

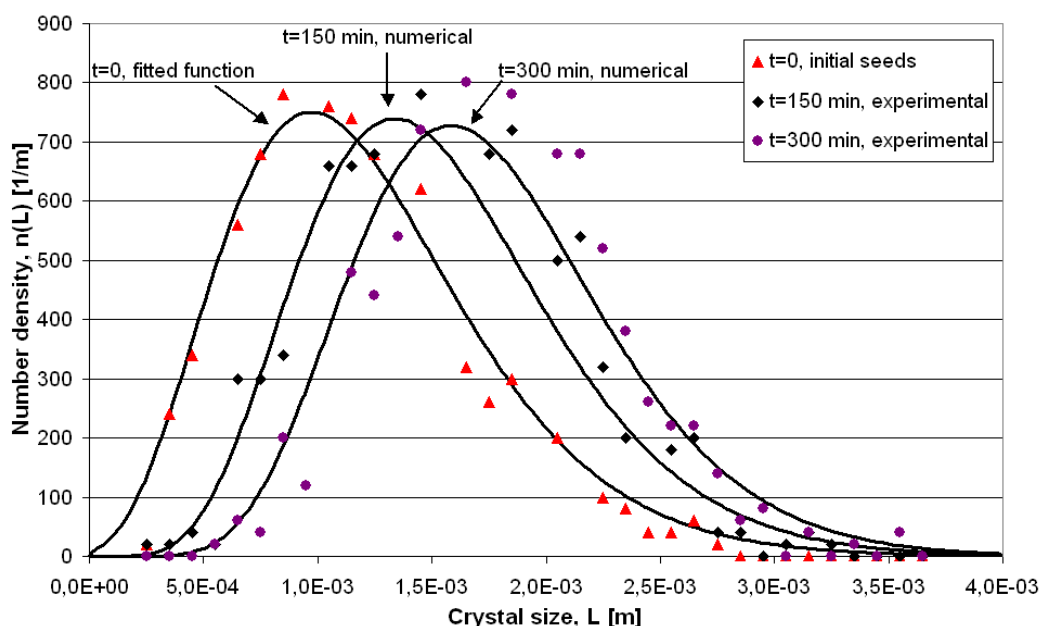


Fig. 3.6. CSD plots of the seed crystals (L-threonine) at different time instants, comparing experimental and numerical data. Solid curves correspond to our computation.

In Fig. 3.7, mass density plots for both enantiomers are shown for both numerical methods, full PBE and SMOM in comparison. The reconstructed CSDs according to the SMOM are based on a Gaussian shape (for the nucleated crystals), resp. on β -PDFs (for the seed crystals), as above. As it can be seen, the reconstructed CSD plots represent again a very good approximation of the results obtained by using the full population balance equations. Here, it is worth noting that there is one single CSD curve representing the full PBE for L-threonine since the whole size distribution (both for nucleated and seed crystals) is computed as a single function in this case. On the other hand the nucleated and the seed crystals are separately reconstructed for L-threonine when using the first three moments according to SMOM. This is essential to reconstruct the CSD properly, since such classical functions accept only one single peak value and can not represent such a two-peaked CSD curve. Moreover, two different shapes are used for different types of particles, as mentioned above: a Gaussian-PDF for the nucleated crystals and a β -PDF for the seed crystals. By this way the numerical results obtained with the SMOM correspond much better to the experimental data, as demonstrated in Fig. 3.8.

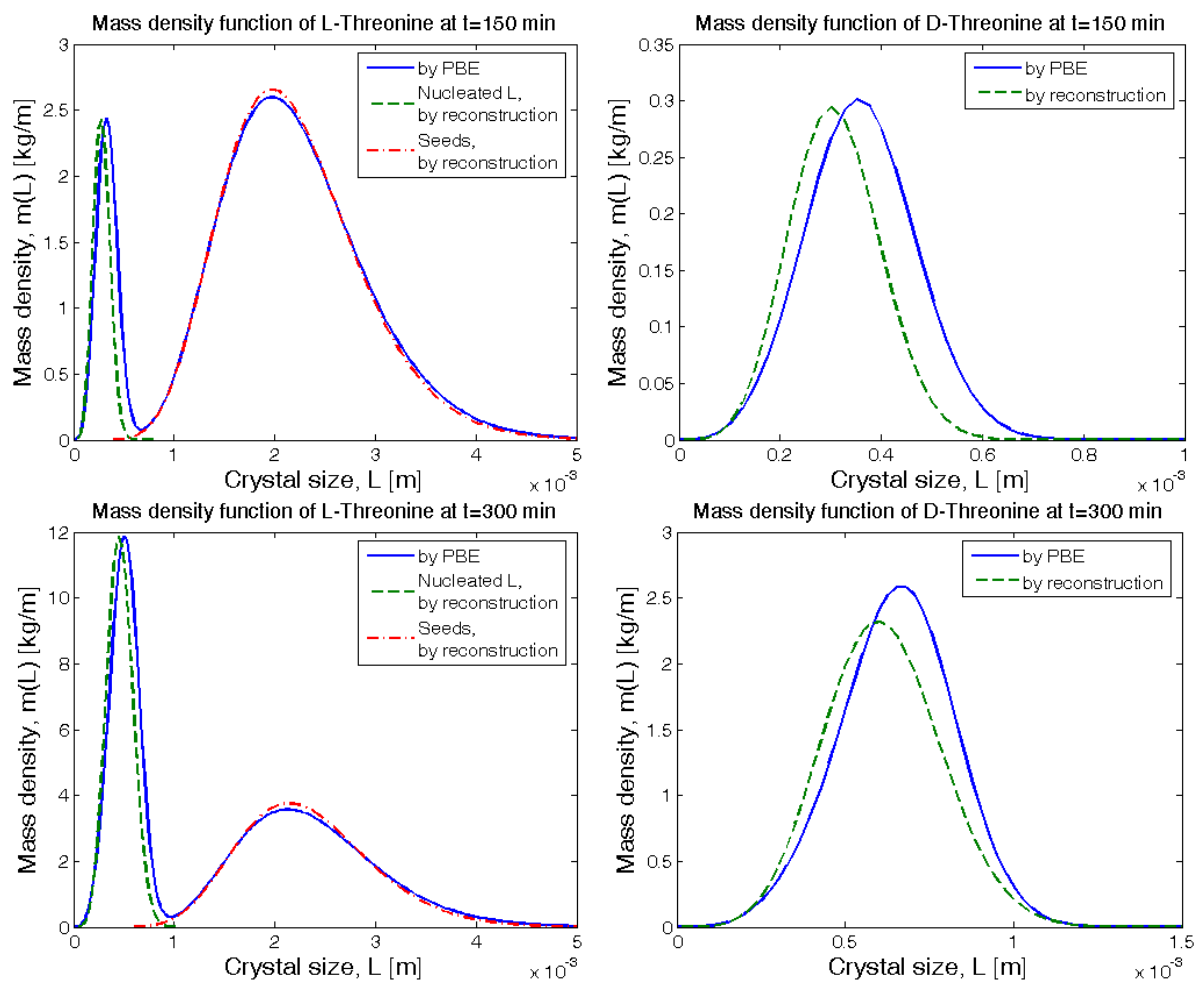


Fig. 3.7. Mass density plots for both enantiomers at different time instants, comparing results obtained by full PBE and SMOM (0-D analysis).

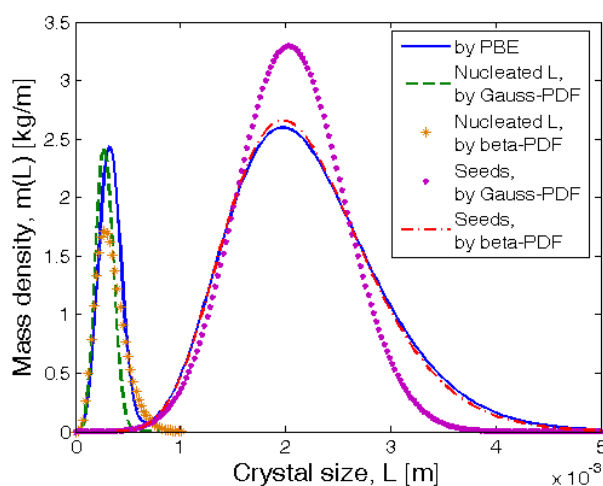


Fig. 3.8. CSD plots for full PBE and SMOM for different presumed PDF shapes (L-threonine at $t = 150$ min).

Although the plots given in Fig. 3.7 represent quite good results, some discrepancies are observed in the CSDs of the nucleated threonine of both enantiomers when comparing both numerical approaches. The most obvious discrepancy is the difference in the mean sizes of the nucleated crystals.

This is actually caused by the assumption of a prescribed PDF shape when using the SMOM. These discrepancies can be better seen when the number density plots are shown (Fig. 3.9). For this quantity the reconstructed curve presents a poor agreement especially for a crystal size below 300 μm . Hence, the observed discrepancies in the CSDs of the nucleated crystals originate at this stage, which indirectly controls the mass density functions since they are calculated by using the number density functions (Eq. (3.15)).

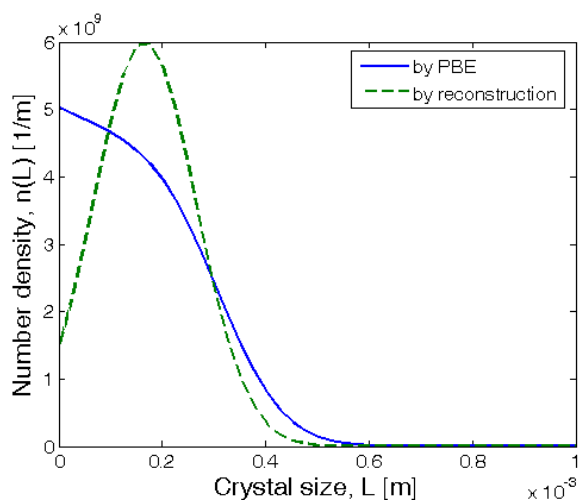


Fig. 3.9. Number density functions for full PBE and SMOM in comparison (L-threonine at $t = 150$ min).

3.4.2 Three-dimensional computation

The velocity vector plots and the turbulent energy, k , contour plots according to the first-stage simulation (considering only the flow field) performed for the CSBR are shown in Figs. 3.10 and 3.11 respectively. The flow field is consistent with experimental and numerical results in the literature (e.g. Bakker et al., 2000, Brucato et al., 1998, Lamberto et al., 1996, Lamberto et al., 2001, Montante et al., 2001 and Ng et al., 1998).

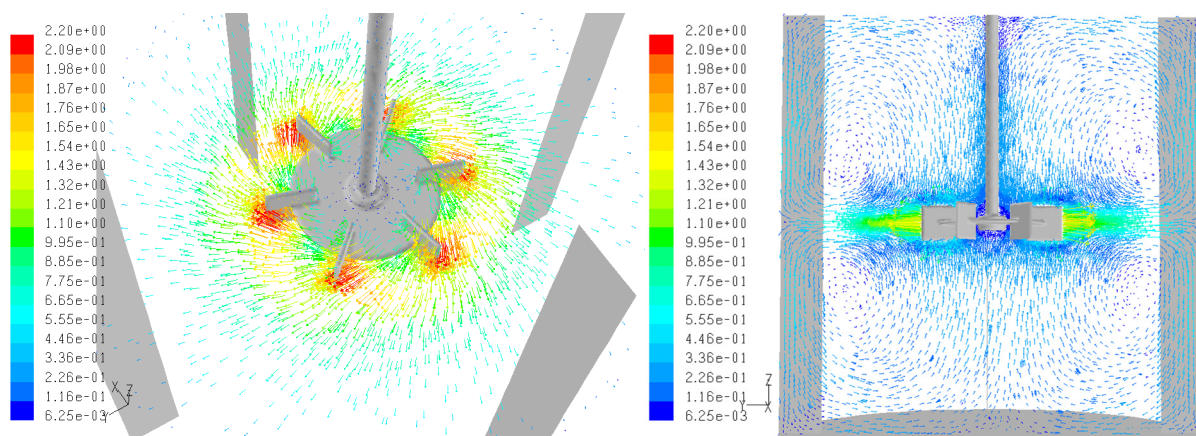


Fig. 3.10. Velocity vectors (m/s) around the impeller (left) and on the middle cross-sectional surface of the reactor (right).

According to the second-stage simulation (including only the crystallization on top of a frozen flow), an almost homogeneous concentration distribution of all chemical components is observed. This is due to the fact that the mixture is homogeneous at the beginning of the process, including the seed

crystals and that the particles are not highly affected by the gravity since they are not very dense ($\rho_{thr} = 1250 \text{ kg/m}^3$) with respect to the solvent (water) and since the mixing effect of the impeller is high enough (600 rpm, $Re = 25\,000$). The CSD plots obtained by the full PBE for the zero-dimensional case and by the reconstruction according to SMOM in three dimensions are shown in Fig. 3.12 for comparison. These data again show a good agreement, demonstrating that three-dimensional effects are quite negligible in this configuration.

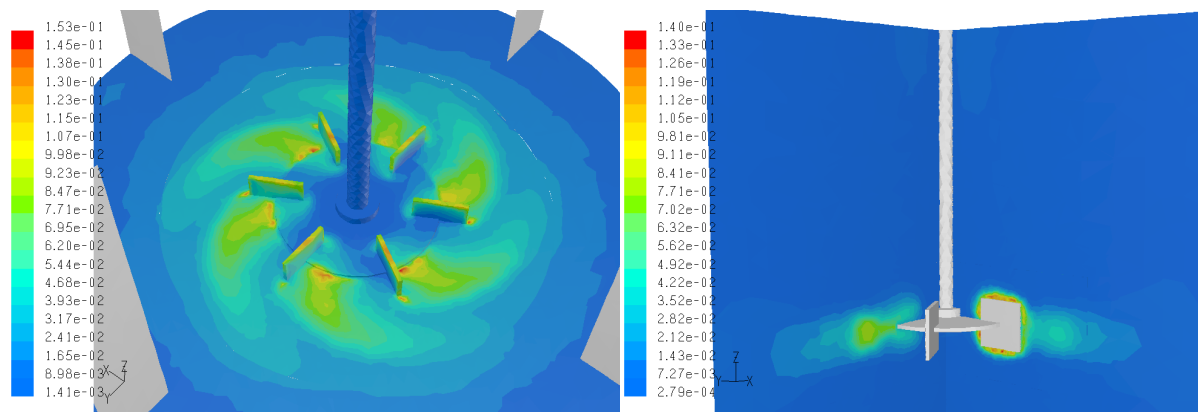


Fig. 3.11. Turbulent kinetic energy (m^2/s^2) around the impeller (left) and on two perpendicular planes (right).

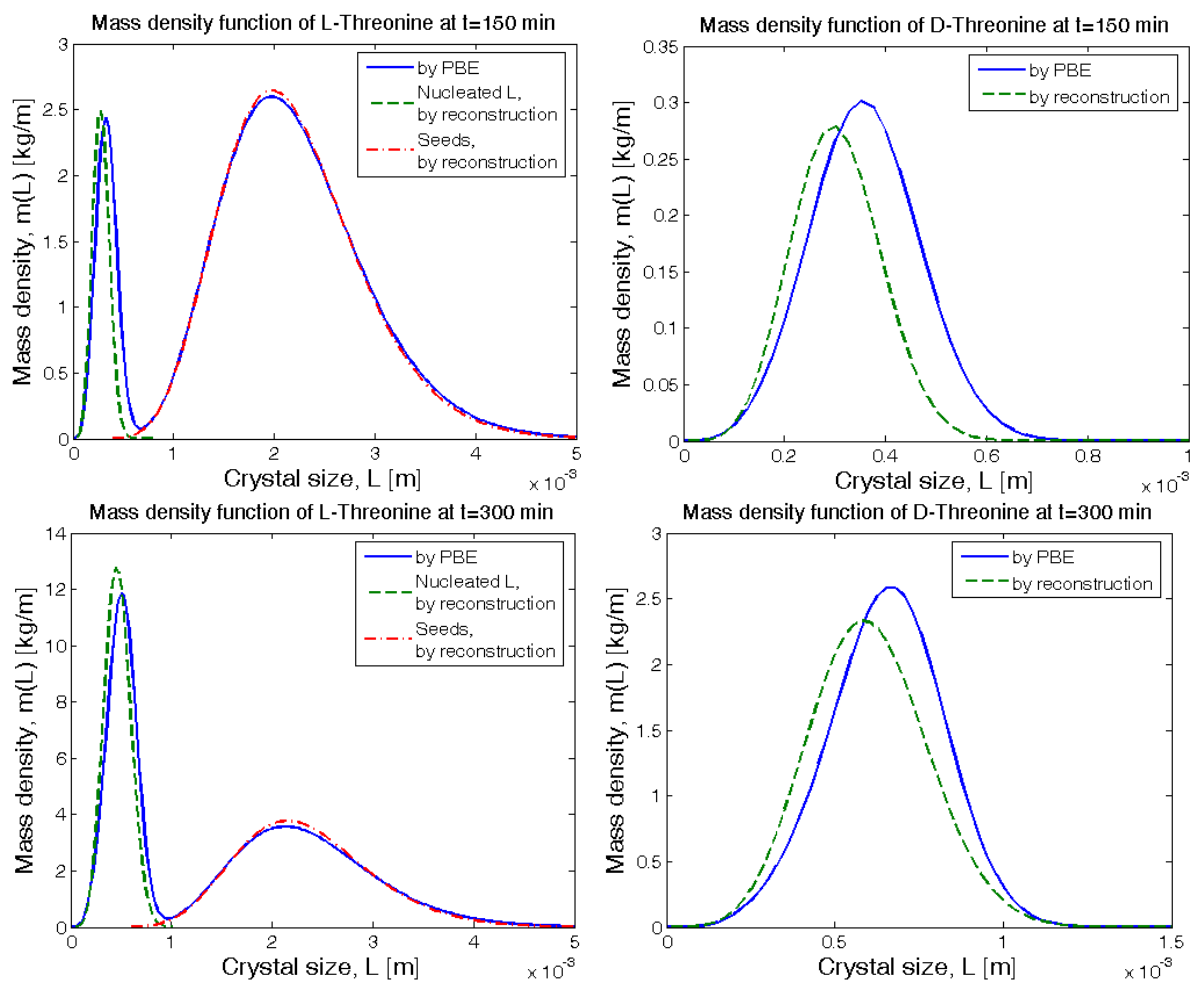


Fig. 3.12. Mass density plots for both enantiomers at different time instants for full PBE (zero-dimensional analysis) and SMOM (3-D analysis) in comparison.

3.5 Conclusions and remarks

The aim of this work was to perform time-dependent numerical calculations for homogeneous crystallization processes in a perfectly mixed crystallization zone (zero-dimensional analysis) and in a CSBR (full three-dimensional analysis), and consequently to determine the mass profiles and the crystal size distributions of the threonine enantiomers. A numerical model has been developed based on the classical method of moments and compiled into FLUENT[®] 6.1. For the corresponding PBM, two-population balance approach was applied based on SMOM. The obtained results have been thereafter compared with experimental data and with alternative numerical calculations based on the full population balance equations. According to the results it can be concluded that the developed numerical model supplies excellent data as far as homogeneous terms are concerned.

The three-dimensional simulation has been performed in two stages in order to minimize the computational time. In the first stage the flow field has been calculated until reaching flow periodicity. The resulting flow field has been found to be fully consistent with data presented in the literature. In the next stage the flow field has been kept at a corresponding fixed impeller position and only the crystallization kinetic has been calculated. By freezing the flow in this way, the computations have been considerably accelerated. The same approach will be used in further chapters.

From the mass profiles it is obvious that the process is quite slow and should be interrupted at around 250 min in order to preserve the high purity of the desired product, L-threonine. The small discrepancies observed in the CSDs between the full PBE- and SMOM-based calculations are most probably due to the assumption that the reconstructed PDFs according to the SMOM are common mathematical functions such as Gaussian or β -functions. Nevertheless, the mass density plots obtained by these two methods have been found to be highly consistent with each other, especially for the seed crystals of the L-threonine. Moreover, the number distributions of the seed crystals at different time instants correspond well to the experimental data presented by Elsner et al. (2005).

From the population dynamics point of view, the formulation of a two-population balance model in the CFD computations via in-house built UDS and UDF has been successfully demonstrated during this study. This experience will be very useful for a similar application considering the cultivation of animal cells in the further studies.

References of Chapter 3

- Bakker, A., LaRoche, R.D., Wang, M.H., Calabrese, R.V. (2000). Sliding mesh simulation of laminar flow in stirred reactors. *The Online CFM Book at <http://www.bakker.org/cfm>*.
- Baldyga, J., Orciuch, W. (1997). Closure problem for precipitation. *Trans. Inst. Chem. Eng.*, 75, 160-170.
- Brucato, A., Ciofalo, M., Grisafi, F., Micale, G. (1998). Numerical prediction of flow fields in baffled stirred vessels: a comparison of alternative modelling approaches. *Chem. Eng. Sci.*, 53, 3653-3684.
- Elsner, M.P., Fernández Menéndez, D., Alonso Muslera E., Seidel-Morgenstern, A. (2005). Experimental study and simplified mathematical description of preferential crystallisation. *Chirality*, 17, S183-S195.
- Elsner, M.P., Lorenz, H., Seidel-Morgenstern, A. (2003). Enantioseparation using crystallization by entrainment – some engineering aspects. *AIChE Annual Meeting*, San Francisco, September, 16th – 21st 2003.
- Falk, L., Schaer, E. (2001). A PDF modelling of precipitation reactors. *Chem. Eng. Sci.*, 56, 2445-2457.
- Fan, R., Marchisio, D.L., Fox, R.O. (2004). Application of the direct quadrature method of moments to polydisperse gas-solid fluidized beds. *Powder Technol.*, 139, 7-20.
- Heinz, S. (2003). *Statistical mechanics of turbulent flows*. Berlin: Springer Verlag.
- Hulburt, H.M., Katz, S. (1964). Some problems in particle technology: A statistical mechanical formulation. *Chem. Eng. Sci.*, 19, 555-574.
- Jaworski, Z., Nienow, A. (2003). CFD modelling of continuous precipitation of barium sulphate in a stirred tank. *Chem. Eng. J.*, 91, 167-174.
- Lamberto, D.J., Alvarez, M.M., Muzzio, F.J. (2001). Computational analysis of regular and chaotic mixing in a stirred tank reactor. *Chem. Eng. Sci.*, 56, 4887-4899.
- Lamberto, D.J., Muzzio, F.J., Swanson, P.D. (1996). Using time-dependent RPM to enhance mixing in stirred vessels. *Chem. Eng. Sci.*, 51, 733-741.
- McGraw, R. (1997). Description of aerosol dynamics by the quadrature method of moments. *Aerosol Sci. Technol.*, 27, 255-265.
- Mersmann, A. (1995). *Crystallization technology handbook*. New York: Marcel Dekker Inc.
- Montante, G., Bakker, A. (2004). Stirring up the phases in tall tanks. *Fluent News – Fall 2004*, XIII(2), 8-9.
- Montante, G., Lee, K.C., Brucato, A., Yiannekis, M. (2001). Experiments and predictions of the transition of the flow pattern with impeller clearance in stirred tanks. *Comput. Chem. Eng.*, 25, 729-735.
- Ng, K., Fentiman, N.J., Lee, K.C., Yiannekis, M. (1998). Assessment of sliding mesh CFD predictions and LDA measurements of the flow in a tank stirred by a Rushton impeller. *Trans. Inst. Chem. Eng.*, 76, 737-747.
- Öncül, A.A., Janiga, G., Thévenin, D. (2009). Comparison of various micromixing approaches for computational fluid dynamics simulation of barium sulfate precipitation in tubular reactors. *Ind. Eng. Chem. Res.*, 48, 999-1007.
- Öncül, A.A., Sundmacher, K., Seidel-Morgenstern, A., Thévenin, D. (2006). Numerical and analytical investigation of barium sulphate crystallization. *Chem. Eng. Sci.*, 61, 652-664.
- Ramkrishna, D. (2000). *Population balances, theory and application to particulate systems in engineering*. New York: Academic Press.
- Ramkrishna, D., Mahoney, A.W. (2002). Population balance modelling: Promise for the future. *Chem. Eng. Sci.*, 57, 595-606.
- Wei, H., Wei, Z., Garside, J. (2001). Computational fluid dynamics modelling of the precipitation process in a semibatch crystalliser. *Ind. Eng. Chem. Res.*, 40, 5255-5261.

Chapter 4

Model reduction: Microemulsion precipitation of barium sulphate

4.1 Introduction

For many applications, for instance for the bioreactor considered in further chapters, it is usually impossible to solve directly the full three-dimensional, unsteady flow together with all important populations. Therefore, model reduction techniques must be developed and compared to the full solution. This is first done here for a simpler problem: microemulsion precipitation.

Nanoparticle production using microemulsion droplets has become a very interesting technique in the recent years. It allows a controlled adjustment of the particle size, which is an essential task due to the highly size-dependent properties of nanoparticles. The present study deals with the formation of BaSO_4 nanoparticles by precipitation of ionic reactants in microemulsion systems.

The aim of this study was to apply a reduced PBM for the CFD simulation of microemulsion precipitation of BaSO_4 in a semi-batch reactor. For this purpose, a PBM framework based on discrete coordinates was derived and afterwards an appropriate reduction concept was applied to obtain an efficient numerical solution. Although the resulting zero-dimensional (spatially homogeneous) calculations performed by MATLAB[®] 7.0 showed a qualitatively good agreement with the experimental data for stoichiometric conditions, larger deviations were observed for cases with a high concentration excess of one reactant inside the microemulsion droplets. Nevertheless, the reduced PBM was validated up to an acceptable degree via this initial analysis.

The observed deviations might result from the fact that the precipitation rate strongly depends on the local supersaturation. High concentration differences, especially near the feed led to large local variations of the supersaturation profile. Thus, CFD simulations were performed for a refined analysis. This was managed by implementing the reduced PBM in the commercial CFD code FLUENT[®] 6.2 via UDS and UDF. By this way, it became possible to investigate the reaction process for various three-dimensional inhomogeneous hydrodynamic conditions with acceptable computational times. The obtained results were finally compared with the homogeneous calculation results and with the experiments. Moreover, local variations within the reactor were also examined.

Related publication

This chapter builds on top of:

CFD modelling of BaSO₄ precipitation inside microemulsion droplets in a semi-batch reactor

Alper A. Öncül^{a,*}, Björn Niemann^b, Kai Sundmacher^{b,c}, Dominique Thévenin^a

Chemical Engineering Journal (2008) 138:498-509

^a*Institut für Strömungstechnik und Thermodynamik, Lehrstuhl für Strömungsmechanik und Strömungstechnik (ISUT/LSS), Otto-von-Guericke-Universität-Magdeburg, Universitätsplatz 2, D-39106 Magdeburg, Germany*

^b*Max-Planck-Institut für Dynamik komplexer technischer Systeme, Sandtorstrasse 1, D-39106 Magdeburg, Germany*

^c*Institut für Verfahrenstechnik, Lehrstuhl für Systemverfahrenstechnik (IVT/SVT), Otto-von-Guericke-Universität-Magdeburg, Universitätsplatz 2, D-39106 Magdeburg, Germany*

4.2 State of the art

The production of nanoparticles with well-defined properties of the resulting particle size distribution (PSD) is a challenging task for current research. An exact size control is an important issue due to the strong size dependence of chemical and physical nanoparticle properties resulting from quantum effects (Luther, 2004). A strong influence on, e.g. melting point, fluorescence spectrum or chemical activity has been observed for a variety of materials when the particle size is below 100 nm. A promising and on laboratory scale well-established wet chemistry process, which allows an accurate size control during the production, is the precipitation of nanoparticles inside the water droplets of a microemulsion. Many different materials like semiconductors, metals, metal oxides, borides, carbonates and sulphates have already been successfully produced by this method (see overview by Niemann et al., 2006). An example for the quality of the produced nanoparticles is given in Fig. 4.1a. The shown BaSO₄ particles have a very narrow size distribution with a mean particle diameter of approximately 6.5 nm. Adityawarman et al. (2005) showed in their experimental study that the mean particle diameter can be precisely adjusted between 6 and 35 nm by this technique.

The main reason for this excellent suitability of the microemulsion technique for the production of tailored nanoparticles is the adjustment of well-defined conditions for nucleation and growth by the limited amount of reactants inside the nano-sized droplets. The primarily formed nuclei, which consist only of a few molecules, are protected by the surrounding surfactant monolayer against uncontrolled growth and agglomeration. Thus, the formation of bigger particles by growth is completely governed by the droplet exchange, which provides new reactants in small amounts of a few molecules from other droplets. A schematic illustration of the particle formation mechanism for ionic reactants (salts) is given in Fig. 4.1b.

Process models for the microemulsion system are usually very complex due to the high number of distributed properties which result in multi-dimensional partial differential equations with integral terms. Solutions by discretization of deterministic population balance models and simulations of stochastic Monte-Carlo models have been presented in literature (see overview by Niemann et al., 2006). They show a good agreement between laboratory-scale experiments and simulations for the

* Corresponding author. Tel.: +49 391 6718195; fax: +49 391 6712840.
E-mail address: oncuel@ovgu.de (A.A. Öncül).

ideally-mixed case. However, the computational demand is so high that it is practically impossible to take into account inhomogeneous hydrodynamic conditions. In order to analyse and improve the process on a technical scale, it is nevertheless important to consider real flow conditions, as obtained numerically by CFD. For such coupled studies reasonable model reductions have to be performed to decrease the computational effort. Therefore, a first reduced numerical model has been derived and implemented within an industrial CFD code in a previous work (Öncül et al., 2006). This tool has been used to investigate the stoichiometric reaction process for three-dimensional inhomogeneous hydrodynamic conditions with reasonable computation times.

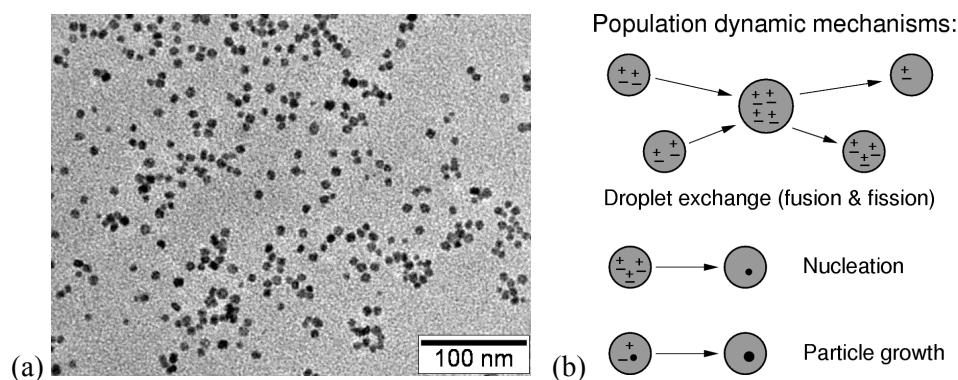


Fig. 4.1. (a) BaSO₄ nanoparticles produced by microemulsion precipitation (see details in the next section). (b) Important population dynamic mechanisms for the nanoparticle formation by precipitation of ionic reactants in microemulsion systems.

Similar modelling studies for emulsions can be found in the literature. For instance, an emulsion polymerization process has been modelled for batch as well as semi-batch systems by Min and Ray (1978) and Unzueta and Forcada (1997). Moreover, the application of a reduced model for an optimal control of population balances is presented by Kiparissides (2006). Vale and McKenna (2005) investigated the coupling of the flow field simulation with compartments method for the modelling of an emulsion polymerization in batch and continuous reactors. Recently, Singh and Kumar (2006) modelled a microemulsion nanoparticle precipitation and validated their simplified model with the results of exact Monte-Carlo simulations.

4.3 Experimental setup

Experimental results by Adityawarman et al. (2005) are used for the validation of the simulations. These authors investigated the nanoparticle precipitation of barium sulphate (BaSO₄) according to the following reaction scheme:



The two reactants BaCl₂ and K₂SO₄ were separately dissolved inside the water droplets of two identically composed microemulsions (continuous oil phase: cyclohexane, non-ionic technical surfactant: Marlipal O13/40). The droplets are almost monodisperse and their mean diameter is approximately 5 nm (Adityawarman et al., 2005). The precipitation experiments were performed in semi-batch operation mode in a Rushton-type stirred tank reactor with a 6-blade impeller rotating at 300 rpm in the clockwise direction (Re = 4,500) and with 18 baffles (Adityawarman et al., 2005; Niemann et al., 2006). The microemulsion containing the dissolved K₂SO₄ was filled inside the reactor and the second microemulsion with the dissolved BaCl₂ was added to the reactor with a constant feed rate. The influence of the initial concentrations of the two reactants inside the droplets on the final particle size distribution has been analyzed in detail. Therefore two sets of experiments have been

performed. Within the first set the concentration of BaCl_2 in the feed was reduced stepwise from 0.1 to 0.01 mol/L while the concentration of K_2SO_4 was kept constant at 0.1 mol/L. In the second set the concentration of BaCl_2 in the feed was kept constant at 0.1 mol/L and the concentration of K_2SO_4 inside the reactor was reduced stepwise from 0.1 to 0.01 mol/L. The exact parameters of the five experiments investigated in this work are shown in Table 4.1.

Table 4.1. List of experiments used in this work

| Case | $\text{K}_2\text{SO}_4, c_{\text{reactor}}$ (mol/L) | $\text{BaCl}_2, c_{\text{feed}}$ (mol/L) |
|------|---|--|
| A | 0.1 | 0.1 |
| B1 | 0.1 | 0.05 |
| B2 | 0.1 | 0.01 |
| C1 | 0.05 | 0.1 |
| C2 | 0.01 | 0.1 |

As a result of these experiments the influence of the initial concentration difference $\Delta c(t=0) = |c_{\text{reactor}} - c_{\text{feed}}|$ as a control parameter for the final particle size is identified. It could be shown that an increase of $\Delta c(t=0)$ leads to an increase of the final particle size. Detailed results are shown later on together with the comparison between experiments and simulations. A list of all important parameters used in the experiments is given in Table 4.2.

Table 4.2. Parameters of the experiments

| Parameter | Value |
|---|--------|
| Droplet diameter, d_D (nm) | 5 |
| Feed rate, \dot{V}_{feed} (mL/min) | 35 |
| Feeding time, t_{feed} (s) | 257.14 |
| Temperature, T (K) | 298.15 |
| Volume of the microemulsion inside the reactor, V_{reactor} (mL) | 150 |
| Volume of the microemulsion of the feed, V_{feed} (mL) | 150 |

4.4 Numerical model

The dynamics of the nanoparticle precipitation inside microemulsion droplets are investigated according to three internal coordinates (distributed properties) and the three external coordinates (spatial position). The three internal coordinates are the numbers of barium and sulphate ions (N_A and N_B) as well as the number of BaSO_4 molecules per particle in solid state N_P . All coordinates are discrete and therefore a very accurate mass conservation is guaranteed. These three coordinates can be used to model the process if the following assumptions are made:

- Monodisperse water volume of each droplet.
- At maximum one particle per droplet.
- No agglomeration and breakage of particles.

These assumptions are justified in the present case: the droplet size distribution of droplets without particles is almost monodisperse (Adityawarman et al., 2005); only less than 1% of the droplets contain one particle; the nanoparticles observed on microscope pictures (see Adityawarman et al.,

2005) are no agglomerates or fragments of bigger particles. The first assumption is used as well for droplets with particles, since it is assumed that the water content remains constant during the expansion of droplets resulting from particle growth.

A direct solution of the fully coupled six-dimensional problem is practically impossible with current computational possibilities and solution methods. The computational demand for the solution of the three-dimensional PBM for the ideally mixed case without external coordinates is already extremely high. Therefore, a careful model reduction of the population balance model has to be performed before the external coordinates can be taken into account.

4.4.1 Population balance and reaction kinetics

4.4.1.1 Model reduction concept

The model reduction concept is based on reasonable assumptions concerning the distributed properties of the system, which allow the representation of the three-dimensional reference droplet number distribution $f_{ref}(N_A, N_B, N_P, t)$ by coupled balances with a lower dimension.

The first reduction step is obtained by a separation approach. The distribution of the two dissolved reactants and the particle size distribution can be split into two separated distributions if the redistribution of the reactants in the two daughter droplets is independent of the existence and size of a particle inside these droplets. The resulting distributions are a two-dimensional probability density function P_{2D} and a one-dimensional number density function f . Consequently, the reference number distribution f_{ref} can be calculated from

$$f_{ref}(N_A, N_B, N_P, t) \approx P_{2D}(N_A, N_B, t) \cdot f(N_P, t). \quad (4.2)$$

The computational demand needed for the solution of this coupled system is still too high for an implementation within a CFD code solving complex, three-dimensional unsteady flows (Niemann and Sundmacher, 2006b and c, 2007) and a further reduction of the model has to be performed.

In a second reduction step a quasi-steady-state hypothesis is applied to the distribution of the dissolved reactants P_{2D} . By this procedure P_{2D} is replaced by an analytically solvable equilibrium distribution P_{2D}^{eq} and Eq. (4.2) is simplified to

$$f_{ref}(N_A, N_B, N_P, t) \approx P_{2D}^{eq}(N_A, N_B, t) \cdot f(N_P, t) \quad (4.3)$$

with $P_{2D}^{eq}(N_A, N_B, t) = f(\lambda_A(t), \lambda_B(t))$, where λ_A and λ_B are obtained from Eqs. (4.6) and (4.7).

The application of an equilibrium distribution leads to the neglect of a slow-down effect resulting from the droplet exchange dynamics. If all reactants inside one droplet are depleted by nucleation and growth, further growth of this particle is only possible when a subsequent droplet exchange event provides new reactants from another droplet. The time period between depletion of reactants and a droplet exchange event is neglected in this model. Therefore this slow-down effect has to be considered by effective rate constants in the nucleation and growth rate approaches. These constants are determined by a parameter optimization (Niemann and Sundmacher, 2006a) and they are slowed down by a factor of 10^{-3} to 10^{-7} compared to the corresponding rate constants obtained from bulk precipitation.

This second reduction step results in a significant decrease of the simulation times from hours to a few seconds depending on the processor speed and desired accuracy level (Niemann and Sundmacher, 2006a and b). Nevertheless, for the coupling with a CFD code the computational effort is still extremely high.

In the third and last reduction step the droplet number distribution f is replaced by two Dirac-delta functions. The first one represents all droplets without particle $N_0(t)$ and therefore it is located at $N_P = 0$. The second Dirac-delta function stands for all droplets with particle $N_M(t) - N_0(t)$ and it is

located at the mean particle size represented by the mean number of molecules within one particle \bar{N}_p . The approximation of f_{ref} is then given by

$$f_{ref}(N_A, N_B, N_P, t) \approx P_{2D}^{eq}(N_A, N_B, t) \cdot \begin{cases} N_0(t) \cdot \delta(N_P, t) & \text{if } N_P = 0 \\ (N_M(t) - N_0(t)) \cdot \delta(N_P - \bar{N}_p, t) & \text{if } N_P \geq N_{crit} \end{cases} \quad (4.4)$$

The total number of droplets without particle $N_0(t)$ and the total number of droplets $N_M(t)$ can be calculated by Eqs. (4.10) and (4.12) given in Section 4.4.1.3. Due to the loss of information concerning the PSD a small error has to be accepted in the solution of this model. The mean growth rate in Eq. (4.11) has to be calculated from the mass averaged mean particle size and not from a size average (see Eqs. (4.14) and (4.15)). The mass averaged particle size predicts in our case a higher mean particle size and therefore a higher growth rate. A significant effect on the final results of the presented simulations can be excluded due to the very narrow and mono-modal PSDs in this system which only lead to a small difference between the two mean values.

In conclusion the highest error in the presented model reduction concept is reduction step from Eq. (4.2) to Eq. (4.3). The neglect of the droplet exchange dynamics forces an alternative consideration of the droplet exchange by effective rate constants in the nucleation and growth rate approaches. Nevertheless, the qualitatively good fit obtained with this approach presented in Niemann and Sundmacher (2006a) justifies the applicability of this reduction step.

4.4.1.2 Determination of P_{2D}^{eq}

The distribution of reactants inside the microemulsion droplets has been investigated first by Atik and Thomas (1981). They found out that a dissolved salt is distributed according to a Poisson distribution. In a more recent study by Hatton et al. (1993) the interactions between the different dissolved ions were taken into account. They showed that the distribution of the reactants strongly depends on the redistribution during the droplet exchange. Two limiting cases of the distribution can be identified: i) the Poisson distribution for the case that repulsive and cooperative forces between the ions are almost the same and ii) bimodal distributions with a lot of empty droplets in the case of strong cooperative forces between the different ions. The presented model approach allows the implementation of any arbitrary probability density distribution. Studies according to different redistribution protocols which result in different reactant distributions can be found, e.g. in Jain and Mehra (2004), Natarajan et al. (1996) and Niemann and Sundmacher (2006b). In the present study the focus lies on the coupling of the population balance with a complex flow structure. Therefore, only the limiting case of equal repulsive and cooperative forces is being investigated.

For this limiting case P_{2D}^{eq} is calculated from two one-dimensional Poisson distributions P_A and P_B of both reactants by

$$P_{2D}^{eq}(i, j, t) = P_A(i, t) \cdot P_B(j, t) \text{ with } i, j = 0 \dots N_{l,max} . \quad (4.5)$$

The two one-dimensional Poisson distributions are calculated by

$$P_A(i, t) = \lambda_A(t)^i \cdot e^{-\lambda_A(t)} / i! \quad \text{with} \quad \lambda_A(t) = \frac{N_A^{total}(t)}{N_M(t)} \quad (4.6)$$

and

$$P_B(j, t) = \lambda_B(t)^j \cdot e^{-\lambda_B(t)} / j! \quad \text{with} \quad \lambda_B(t) = \frac{N_B^{total}(t)}{N_M(t)} . \quad (4.7)$$

Thus, only λ_A and λ_B have to be known for the determination of P_{2D}^{eq} . Both represent the mean occupancies of a droplet with barium and sulphate ions, which are defined by the ratios of the total number of A or B ions and the total number of droplets in the reactor. The total numbers of A and B ions are given by

$$N_A^{total}(t) = (N_M(t) - N_{M,0}) \cdot \lambda_{A,0,feed} - N_s(t) \quad (4.8)$$

$$N_B^{total}(t) = N_{M,0} \cdot \lambda_{B,0} - N_s(t) \quad (4.9)$$

and the total number of droplets $N_M(t)$ is calculated by Eq. (4.12). $N_{M,0}$ is the initial number of droplets, $\lambda_{A,0,feed}$ the initial mean droplet occupancy with A ions in the feed, $\lambda_{B,0}$ the initial droplet occupancy with B ions inside the reactor and $N_s(t)$ is the total number of BaSO_4 molecules in solid state calculated by Eq. (4.11).

4.4.1.3 Balance equations

To calculate the two Dirac-delta functions (Eq. (4.4)) in order to close the reduced population balance model the balance equations for $N_0(t)$, $N_s(t)$ and $N_M(t)$ have to be solved and the time evolution of \bar{N}_p has to be derived from these equations:

$$\frac{dN_0(t)}{dt} = - \sum_{i=N_{crit}}^{N_{l,max}} \sum_{j=N_{crit}}^{N_{l,max}} P_{2D}^{eq}(i,j,t) \cdot r_{nuc}(i,j) \cdot V_W(t) + N_{feed}(t), \quad (4.10)$$

$$\begin{aligned} \frac{dN_s(t)}{dt} = & \sum_{i=N_{crit}}^{N_{l,max}} \sum_{j=N_{crit}}^{N_{l,max}} M_M(i,j) \cdot P_{2D}^{eq}(i,j,t) \cdot r_{nuc}(i,j) \cdot V_W(t) \\ & + \sum_{i=1}^{N_{l,max}} \sum_{j=1}^{N_{l,max}} P_{2D}^{eq}(i,j,t) \cdot r_{gro}(i,j) \cdot \Psi_T(t) \cdot (N_M(t) - N_0(t)) \end{aligned} \quad (4.11)$$

and

$$\frac{dN_M(t)}{dt} = N_{feed}(t), \quad (4.12)$$

where N_{crit} is the critical number of molecules needed to form a stable nucleus (defined by the modified Gibbs-Thomson relation, see Eq. (4.19)), $N_{l,max}$ the maximum number of dissolved ions of one kind inside a droplet, r_{nuc} the nucleation rate, V_W the water volume, N_{feed} the feed rate of droplets, r_{gro} the growth rate and $\Psi_T(t)$ is a transformation factor for the growth rate (see Eq. (4.14)). The matrix M_M correlates the ion combination i,j with the number of ions involved in the phase transition to solid state (example: five barium ions and seven sulphate ions can only form a BaSO_4 particle consisting of five molecules $\rightarrow M_M(5,7) = 5 = \min(5,7)$).

The mean number of BaSO_4 molecules within one particle needed for the localization of the second Dirac-delta function in Eq. (4.4) can be determined from all three balances by

$$\bar{N}_p(t) = \frac{N_s(t)}{N_M(t) - N_0(t)}. \quad (4.13)$$

The factor $\Psi_T(t)$ in Eq. (4.11) transforms the generally used unit for growth rates (m/s) in the unit used in the discrete balances of our model framework ((number of molecules)/s). It is defined as the first derivative of the mean number of molecules within one particle \bar{N}_p with respect to the mean particle diameter:

$$\Psi_T(t) = \frac{d\bar{N}_P(\bar{d}_P(t))}{d\bar{d}_P(t)} = \frac{d}{d\bar{d}_P(t)} \left(\frac{k_V \cdot \rho_P \cdot N_{Avogadro}}{M_P} \cdot \bar{d}_P^3(t) \right) = 3 \cdot \frac{k_V \cdot \rho_P \cdot N_{Avogadro}}{M_P} \cdot \bar{d}_P^2(t) \quad (4.14)$$

with

$$\bar{d}_P^3 = \frac{M_P}{k_V \cdot \rho_P \cdot N_{Avogadro}} \cdot \bar{N}_P, \quad (4.15)$$

where M_P is the molar mass of BaSO_4 , k_V the volume shape factor, ρ_P the particle density and $N_{Avogadro}$ Avogadro's number.

4.4.1.4 Precipitation kinetics

Nucleation and growth rates strongly depend on the supersaturation S within each droplet. For the microemulsion system with discrete coordinates individual supersaturation ratios for each droplet class depending on the ion combination are present. Thus nucleation and growth rates have as well individual values for each droplet class. The supersaturation for each droplet class is given by

$$S(N_A, N_B) = \sqrt{\frac{c_A(N_A) \cdot c_B(N_B)}{k_L}} = \sqrt{\frac{N_A \cdot N_B}{k_L \cdot N_{Avogadro}^2 \cdot V_D^2}} \quad (4.16)$$

with V_D = droplet volume and k_L = solubility product.

Special kinetic approaches for precipitation inside microemulsion droplets can not be found in the literature. In this study modified approaches from bulk precipitation were used to describe the particle formation dynamics. The nucleation rate is related to the standard approach by Bałdyga et al. (1995) with $\alpha_{nuc} = 15$ for high supersaturation. It is given by

$$r_{nuc}(N_A, N_B) = k_{nuc}^{eff} \cdot (S(N_A, N_B) - 1)^{\alpha_{nuc}}. \quad (4.17)$$

The implemented growth rate

$$r_{gro}(N_A, N_B) = k_{gro}^{eff} \cdot (S(N_A, N_B) - 1)^{\alpha_{gro}} \quad (4.18)$$

is a modified standard bulk phase approach by Nielsen (1984) with $\alpha_{gro} = 2$. The effective nucleation and growth rate constants k_{nuc}^{eff} and k_{gro}^{eff} are estimated by a least square optimization algorithm. The particle size distributions obtained with the model represented by Eq. (4.3) and the experimentally obtained particle size distributions are fitted simultaneously for 11 different experiments (details about the parameter estimation can be found in Niemann and Sundmacher, 2006a and b).

Another important parameter for the nucleation kinetics is the critical number of molecules needed to form a stable nucleus N_{crit} . The Gibbs-Thomson relation

$$N_{crit}(N_A, N_B) = \frac{32 \cdot \pi \cdot M_P^2}{\rho_P^2 \cdot N_{Avogadro}^2} \cdot \frac{\sigma_{eff}^3}{3} \cdot (k_B \cdot T \cdot \ln(S(N_A, N_B)))^{-3} \quad (4.19)$$

is used to calculate N_{crit} . This value depends on the supersaturation as well and is therefore also droplet-class specific. In Eq. (4.19) σ_{eff} is the effective interfacial surface tension, k_B the Boltzmann constant and T is the temperature. Niemann and Sundmacher (2006a) showed that σ_{eff} is approximately 0.13 J/m^2 in the investigated system. Consequently, the resulting N_{crit} values are between 8 and 9 according to the droplet class.

Table 4.3 contains all parameters used in the simulations.

Table 4.3. Model parameters

| Parameter | Value |
|---|---------|
| Maximum number of dissolved ions per droplet, $N_{l,\max}$ | 30 |
| Droplet feed rate, N_{feed} ($\times 10^{17} \text{ s}^{-1}$) | 2.4 |
| Initial number of droplets inside the reactor, $N_{M,0}$ ($\times 10^{19}$) | 6.3 |
| Molar mass of barium sulphate, M_p (g/mol) | 233.39 |
| Density of barium sulphate, ρ_p (g/cm ³) | 4.48 |
| Volume shape factor, k_V | $\pi/6$ |
| Solubility product, k_L ($\times 10^{-10} \text{ mol}^2/\text{L}^2$) | 1.3 |
| Effective nucleation rate constant, k_{nuc}^{eff} ($\times 10^{41} \text{ (m}^3 \text{ s)}^{-1}$) | 5.2 |
| Effective growth rate constant, k_{gro}^{eff} (nm/s) | 145.1 |

4.4.2 Numerical computations

The simplified PBM explained above has been first applied for the homogeneous reaction process (zero-dimensional analysis) before performing the inhomogeneous computations (three-dimensional analysis in space).

4.4.2.1 Zero-dimensional analysis

The homogeneous case calculations as a function of only time have been performed by MATLAB[®] 7.0. The computation at this stage takes less than a second when employing a single Pentium-IV Linux PC (2.7 GHz/2 GB memory). The results obtained from these time-dependent calculations are discussed later when compared with those obtained by experiments and coupled CFD simulations.

4.4.2.2 Three-dimensional CFD simulations

The geometry and the unstructured grid of the reactor used in the experiments have been generated using MixSim[®] 2.0 and are shown in Fig. 4.2. There are about 80,000 volume elements in the whole domain. This grid resolution has been obtained following the best practice guidelines proposed by MixSim[®] and FLUENT[®] (Fluent Inc., 2003 and 2005). Although the operation is in semi-batch mode (which means increasing fluid volume) until the end of feeding, the influence of the volume change on the flow field has not been modelled in order to simplify the computations. Instead, the total volume of the two microemulsions has been taken into account assuming a batch system during the whole simulation. Otherwise, applying a deforming dynamic mesh model for the changing liquid level would increase drastically the complexity and the computing time of the calculations. This is due to the fact that the flow parameters should be extrapolated to the deformed and newly created volume elements, associated with the requirement to re-compute the full flow field after each time-step. Nevertheless, the injection process is fully taken into account in the simulation during the feed time of 257.14 s. The feeding point is identical with the experiments and can be seen in Fig. 4.7.

The three-dimensional, unsteady simulations have been performed with the industrial CFD code FLUENT[®] 6.2. Equations and source terms of the reaction kinetics and PBM have been defined via external user-defined scalars (UDS) and functions (UDF). A two-stage calculation has been implemented. First, the flow field has been simulated without the reaction process until the unsteady hydrodynamic conditions have reached a constant limit cycle for one impeller rotation. Afterwards, the reaction process has been simulated within FLUENT[®] by switching off the flow and the turbulence

models (i.e. using the frozen-flow conditions corresponding to the limit cycle), while activating chemical reactions. By this way, the computations can be considerably accelerated. The computing times are about 24 h for the first stage and 6 up to 32 h for the second stage (depending on the simulated process duration), employing the same standard PC mentioned previously. This two-stage calculation method has already been applied for other processes (for example for crystallization reactors; see Öncül et al., 2005a and b) and found to be accurate (good agreement with experimental data) and computationally very efficient (low computing time). As an alternative, performing directly the calculation in a fully coupled manner (i.e. simultaneously solving for flow, turbulence and chemical reactions in time) results in a drastically higher computational effort. For example, to compute 30 s in real time for the process, the simulation relying on frozen flow conditions (two-stage calculation) takes about 21 min, while the corresponding fully-coupled simulation (single-stage calculation) requires slightly less than 60 days. Both calculations lead to almost identical results in the present configuration (Öncül et al., 2006).

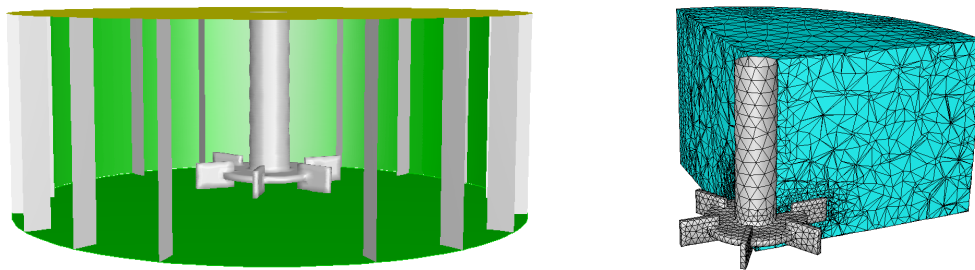


Fig. 4.2. Geometry (left) and computational grid of the reactor (right) (complete dimensions are given in Adityawarman et al., 2005; Niemann et al., 2006).

Two numerical approaches have been employed in order to simulate the motion of the impeller. The so-called multiple reference frames (MRF) model has initially been applied, yielding a first estimation of the flow for steady-state conditions. The obtained MRF-solution has been used as an initial guess for a further, unsteady simulation applying the more realistic sliding mesh model (SMM). Unlike the MRF model (Luo et al., 1994), the SMM is capable of taking into account the impeller-baffle coupling effects, since the time-dependent location of the impeller is taken into consideration (Luo et al., 1993; Ng et al., 1998; Montante et al., 2001b; Sommerfeld and Decker, 2004). Therefore the sliding mesh technique delivers more reliable results for an unsteady calculation. However, initializing the SMM-simulation using the MRF-results reduces the total computational time considerably (Paul, 2004), compared to a direct SMM-simulation. The computing times for the MRF- and SMM-simulations are roughly 3 h and 21 h, respectively, until the cyclic unsteady flow field (i.e. the right flow periodicity) has been obtained. For these flow field simulations a second order discretization has been used in space and a second order implicit time formulation has been chosen for the unsteady solution of the SMM (Fluent Inc., 2005). Iterations have been stopped when residuals fall below 10^{-4} for continuity and below 10^{-3} for the other parameters in each time-step.

The standard k - ϵ approach has been used as turbulence model since this model is known to supply a reasonable accuracy and short computing times for such baffled tanks in which no strong, swirling flow occurs (Montante and Bakker, 2004; Montante et al., 2001a).

4.5 Results and discussion

4.5.1 Validation of the reduced model

The reduced PBM has been validated using the available experimental results. Fig. 4.3 shows the comparison for particle size distributions obtained by numerical and experimental results for the different conditions (see Table 4.1). Here it is worth keeping in mind that the reduced model yields

only the mean particle size instead of a complete distribution function. As can be seen from these comparisons an acceptable agreement has been achieved with the reduced model, although larger deviations are observed for cases with a high concentration excess of one of the microemulsions. This validation procedure, carried out for spatially homogeneous conditions (zero-dimensional computation in physical space) forms the basis of the further three-dimensional, inhomogeneous CFD computations.

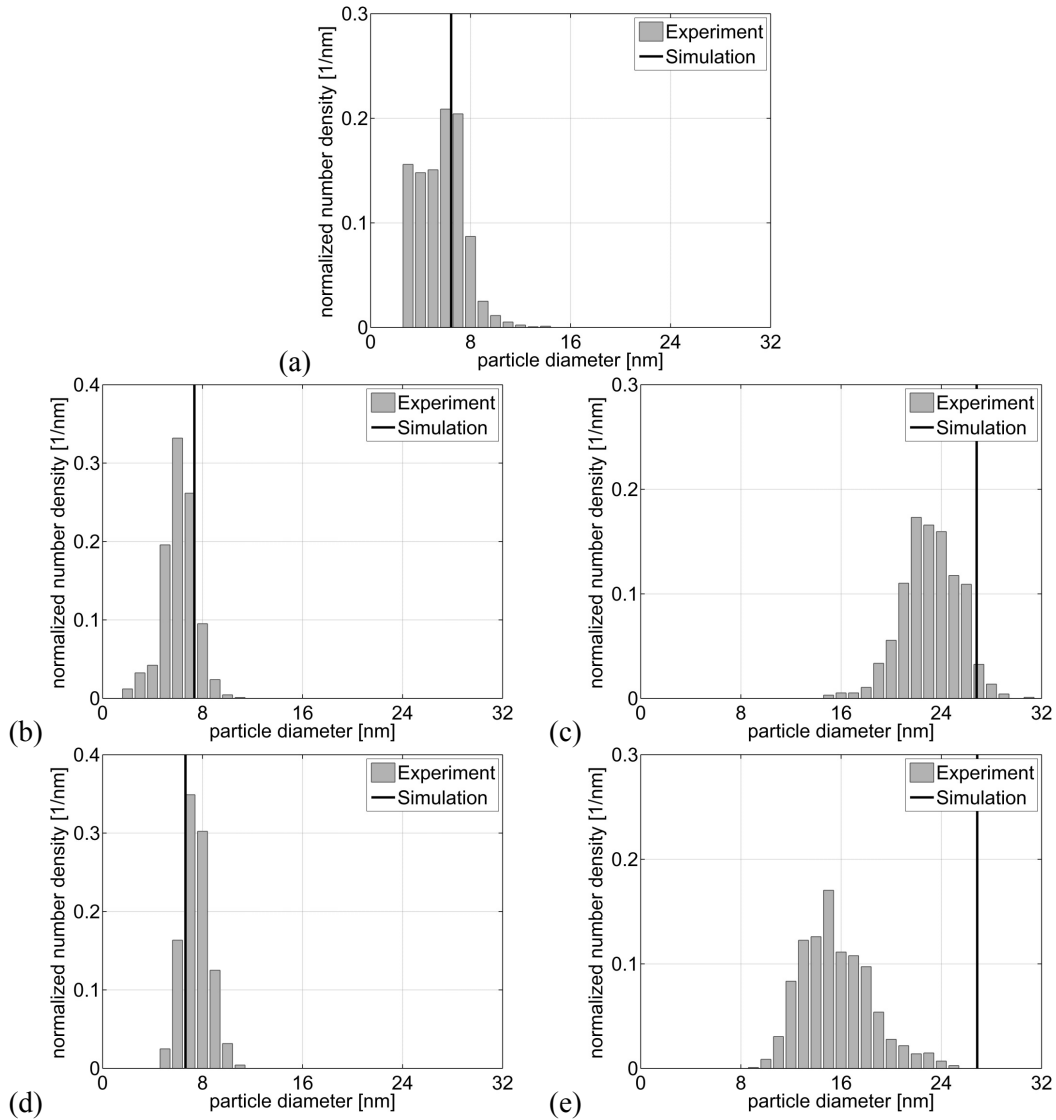


Fig. 4.3. Validation of the reduced model with experimental data for Cases A (a), B1 (b), B2 (c), C1 (d) and C2 (e).

4.5.2 Results of CFD simulations

Time-periodic flow conditions have been achieved after roughly 100 full rotations of the impeller (corresponding to 20 s physical time) during the unsteady flow field simulation employing SMM.

The evolution of the mean number of dissolved Ba^{2+} and SO_4^{2-} ions per droplet (λ_{Ba} , i.e. λ_A and λ_{SO_4} , i.e. λ_B , respectively) and the mean particle diameter (\bar{d}_p) with respect to time according to the three-dimensional (3D) second-stage simulations (including only the inhomogeneous precipitation on top of the frozen flow) are represented in Figs. 4.4–4.6 in comparison with the results of the zero-

dimensional (0D) analysis in space. Here it is worth stating that each 3D result is an overall mass-averaged value in the whole reactor. Referring to these comparisons, it can be concluded that an almost homogeneous reaction process is observed in the reactor except for Case A, where a noticeable discrepancy is observed compared to the 0D results (relative reduction of the mean, final particle size by 14.1%). This is actually not unexpected since Case A leads to the highest supersaturation ratio in this work. Higher supersaturation ratio leads to a faster reaction, which means greater sensitivity of the process to local hydrodynamic conditions. In other words, the mixing mechanism becomes more important for the precipitation process, since the reaction time-scale decreases with increasing supersaturation ratio while the mixing time-scale remains unchanged. This situation can be better understood when reaction and macromixing (i.e. reactor-scale mixing) time-scales are compared. The reaction time-scale, τ_R , for Case A is about 400 s whereas it is around 2,000 s for Cases B2 and C2 (see again Figs. 4.4–4.6). On the other hand, the mixing time-scale, τ_M , is the same for all cases and can be calculated by the following formula for Rushton turbine impellers Bałdyga et al. (1995):

$$\tau_M = \frac{V_{reactor}}{Q_c} \quad (4.20)$$

with

$$Q_c = 1.5 N_{rps} d_{imp}^3, \quad (4.21)$$

where Q_c is the circulation capacity, N_{rps} the stirring rate and d_{imp} the impeller diameter, here equal to 3 cm. According to Eqs. (4.20) and (4.21), the value of τ_M varies between 0.74 and 1.48 s since the reactor volume, $V_{reactor}$, continuously increases until the end of feeding. As a consequence, $\tau_R \gg \tau_M$ in all cases (well-mixed conditions), but the case with the lowest τ_R value (Case A) is roughly five times more sensitive to mixing conditions compared to Cases B2 and C2. Consequently, almost no deviation between the results of 0D and 3D simulations is observed in Cases B2 and C2 due to the corresponding, low supersaturation levels (the lowest in this study) and therefore long reaction time-scales. Finally, Cases B1 and C1 are associated with a visible but very low difference between 0D and 3D simulations.

In addition to these averaged profiles, various local profiles inside the reactor have also been investigated for a better understanding of the mixing conditions. This has been carried out by examining the profiles at six chosen locations, shown in Fig. 4.7. As can be seen from this sketch, the odd numbered points and the even numbered points are positioned symmetrically to each other with respect to the reactor axis. P3 represents the feed exit location whereas P1 and P5 are placed close to the impeller blades and to the fluid top level, respectively. The local λ_{Ba} , λ_{SO_4} , and \bar{d}_P profiles are examined at these locations for two extreme cases: Case A (for which the effect of hydrodynamic conditions are maximum because of the highest supersaturation ratio) and Case B2 (for which the mixing should have a minimum influence on the reaction due to the lowest supersaturation level). Corresponding time-dependent results are given in Figs. 4.8 and 4.9. According to these figures, higher local deviations from the reactor mean are observed in Case A, as expected. The largest local discrepancies in both cases belong obviously to the feeding exit point (P3), due to the continuously injected fresh reactant that causes a locally varying supersaturation profile. Moreover, the P5 profiles show also a non-negligible deviation in Case A, which is due to a flow recirculation vortex transporting the fed droplets of concentrated reactant from the feed point directly to this region within a short time. However, all local discrepancies disappear very rapidly after the feeding is completed ($t = 257.14$ s). This confirms that the mixing conditions induced by the impeller are strong enough to homogenize the emulsion system in a very short time. All locations other than P3 and P5 are always almost identical to the mean conditions within the reactor.

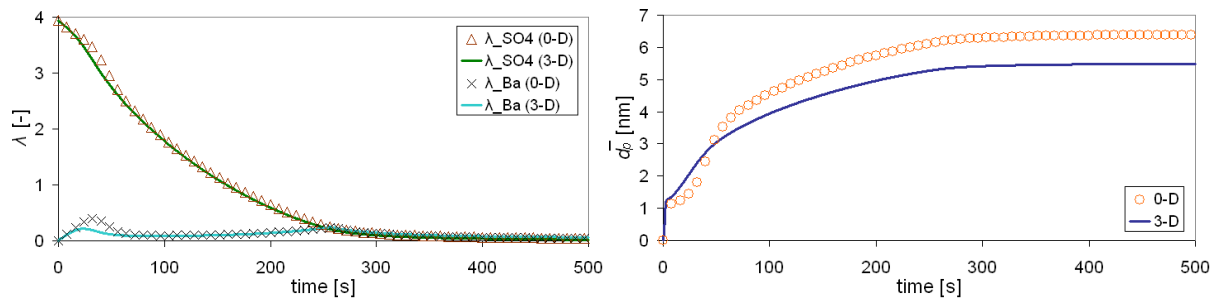


Fig. 4.4. 0D and 3D calculation results of Case A in comparison.

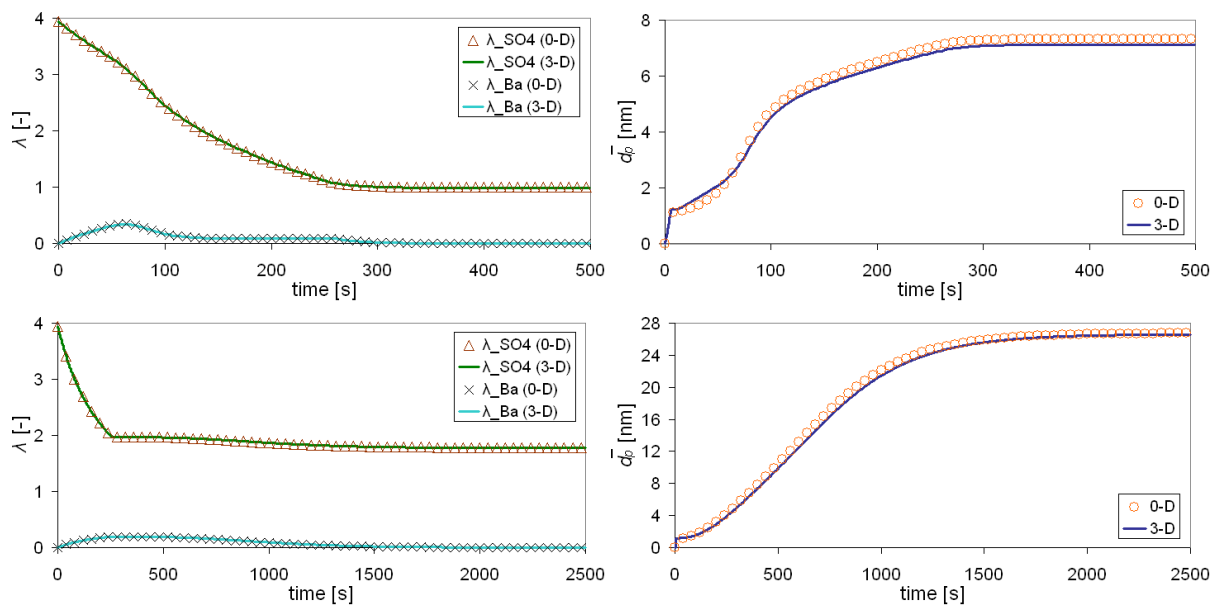


Fig. 4.5. 0D and 3D calculation results of Cases B1 (top) and B2 (bottom) in comparison.

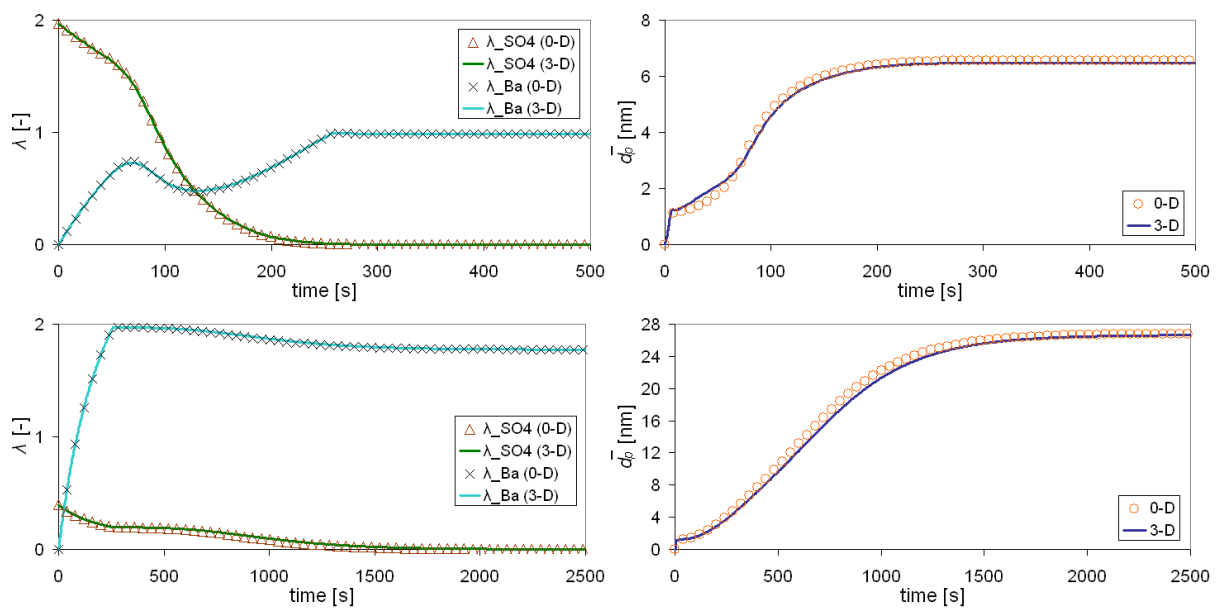


Fig. 4.6. 0D and 3D calculation results of Cases C1 (top) and C2 (bottom) in comparison.

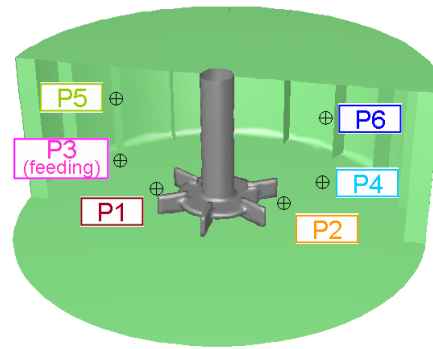


Fig. 4.7. Positions of the six points at which the local profiles are observed (note that the colours are identical with those used for the profiles).

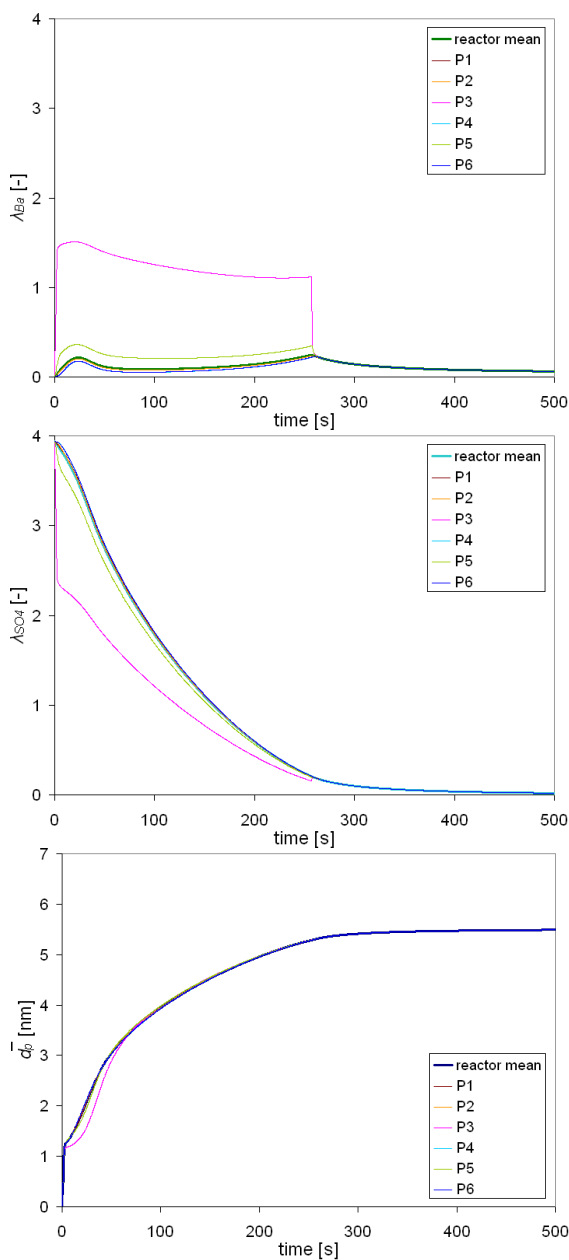


Fig. 4.8. Local profiles in comparison with reactor mean (thick line) for Case A. Feeding is completed at time $t = 257.14$ s.

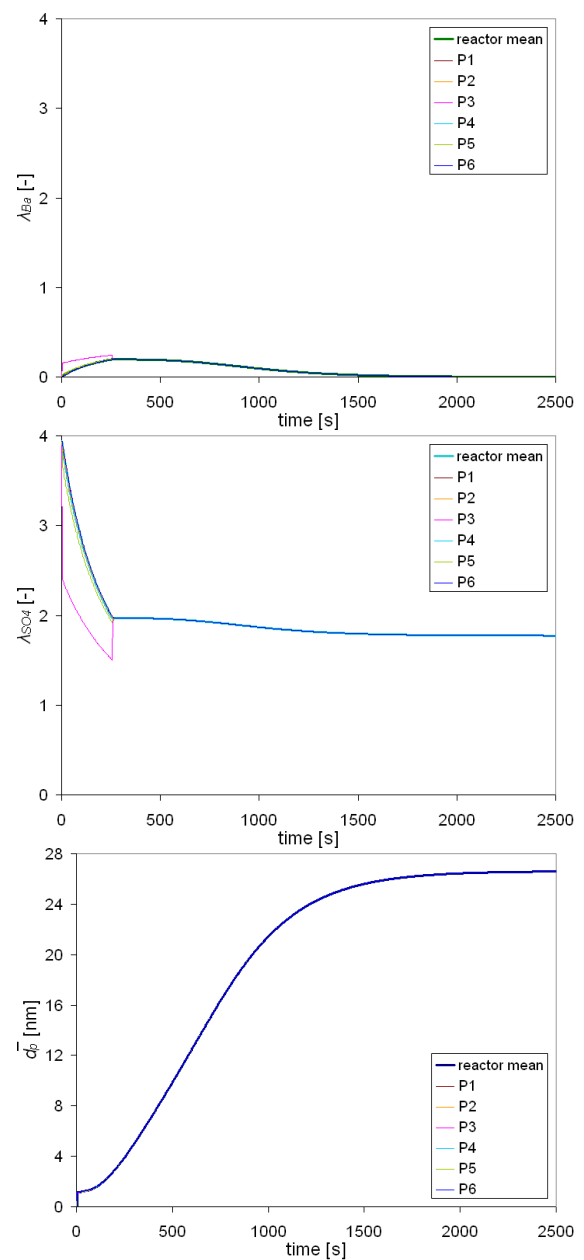


Fig. 4.9. Local profiles in comparison with reactor mean (thick line) for Case B2. Feeding is completed at time $t = 257.14$ s.

4.6 Conclusions and remarks

The aim of this work was to develop a simplified, zero-dimensional (homogeneous) PBM describing the precipitation of BaSO_4 in a microemulsion droplet population and to implement this model for the three-dimensional, real case analysis of the reaction process in a semi-batch reactor. The reduced PBM is based on a two-dimensional Poisson distribution for the dissolved Ba^{2+} and SO_4^{2-} ions and on a simplified representation of the droplet number distribution by two Dirac-delta functions.

Although the obtained results of zero-dimensional computations for stoichiometric cases have shown a good agreement with the experimental data, bigger deviations have been observed for cases with a high concentration excess of one of the microemulsions. Nevertheless, the reduced model has been validated up to an acceptable degree with the help of experimental data via this initial analysis.

In the second step, inhomogeneous simulations in space have been performed for a more realistic investigation by embedding the reduced PBM formulation within an industrial CFD code. The results of these three-dimensional CFD computations show an almost homogeneous reaction process within the reactor, which leads to the conclusion that the mixing quality is high. Noticeable discrepancies compared to zero-dimensional computations have been observed only in the stoichiometric case, for which the supersaturation ratio is highest. Furthermore, local deviations from the reactor mean can only be identified in the vicinity of the feeding location. This means that the deviations obtained with the simplified PBM model far from stoichiometry do not result from a coupling with hydrodynamics.

Nevertheless, the resulting coupled CFD/PBM simulation tool is extremely useful. Acceptable computing times have been obtained by using the flow field results based on a MRF approach as an initial guess for the more accurate calculations employing SMM. Furthermore, the reaction is solved as a final step on top of the frozen, cyclic flow condition. In this respect, the numerical experience gained during the previous study was very useful. By this way, it is possible to investigate the reaction process for any kind of three-dimensional inhomogeneous hydrodynamic conditions. This situation offers excellent opportunities for reactor optimization as a further step, by trying to use hydrodynamics in a controlled manner in order to improve process quality, for example to obtain smaller particles.

As a final conclusion, application of a reduced PBM in the CFD computations via in-house built UDS and UDF was successfully established during this study. This will be essential for the last chapter of this work, trying to reduce model complexity in order to describe cell cultivation.

References of Chapter 4

- Adityawarman, D., Voigt, A., Veit, P., Sundmacher, K. (2005). Precipitation of BaSO₄ nanoparticles in a non-ionic microemulsion: Identification of suitable control parameters. *Chem. Eng. Sci.*, 60, 3373-3381.
- Atik, S.S., Thomas, J.K. (1981). Transport of photoproducted ions in water in oil microemulsions - Movement of ions from one water pool to another. *J. Am. Chem. Soc.*, 103, 3543-3550.
- Baldyga, J., Podgórska, W., Pohorecki, R. (1995). Mixing precipitation model with application to double feed semibatch precipitation. *Chem. Eng. Sci.*, 50, 1281-1300.
- Fluent Inc., *Fluent 6.2 User's Guide*, Lebanon, USA, 2005.
- Fluent Inc., *MixSim 2.0 User's Guide*, Lebanon, USA, 2003.
- Hatton, T.A., Bommarius, A.S., Holzwarth, J.F. (1993). Population-dynamics of small systems. 1. Instantaneous and irreversible reactions in reversed micelles. *Langmuir*, 9, 1241-1253.
- Jain, R., Mehra, A. (2004). Monte Carlo models for nanoparticle formation in two microemulsion systems. *Langmuir*, 20, 6507-6513.
- Kiparissides, C. (2006). Challenges in particulate polymerization modeling and optimization: A population balance perspective. *J. Process Control*, 16, 205-224.
- Luo, J.Y., Gosman, A.D., Issa, R.I., Middleton, J.C., Fitzgerald, M.K. (1993). Full flow field computation of mixing in baffled stirred vessels. *Chem. Eng. Res. Des.*, 71A, 342-344.
- Luo, J.Y., Issa, R.I., Gosman, A.D. (1994). Prediction of impeller-induced flows in mixing vessels using multiple frames of reference. *ICHEME Symp. Ser.*, 136, 549-556.
- Luther, W. (2004). Industrial application of nanomaterials - chances and risks. *Technological analysis, Future Technologies Division of VDI Technologiezentrum GmbH*, Düsseldorf, Germany.
- Min, K.W., Ray, W.H. (1978). The computer simulation of batch emulsion polymerization reactors through a detailed mathematical model. *J. Appl. Polym. Sci.*, 22, 89-112.
- Montante, G., Bakker, A. (2004). *Stirring up the phases in tall tanks*, Fluent News, XIII(2), 8-9.
- Montante, G., Lee, K.C., Brucato, A., Yianneskis, M. (2001a). Experiments and predictions of the transition of the flow pattern with impeller clearance in stirred tanks. *Comput. Chem. Eng.*, 25, 729-735.
- Montante, G., Lee, K.C., Brucato, A., Yianneskis, M. (2001b). Numerical simulations of the dependency of flow pattern on impeller clearance in stirred vessels. *Chem. Eng. Sci.*, 56, 3751-3770.
- Natarajan, U., Handique, K., Mehra, A., Bellare, J.R., Khilar, K.C. (1996). Ultrafine metal particle formation in reverse micellar systems: Effects of intermicellar exchange on the formation of particles. *Langmuir*, 12, 2670-2678.
- Ng, K., Fentiman, N.J., Lee, K.C., Yianneskis, M. (1998). Assessment of sliding mesh CFD predictions and LDA measurements of the flow in a tank stirred by a Rushton impeller. *Chem. Eng. Res. Des.*, 76A, 737-747.
- Nielsen, A.E. (1984). Electrolyte crystal-growth mechanisms. *J. Cryst. Growth*, 67, 289-310.
- Niemann, B., Rauscher, F., Adityawarman, D., Voigt, A., Sundmacher, K. (2006). Microemulsion-assisted precipitation of particles: Experimental and model-based process analysis. *Chem. Eng. Proc.*, 45, 917-935.
- Niemann, B., Sundmacher, K. A discrete-continuous population balance approach for the nanoparticle precipitation in microemulsions, in: *World Congress on Particle Technology 5*, Orlando, USA, 2006a.
- Niemann, B., Sundmacher, K. Emulsionsgestützte Synthese von Nanopartikeln: Experimentelle und modelltheoretische Prozessanalyse, in: *DECHEMA/GVC Jahrestagungen*, Wiesbaden, Germany, 2006b.
- Niemann, B., Sundmacher, K. Manipulation and control of the particle size distribution of nanoparticles during their formation in microemulsion droplets by a suitable feed strategy, in: *Proceedings of AIChE Annual Meeting*, San Francisco, USA, 2006c, ISBN 0-8169-1012-X, Paper No: 87e.

- Niemann, B., Sundmacher, K. Nanoparticle precipitation in microemulsion: A discrete-continuous population balance approach, in: *Proceedings of PARTEC 2007*, Nuremberg, Germany, 2007.
- Öncül, A.A., Niemann, B., Thévenin, D., Sundmacher, K. CFD model of a semi-batch reactor for the precipitation of nanoparticles in the droplets of a microemulsion, in: *Proceedings of 16th European Symposium on Computer Aided Process Eng. (ESCAPE16) & 9th International Symposium on Process Systems Eng. (PSE2006)*, Garmisch-Partenkirchen, Germany, 2006, ISBN 978-0-444-52257-3, pp. 203-208.
- Öncül, A.A., Thévenin, D., Elsner, M.P., Seidel-Morgenstern, A. Numerical analysis of the preferential crystallization of enantiomers, in: *Proceedings of 11th Workshop on Two-phase Flow Predictions*, Halle, Germany, 2005a, ISBN 3-86010-767-4, pp. 5.10/1-5.10/15.
- Öncül, A.A., Thévenin, D., Elsner, M.P., Seidel-Morgenstern, A. Numerical analysis of the preferential crystallization of enantiomers in complex flows, in: *Proceedings of 12th International Workshop on Industrial Crystallization (BIWIC12)*, Halle, Germany, 2005b, ISBN 3-86010-797-6, pp. 165-172.
- Paul, E.L., Atiemo-Obeng, V.A., Kresta, S.M. (2004). *Handbook of Industrial Mixing: Science and Practice*, Wiley-Interscience, Hoboken NJ, USA.
- Singh, R., Kumar, S. (2006). Effect of mixing on nanoparticle formation in micellar route. *Chem. Eng. Sci.*, 61, 192-204.
- Sommerfeld, M., Decker, S. (2004). State of the art and future trends in CFD simulation of stirred vessel hydrodynamics. *Chem. Eng. Technol.*, 27, 215-224.
- Unzueta, E., Forcada, J. (1997). Modeling the effect of mixed emulsifier systems in emulsion copolymerization. *J. Appl. Polym. Sci.*, 66, 445-458.
- Vale, H.M., McKenna, T.F. (2005). Modeling particle size distribution in emulsion polymerization reactors. *Prog. Polym. Sci.*, 30, 1019-1048.

Part II: Application to cell cultivation in bioreactors

Chapter 5

Experimental characterization of flow conditions in bioreactors

5.1 Introduction

From now on, only cell cultivation in bioreactors is considered. Quantifying the influence of flow conditions on cell viability is essential for a successful control of cell growth and cell damage in major biotechnological applications, such as in recombinant protein and antibody production or vaccine manufacturing. In the last decade, new bioreactor types have been developed. In particular, bioreactors with wave-induced motion (commercial name: Wave Bioreactors[®]) show interesting properties (e.g., disposable cellbags suitable for cGMP manufacturing, no requirement for cleaning and sterilization of cultivation vessels, and fast setup of new production lines) and are considered in the present study. As an additional advantage, it is expected that cultivations in such bioreactors result in lower shear stress compared with conventional stirred tanks, due to the gentle liquid motion in the rocking cellbag. As a consequence, cell damage would be reduced as cell viability is highly sensitive to hydrodynamic conditions.

The aim of this chapter was to characterize experimentally the flow conditions in two cellbag sizes (2 L and 20 L) of Wave Bioreactors[®]. For this purpose, an experimental setup was developed during this study to measure the most important flow parameters (liquid surface level, liquid velocity, liquid and wall shear stress). By this way, CFD simulations describing the flow conditions within both cellbags during the further studies could be validated through the obtained experimental findings. Moreover, the measurements confirmed in particular low shear stress values in both cellbags, indicating favorable hydrodynamic conditions for cell cultivation.

Related publication

This chapter builds on top of:

Experimental characterization of flow conditions in 2 L and 20 L bioreactors with wave-induced motion

Andreas Kalmbach^{a,b}, Róbert Bordás^c, Alper A. Öncül^c, Dominique Thévenin^{c,*},
Yvonne Genzel^b, Udo Reichl^b

Biotechnology Progress (2010) in press (DOI 10.1002/btpr.516)

^a*Professur für Strömungsmechanik, Helmut-Schmidt-Universität Hamburg, Holstenhofweg 85, D-22043 Hamburg, Germany*

^b*Max-Planck-Institut für Dynamik komplexer technischer Systeme, Sandtorstr. 1, D-39106 Magdeburg, Germany*

^c*Institut für Strömungstechnik und Thermodynamik, Lehrstuhl für Strömungsmechanik und Strömungstechnik, Otto-von-Guericke-Universität Magdeburg, Universitätsplatz 2, D-39106 Magdeburg, Germany*

5.2 State of the art

The outbreak of the so-called “swine flu” H1N1 pandemic that originated in Mexico in March 2009 has spread to 39 countries in one month infecting 8480 persons globally (Mahony et al., 2009). This shows that beside diagnostic assays, an effective and fast production of vaccines is required to prevent major pandemic threats. Vaccines derived from cell cultures are typically obtained in T-flasks, roller bottles or stirred tanks. T-flasks and roller bottles provide excellent conditions for cell cultivation but have disadvantages in handling and preparation. Furthermore, it is difficult and expensive to produce large amounts of vaccines in such cultivation systems within a very short time. In contrast to this, modern stirred tank reactors can handle much higher working volumes and allow production of considerable amounts of vaccines in a single reactor. Beyond the complex validation of such bioreactors for production processes, disadvantages associated with stirred tank reactors are mainly the higher shear stress levels acting on the cells, time- and energy-consuming sterilization procedures, and extensive cleaning validation studies.

A possible alternative to these conventional cultivation systems is a bioreactor with wave-induced motion like the Wave Bioreactor[®] (Singh, 1999, Fig. 5.1). This system consists of a bag on a wave holder that periodically inclines and declines. This motion induces a flow in the liquid volume (e.g., cell suspension). The most obvious advantage of such bioreactors system is the disposability of the PET (polyethylene terephthalate) bags after a single use, which eliminates the required cleaning or repeated sterilization. This leads to low design complexity and a fast setup of new production lines. Presently, cellbags are available up to a working volume of 500 L.

Various examples can be found for the cultivation of animal cells using bioreactors with wave-induced motion, demonstrating the possibility of adapting classical processes that use either roller bottles or stirred tank bioreactors to the cellbag method (Hundt et al., 2007; Lohr et al., 2009; Okonkowski et al., 2007; Tang et al., 2007; Weber et al., 2002). For the cultivation of adherent Madin-Darby canine kidney (MDCK) cells in an influenza vaccine production process, it has been observed that higher maximum cell densities can be obtained in microcarrier culture in a cellbag (1 L

* Corresponding author. Tel.: +49-391-6718570; fax: +49-391-6712840.
E-mail address: thevenin@ovgu.de (D. Thévenin).

working volume) compared with a 5 L stirred tank bioreactor under similar conditions (Genzel et al., 2006). The difference of 350 cells per microcarrier (cellbag) compared with 250 cells per microcarrier (stirred tank) was especially assumed to be related to the unsteady flow field in the Wave Bioreactor[®] and to the expected lower shear stress.

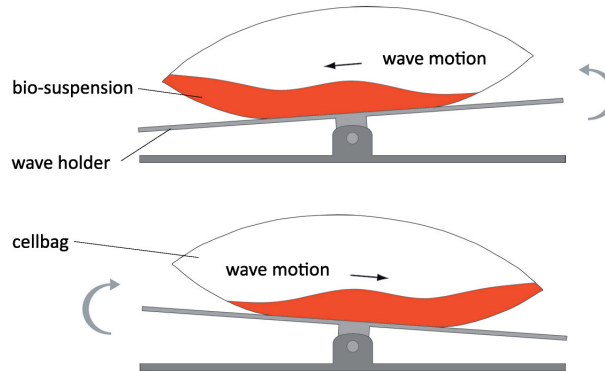


Fig. 5.1. Concept of bioreactors with wave-induced motion.

Flow characterization studies in conventional stirred reactors showed that the cell viability is mainly dependent on the acting shear stresses (Chisti, 2001). For animal cells, the lack of a protective cell wall and their considerable size compared with bacteria make them more susceptible to damage. Anchored animal cells, because of the lack of mobility, cannot reduce the net forces and are even more vulnerable (Croughan and Wang, 1991). Nevertheless, each cell type will show its individual sensitivity under each specific condition (reactor, flow, medium, etc., see Chisti, 2001). Critical shear stresses of different mammalian cell types were typically in the range of 0.7-1.4 Pa for adherent cell lines and of 0.3-1.7 Pa for suspension cell lines (Biedermann, 1994; Croughan and Wang, 1991). Therefore, shear stresses above their respective critical values could result in irreversible cell damage leading to cell death or insufficient cell growth (Koynov et al., 2007; Kretzmer, 2000). A comparison of critical cell shear stresses measured in different reactor types (Joshi et al., 1996; Stintzing et al., 2008) showed that flow conditions could become the main limiting factor for a cell cultivation process: stirred tank bioreactors show typical values of 0.01 to 25 Pa, roller bottles about 0.01 Pa, and bubble columns are associated with shear stress of 0.01 up to 30 Pa.

In the present work, the flow conditions in cellbags of two different sizes for typical operating conditions associated with mammalian cell culture have been characterized by measuring the four most relevant fluid parameters (liquid surface level, liquid velocity, bulk shear stress and wall shear stress). These time-dependent measurements were done under constant operating conditions (rocking rate, rocking angle, pressure, temperature). Experimental data have been furthermore used to validate the results of corresponding Computational Fluid Dynamics (CFD) simulations, as documented in the next chapter (Öncül et al., 2010).

5.3 Materials and methods

The experimental setup relied on a standard, commercial Wave Bioreactor[®] (Wave Biotech AG, Switzerland). Both 2 L and 20 L cellbags (Wave Biotech AG, Cellbags CB2L and CB20L, LDPE material, Switzerland) were placed in a standard manner on the rocking platform of the reactor. Operating conditions were set to a rocking rate of 15 rpm and a rocking angle of 7°, identical to the conditions for mammalian cell cultivation (Genzel et al., 2006).

In contrast to an ordinary cultivation, distilled water at a temperature of 37 °C was used as the flowing medium instead of a culture broth. This was necessary due to the measuring methods used. To access reproducibly different positions in both cellbags, a high-precision, three-dimensional traversing system (Fig. 5.2) was installed above the rocking platform of the reactor. This allowed a placement of

various sensor probes at target positions with accuracy better than 0.5 mm. The probes entered the bag through several airtight ports mounted on the upper surface of the PET bag. Due to the fact that a commercial cellbag had only a limited number of ports that also differ in size and shape, additional specific ports were prepared on the cellbags. These additional ports allowed access to multiple measuring positions (19 positions in the 2 L cellbag and 12 positions in the 20 L cellbag). Another requirement for the measurements was a constant overpressure of 10 mbar in the cellbag to assure a stable shape. Using a capsular spring manometer (Riegler & Co. KG, Gauge 6812, Germany), airtight conditions were controlled during the measurements.

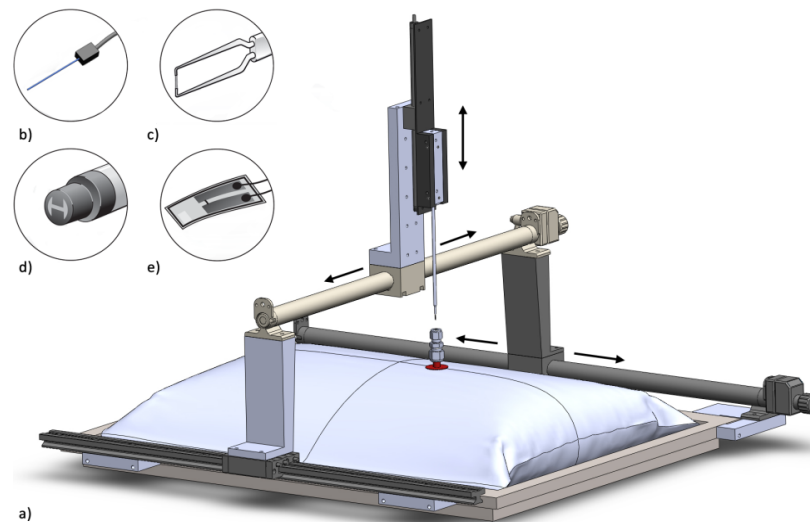


Fig. 5.2. a) Experimental setup (20 L cellbag, traversing, positioning system and probe holder) on the rocking holder of the Wave Bioreactor[®]; b) surface level probe; c) velocity probe; d) liquid shear stress probe; e) wall shear stress probe.

All probes (see later for details) delivered an analog signal at a relatively high frequency. In addition to the probe signal, a capacitive declination sensor (Seika Mikrosystemtechnik GmbH, Sensor N2, Germany) measured the real, instantaneous rocking angle of the reactor system. All signals were digitally recorded on a PC and later analyzed depending on their respective time phases (phase locking).

5.3.1 Probe description and calibration

The level of the liquid surface was measured with a capacitive probe specifically developed at the Chair of Fluid Dynamics of the University of Magdeburg. The probe detected the difference between the dielectric constants of the flowing medium and the air above it. Using a sensor calibration curve recorded in a container filled with distilled water up to a known level, the liquid surface heights could be measured.

The velocities of the main flow direction (directly induced by the rocking movement) were determined by using a commercial hot-film probe (Dantec Dynamics, Probe 55R11, Germany). This probe worked according to the constant temperature anemometry (CTA) principle: a thin, heated wire at a controlled temperature using a Wheatstone bridge. In a flow, a convective heat transfer from the wire to the fluid causes an adjustment of the wire voltage that holds onto the defined temperature. The amount of heat transferred from the wire to the fluid is directly dependent on the fluid velocity. CTA sensors react very rapidly and are thus perfectly suitable to measure time-dependent velocities.

In addition, estimations of the shear stress in the bulk of the liquid were obtained by using another hot-film probe especially designed for this purpose (also from Dantec Dynamics, Probe 55R46, Germany). It is known that such measurements are associated with a relatively large experimental

uncertainty. They are nevertheless useful to at least roughly estimate the resulting shear stress. Additionally, measurements of wall shear stress were performed at the bottom of the bag using special flush-mounted film probes (Dantec Dynamics, Probe 55R47, Germany) glued on the inner wall surface of the cellbag. Note that shear stress measurements are still considered as highly difficult, in particular in unsteady flows (Naughton and Sheplak, 2002; Tropea et al., 2007).

All probes used to measure flow velocity and shear stress must be calibrated. This has been realized using a special setup developed at the Chair of Fluid Dynamics of the University of Magdeburg, which consisted of a straight pipe filled with water circulating at controlled flow conditions and temperature. The flow rate was measured and regulated in the expected velocity/shear stress range found in the bag. With the recorded voltage as a function of the known liquid velocity and of the associated shear stress given by fully developed flow conditions, calibration points were calculated. To facilitate later post-processing, the corresponding points were later transformed into a continuous polynomial approximation. To increase accuracy, several polynomial functions were combined, each associated with a specific range of velocity (respectively shear stress). Taking into account the remaining uncertainties in the system and repeating several times the calibration measurements, the relative experimental uncertainties obtained with the probes were finally estimated to be $\pm 5\%$ for liquid level, $\pm 13\%$ for liquid velocity, $\pm 25\%$ for liquid shear stress and $\pm 20\%$ for wall shear stress.

5.3.2 Measurement procedure

Indispensable for the described measurements were constant measuring conditions (e.g., constant fluid density, fluid temperature, and rigid fixations of the probes) and a precise calibration. To check the differences between the velocity magnitudes close to the fluid surface and near the bottom of the bags, measurements at three different heights (5, 12 and 22 mm above the wave holder) were done systematically.

All measurements were started 60 s after initiating the rocking movement, in order to obtain fully periodic flow conditions in the bags (confirmed by CFD, see Chapter 6). Ten periods were recorded and afterwards analyzed. Phase locking has been used to obtain average results from the 10 periods, considering only the values obtained at the same inclination. During the averaging procedure, the repeatability error could be directly calculated. It was found to be less than 1% for the liquid surface level, up to 5% for liquid velocity, up to 20% for liquid shear stress, and less than 8% for wall shear stress. These values were considered satisfactory for such a complex setup.

When verifying the measured rocking rate and angle a posteriori, slight differences were observed compared with the adjusted, standard settings of 15 rpm and 7° . The positioning system together with the probe holders and the probes amounted to almost 5 kg of supplementary equipment with a relatively high mass center. This resulted in significant change in both rocking rate and angle, in particular for the largest (and therefore heaviest) cellbag. Therefore, the 20 L cellbag was filled with only 7 L of water (instead of 10 L at standard conditions) to keep the weight on the rocking platform below the maximum acceptable total weight recommended by the manufacturer (13 kg). The resulting, measured rocking rate of 15.94 rpm and the rocking angle of 7.9° however showed some differences from the input operating parameters. Not restricted in maximum weight, the 2 L cellbag was filled with water at its standard volume (1 L). Although well below the manufacturer's recommendations, the rocking rate still altered from 15 rpm (input) to 15.9 rpm (measured), whereas the rocking angle did not show any difference from the set point (7°). Apart from this minor issue, the experimental setup worked in a very satisfactory manner.

5.4 Results and discussion

In the following, the measurement results will be discussed successively for liquid level, liquid velocity and shear stress. All measuring positions in the 2 L and 20 L cellbags are illustrated in Fig.

5.3. For velocity and liquid shear stress, measurements at 5, 12 and 22 mm above the wave holder were done. However, due to the bag shape not all of the defined measurement heights could be reached at all positions. Near the bag borders particularly, only a subset of these positions could be physically measured.

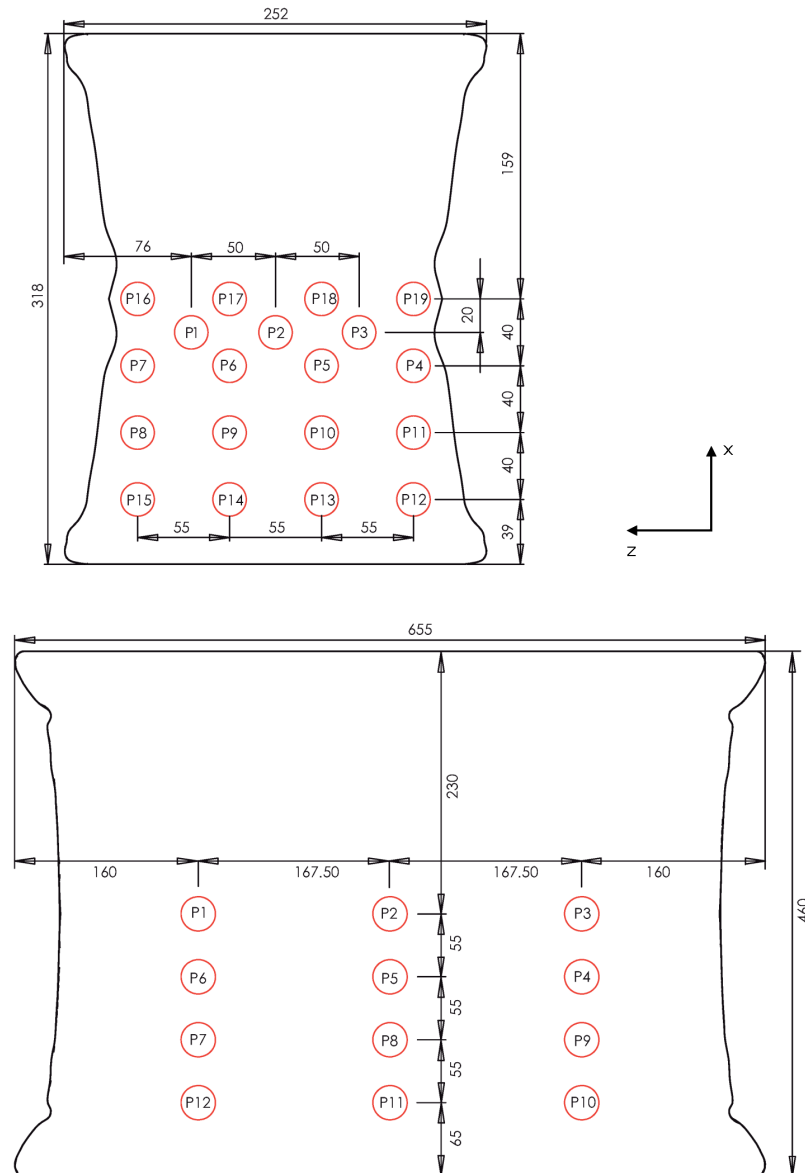


Fig. 5.3. Measuring positions in 2 L cellbag (top) and 20 L cellbag (bottom); all dimensions in mm.

5.4.1 Liquid level

For both cellbags (2 L and 20 L), the liquid levels were measured at the different positions shown in Fig. 5.3 and then linearly interpolated in between these positions (Fig. 5.4). The change in the surface level in the center of both bags was quite small as expected. In contrast to this, the surface levels at the sides of the bags showed a clear dependence on the reactor inclination. As a consequence of the inclination, there was no liquid at several measured locations for part of the time period (e.g., bottom part of Fig. 5.4 at -7.9°), confirming visual observations when reaching the highest reactor angle. Afterwards, the medium would flow back to the opposite side of the bag and surface levels would increase once again. Furthermore, especially in the 2 L bag, there were some slight differences

between the surface heights measured at symmetry points on the left and on the right side, probably due to the limited positioning accuracy of ± 0.5 mm.

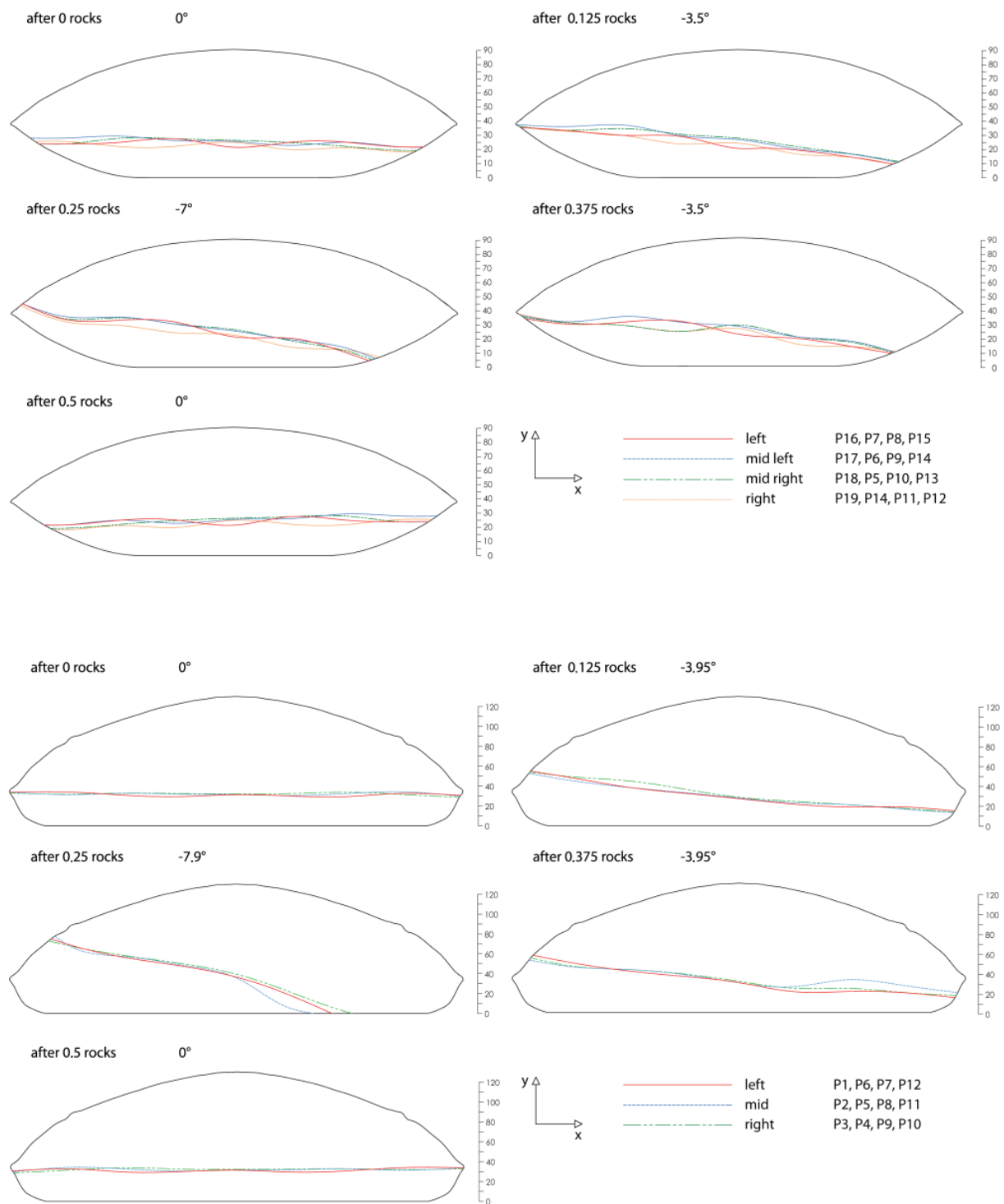


Fig. 5.4. Liquid surface heights (scales in mm) for a half period in 2 L (top) and 20 L (bottom) cellbags; colored lines represent different measurement layers and chronological order is from left to right, top to bottom.

5.4.2 Liquid velocity

Liquid velocity measurements were extensively used to validate CFD simulations as documented in the next chapter (Öncül et al., 2010). All velocities (u_x) presented here correspond to the velocity component in the main flow direction. In both bags, maximum velocities were reached every half period at the moment where the liquid moved from one side of the bag to the other (rocking angle $\sim 0^\circ$). As expected, considerably higher velocities were recorded in the larger, 20 L bag (maximum $u_x = 0.56$ m/s) compared with the 2 L cellbag (maximum $u_x = 0.16$ m/s). This can be readily explained by the lower filling level in the 20 L cellbag as well as by the larger magnitude of the displacement induced by the larger bag length (see Fig. 5.3).

Figs. 5.5 and 5.6 represent results of the velocity measurements at different heights and at all measurable positions in the 2 L and 20 L cellbag, respectively. The velocities (average and maximum) in both cellbags showed higher values in the center region than at the edges of the bag. This was particularly obvious in the 20 L cellbag. Interestingly, and in contrast to the common belief that velocities at the free surface would be higher than those near the bottom of a reactor, the measurements revealed locally higher velocities within the bulk of the liquid, especially for the 20 L cellbag. Although this situation could be surprising at first glance, it is found as well in the companion CFD simulations (see next chapter; Öncül et al., 2010) and is supported by literature concerning oscillating flows (see, e.g., Loudon and Tordesillas, 1998; Richardson and Tyler, 1929; and references within). It has been known for a long time that the peak velocities obtained for oscillating flows in tubes migrate from the center line (steady case) towards the wall with increasing oscillation rates. A similar observation is found here. The fact that this displacement was more obvious in the 20 L cellbag indicates that unsteady flow effects are more predominant in this configuration compared with the 2 L cellbag. As demonstrated in the next chapter (Öncül et al., 2010), the flow remains laminar in both cellbags.

Velocity fluctuations can have a significant influence on cells (Croughan and Wang, 1991). Therefore, the average relative absolute deviation (σ_{rel}) of the local liquid velocity variation was also determined, since it would indicate non-constant hydrodynamic loads on the cells. This parameter was computed according to

$$\sigma_{rel} = \frac{\frac{1}{n} \sum_{i=1}^n |u_{x,i} - \overline{u_x}|}{\overline{u_x}} \quad (5.1)$$

where $u_{x,i}$ represents the velocity data measured at various time instants and $\overline{u_x}$ denotes the velocity averaged in time. The variation of the liquid velocity in the 2 L cellbag was relatively small over the whole bag, whereas the velocities in the 20 L cellbag considerably fluctuated (Fig. 5.7). Consequently, it appears that mammalian cells would be exposed to a non-constant hydrodynamic load during a cultivation process in the 20 L cellbag under the chosen conditions.

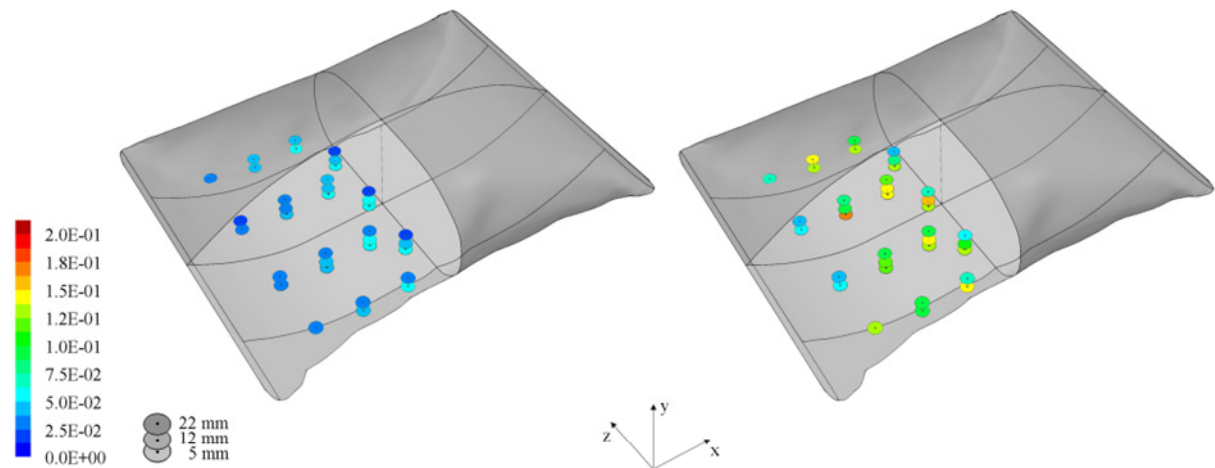


Fig. 5.5. Average (left) and maximum (right) velocities (m/s) at different heights measured in 2 L cellbag. Heights measured are shown as three circles piled (5, 12 and 22 mm from the bag bottom). Missing circles (starting from the lowest level, i.e., 5 mm) in some positions (especially near the bag edges) represent missing levels, which are due to the curved shape of the bag bottom.

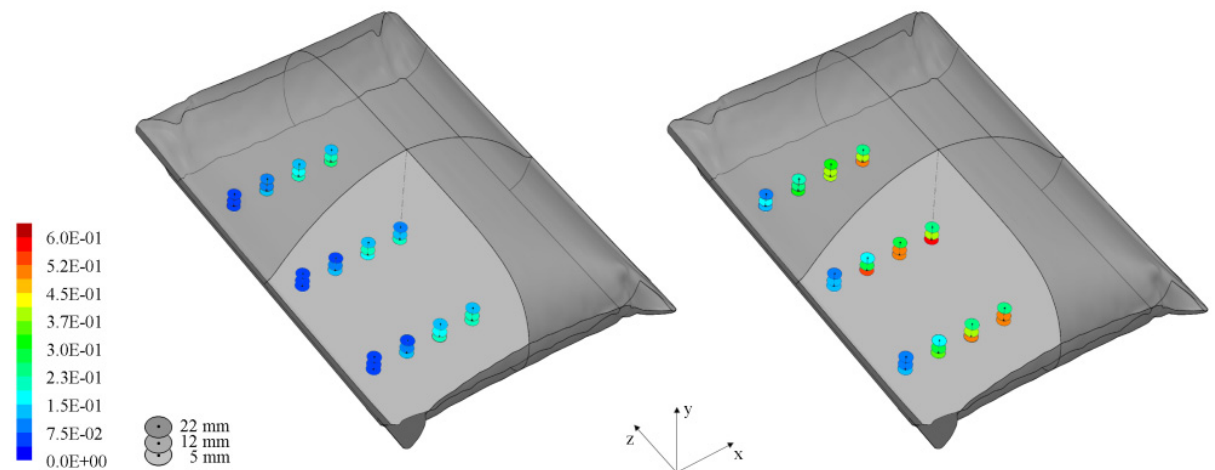


Fig. 5.6. Average (left) and maximum (right) velocities (m/s) at different heights measured in 20 L cellbag. Heights measured are shown as three circles piled (5, 12 and 22 mm from the bag bottom).

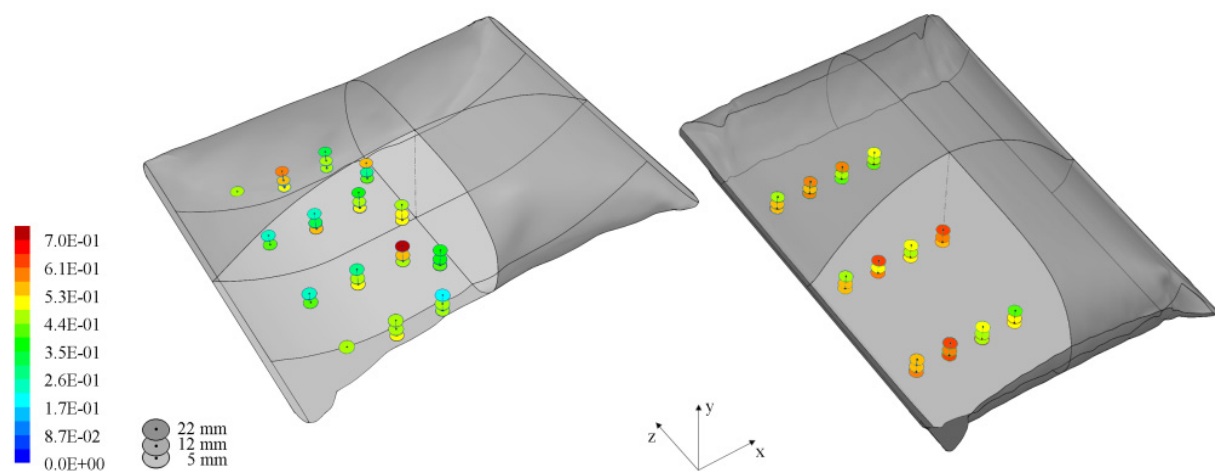


Fig. 5.7. Average relative absolute deviation of the liquid velocity in 2 L (left) and 20 L (right) cellbags. Heights measured are shown as three circles piled (5, 12 and 22 mm from the bag bottom). Missing circles (starting from the lowest level, i.e. 5 mm) in some positions (especially near the bag edges) represent missing levels, which are due to the curved shape of the bag bottom.

5.4.3 Liquid shear stress

Investigations regarding the liquid shear stress (τ_l) were performed for selected positions in the liquid. As already explained when describing the calibration procedure, measuring the shear stress is considerably more challenging than measuring liquid levels or velocities. As a consequence, the quality of the results is reduced, explaining in particular the larger variability of the peak values shown in Fig. 5.8 (right) and Fig. 5.9 (right). These random errors tend to cancel out, leading to much more reliable mean values (left part of Fig. 5.8 and Fig. 5.9).

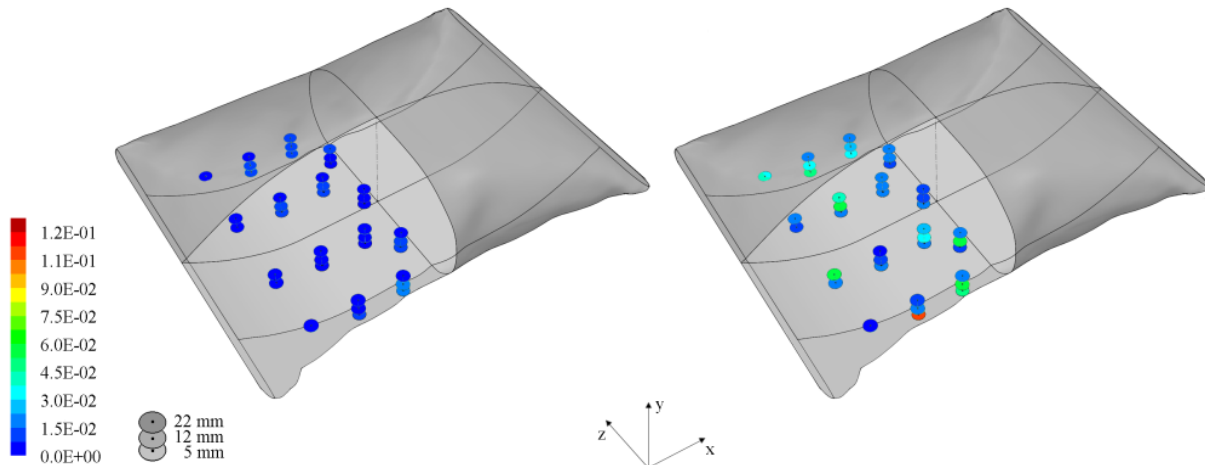


Fig. 5.8. Average (left) and maximum (right) liquid shear stresses (Pa) at different heights measured in 2 L cellbag. Heights measured are shown as three circles piled (5, 12 and 22 mm from the bag bottom). Missing circles (starting from the lowest level, i.e. 5 mm) in some positions (especially near the bag edges) represent missing levels, which are due to the curved shape of the bag bottom.

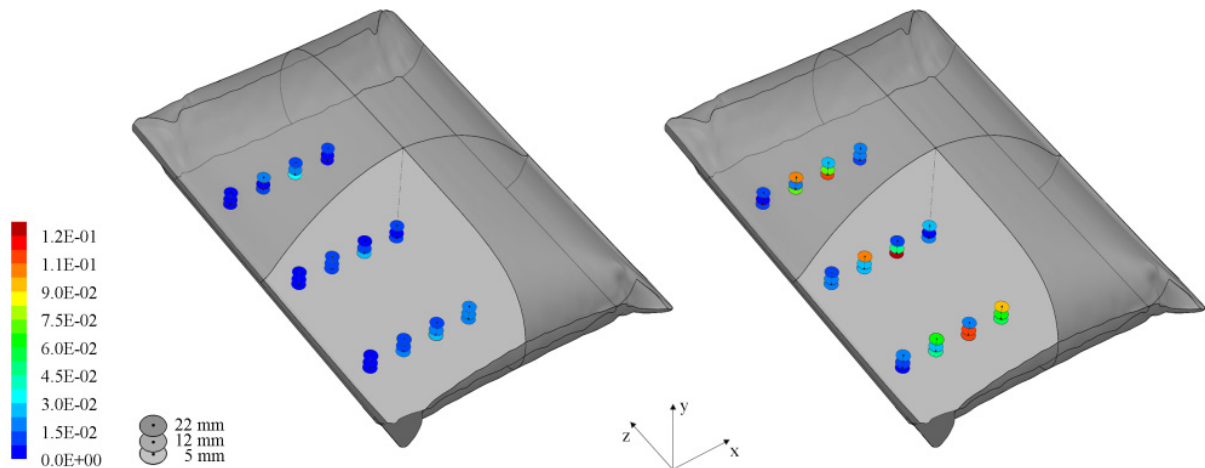


Fig. 5.9. Average (left) and maximum (right) liquid shear stresses (Pa) at different heights measured in 20 L cellbag. Heights measured are shown as three circles piled (5, 12 and 22 mm above the bag bottom).

Nevertheless, the most significant result of these measurements was the range of measured shear stresses. All measured instantaneous values in both cellbags were below 0.13 Pa. The average value of the shear stress remained always below 0.05 Pa. This is considerably lower than the levels found in conventional stirred bioreactors, in which mean values exceeding a few Pa can be observed at specific locations (Joshi et al., 1996). As a shear stress higher than 0.7 Pa (resp. 0.3 Pa) was considered critical

for growth of anchorage-dependent cell lines by Croughan and Wang (1991) (respectively of suspension cells, see Biedermann, 1994), the very low shear stress level found in the cellbags probably explains some of the observations reported in literature. In particular, it has been shown that cells that were usually difficult to grow at larger scales in other bioreactors gave acceptable results in cellbags (Palazón et al., 2003). Additionally, adherent MDCK cells grew to higher densities on microcarriers when cultivated in cellbags (Genzel et al., 2006). These promising results have led to further examples of cultivations in cellbags, such as NS0, hybridoma, avian suspension cells or insect cells, clearly showing the potential of these bioreactors (Lohr et al., 2009; Okonkowski et al., 2007; Tang et al., 2007; Weber et al., 2002).

5.4.4 Wall shear stress

Additional studies were carried out to determine the wall shear stress (τ_w) at the bottom of the bags. The method is very similar to that of the liquid shear stress measurement, differing only in the form and mounting of the probes (compare Fig. 5.2d and e). The calibration of the film probes was again carried out in the setup described in Section 5.3.1, where the temperature and velocity could be continuously controlled. During the calibration process, the conditions were equivalent to that of a Poiseuille-flow, thus the connection between flow velocity (voltage drop on the probe) and wall shear stress could be calculated using theoretical results for both laminar and turbulent flow regimes (Pope, 2000). Measurement results in the 20 L cellbag are exemplified in Fig. 5.10.

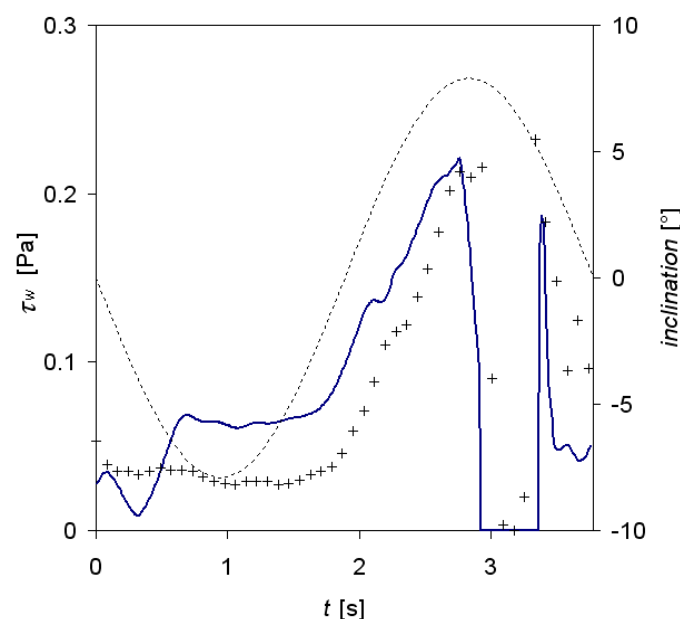


Fig. 5.10. Instantaneous values of wall shear stress (τ_w) for one rocking cycle according to the numerical results (solid line) and experimental data (symbols) at position P12 (see Fig. 5.3) in the 20 L cellbag. The corresponding time-dependent inclination of the cellbag is also shown with a dashed line.

The most important finding of these measurements was the range of the measured wall shear stresses, confirming previous observations for the liquid shear stress. The instantaneous values in both cellbags were always below 0.25 Pa. The average value of the shear stress at all measurement positions remained always below 0.08 Pa in both bags for the whole period. In Fig. 5.10, the measurement results are depicted at a given position (P12) in the 20 L bag and are compared with the results of a numerical simulation (see next chapter for further details). Measured and computed values are in close agreement and remain considerably below the critical values for shear stress found in the literature.

5.4.5 Further hydrodynamic quantities

For a full characterization of the flow conditions in Wave Bioreactors[®], the measurement of further properties would be obviously very interesting. Not all of them could be measured in this first experimental investigation. In particular, working with pure water without microcarriers and cells, mixing and mass transfer could not be characterized, highlighting the need for further studies. Two points might nevertheless be already mentioned here. First, a fast and very good homogenization of the microcarriers used in practical cases for adherent cell lines has been observed visually by coloring these microcarriers and operating the system as usual. Hence, the mixing quality appears to be qualitatively good. Second, oxygen transfer rates have been experimentally determined in 2 L Wave Bioreactors[®] in separate studies from our group (data not shown) showing very good aeration properties.

5.4.6. Scale-up considerations

Since only 2 L and 20 L cellbags have been considered up to now in this study, it is too early to give definitive conclusions on scale up in much larger reactors. However, comparing the results obtained with 2 L and 20 L might already give some information concerning the expected trends. Corresponding results are summarized in Table 5.1.

Table 5.1. Differences observed between 2 L cellbag and 20 L cellbag

| Quantity | 20 L cellbag compared to 2 L cellbag | Comment |
|-------------------------------------|---|---|
| Variation of liquid level with time | Slightly stronger | Remember that 20 L cellbag is only filled with 7 L water |
| Maximum flow velocity | Considerably higher (20 L: 0.56 m/s 2 L: 0.16 m/s) | Partly due to lower filling ratio in 20 L cellbag; Maximum velocity not at surface level |
| Flow state | Larger unsteady effects, but still laminar | Will switch to turbulent at some critical bag size |
| Velocity fluctuations | Considerably larger | |
| Peak liquid shear stress | Slightly higher (20 L: 0.13 Pa 2 L: 0.10 Pa) | Large measurement uncertainty |
| Wall shear stress | Peak: slightly higher (+10%) Mean: considerably higher (x 2.5) | Large measurement uncertainty |

5.5 Conclusions and remarks

In the present work, flow conditions in two different Wave Bioreactors[®] (2 L and 20 L cellbags) have been characterized using experimental measurements. Four flow parameters (liquid level, liquid velocity, liquid shear stress and wall shear stress) were measured at different positions in both cellbags under defined operating conditions typically used for mammalian cell cultivation. All measurements have been performed on line in a commercial, flexible cellbag operated normally. The obtained results were then used for the validation of the numerical investigations in the next studies.

It was shown that peak velocity values are not found near the free surface, but closer to the bag bottom with increasing influence of unsteady flow dynamics (i.e., for larger bag size). Velocity variations are also stronger in the 20 L bag, leading to varying hydrodynamic loading on the cells. The results of the shear stress measurements showed that in both cellbags very low levels are found compared with conventional stirred reactors. As a consequence of the comparatively low shear stress, mammalian cells growing on microcarriers in cellbags do not need to “flatten” as much and thus, more cells of the same volume can grow in a monolayer. From this point of view, the present work constitutes an excellent opportunity to improve our understanding of the impact of flow conditions on cell growth characteristics found in such reactors.

In the future, large-scale reactors would be characterized in the same manner. Today, working volumes of up to 500 L are available. At such scales, the rocking direction and strategy might become essential, and experimental characterization of flow properties in cellbags as well as computer simulations will help optimize cultivation strategies.

References of Chapter 5

- Biedermann, A. (1994). *Scherbeanspruchung in Bioreaktoren*, Ph.D. Dissertation, Universität Köln.
- Chisti, Y. (2001). Hydrodynamic damage to animal cells. *Crit. Rev. Biotechnol.*, 21, 67-110.
- Croughan, M.S., Wang, D.I. (1991). Hydrodynamic effects on animal cells in microcarrier bioreactors. *Biotechnology*, 17, 213-249.
- Genzel, Y., Olmer, R.M., Schäfer, B., Reichl, U. (2006). Wave microcarrier cultivation of MDCK cells for influenza virus production in serum containing and serum-free media. *Vaccine*, 24, 6074-6087.
- Hundt, B., Best, C., Schlawin, N., Kassner, H., Genzel, Y., Reichl, U. (2007). Establishment of a mink enteritis vaccine production process in stirred-tank reactor and Wave[®] Bioreactor microcarrier culture in 1-10 L scale. *Vaccine*, 25, 3987-3995.
- Joshi, J.B., Elias, C.B., Patole, M.S. (1996). Role of hydrodynamic shear in the cultivation of animal, plant and microbial cells. *Chem. Eng. J.*, 62, 121-141.
- Koynov, A., Tryggvason, G., Khinast, J.G. (2007). Characterization of the localized hydrodynamic shear forces and dissolved oxygen distribution in sparged bioreactors. *Biotechnol. Bioeng.*, 97, 317-331.
- Kretzmer, G. (2000). Influence of stress on adherent cells, in: Scheper, T. (Ed.), *Advances in Biochemical Engineering/Biotechnology*. Springer, Berlin/Heidelberg, 67, 123-137.
- Lohr, V., Rath, A., Genzel, Y., Jordan, I., Sandig, V., Reichl, U. (2009). New avian suspension cell lines provide production of influenza virus and MVA in serum-free media: studies on growth, metabolism and virus propagation. *Vaccine*, 27, 4975-4982.
- Loudon, C., Tordesillas, A. (1998). The use of the dimensionless Womersley number to characterize the unsteady nature of internal flow. *J. Theor. Biol.*, 191, 63-78.
- Mahony, J.B., Hatchette, T., Ojkic, D., Drews, S.J., Gubbay, J., Low, D.E., Petric, M., Tang, P., Chong, S., Luinstra, K., Petrich, A., Smieja, M. (2009). Multiplex PCR tests sentinel the appearance of pandemic influenza viruses including H1N1 swine influenza. *J. Clin. Virol.*, 45, 200-202.
- Naughton, J.W., Sheplak, M. (2002). Modern developments in shear-stress measurements. *Prog. Aerosp. Sci.*, 38, 515-570.
- Okonkowski, J., Balasubramanian, U., Seamans, C., Fries, S., Zhang, J., Salmon, P., Robinson, D., Chartrain, M. (2007). Cholesterol delivery to NS0 cells: challenges and solutions in disposable linear low-density polyethylene-based bioreactors. *J. Biosci. Bioeng.*, 103, 50-59.
- Öncül, A.A., Kalmbach, A., Genzel, Y., Reichl, U., Thévenin, D. (2010). Characterization of flow conditions in 2 L and 20 L Wave Bioreactors[®] using Computational Fluid Dynamics. *Biotechnol. Prog.*, 26, 101-110.
- Palazón, J., Mallol, A., Eibl, R., Lettenbauer, C., Cusidó, R.M., Piñol, M.T. (2003). Growth and ginsenoside production in hairy root cultures of *Panax ginseng* using a novel bioreactor. *Planta Med.*, 69, 344-349.
- Pope, S.B. (2000). *Turbulent Flows*, University Press, Cambridge.
- Richardson, E.G., Tyler, E. (1929). The transverse velocity gradient near the mouths of pipes in which an alternating or continuous flow of air is established. *Proc. Phys. Soc.*, 42, 1-15.
- Singh, V., 1999. Disposable bioreactor for cell culture using wave-induced agitation. *Cytotechnology*, 30, 149-158.
- Stintzing, A., Pilz, R.D., Hempel, D.C., Krull, R. (2008). Mechanische Beanspruchungen in Mehrphasenreaktoren. *Chem. Ing. Tech.*, 80, 1837-1842.
- Tang, Y.J., Ohashi, R., Hamel, J.-F.P. (2007). Perfusion culture of hybridoma cells for hyperproduction of IgG(2a) monoclonal antibody in a wave bioreactor-perfusion culture system. *Biotechnol. Prog.*, 23, 255-264.
- Tropea, C., Yarin, A., Foss, J. (2007). *Springer Handbook of Experimental Fluid Mechanics*. Springer.
- Weber, W., Weber, E., Geisse, S., Memmert, K. (2002). Optimisation of protein expression and establishment of the Wave Bioreactor for Baculovirus/insect cell culture. *Cytotechnology*, 38, 77-85.

Chapter 6

CFD simulations for flow characterization in bioreactors

6.1 Introduction

Wave Bioreactors[®], as described in the previous chapter, have led to markedly different results in cell growth and product formation compared to the conventional bioreactors. This difference is expected to result from the complex, non-linear coupling between unsteady flow properties and cell viability. For a further detailed understanding of the flow conditions in the cellbags, complementary CFD simulations are necessary in addition to the experimental measurements.

The aim of this study was to investigate numerically the key flow properties in the Wave Bioreactors[®]. Corresponding computations for two reactor scales (2 L and 20 L cellbags) were performed using the CFD code ANSYS-FLUENT[®] 6.3. The unsteady, three-dimensional computations employed the Volume of Fluid (VOF) method; an Eulerian multiphase model which is able to predict correctly the free liquid surface. It was shown that the obtained flows stay in the laminar regime, confirming gentle mixing conditions. Furthermore, the obtained shear stress levels were well below known threshold values leading to damage of animal cells.

Related publication

This chapter builds on top of:

Characterization of flow conditions in 2 L and 20 L Wave Bioreactors[®] using Computational Fluid Dynamics

Alper A. Öncül^{a,*}, Andreas Kalmbach^{b,c}, Yvonne Genzel^c, Udo Reichl^{c,d},
Dominique Thévenin^a

Biotechnology Progress (2010) 26:101-110

^a*Institut für Strömungstechnik und Thermodynamik, Lehrstuhl für Strömungsmechanik und Strömungstechnik, Otto-von-Guericke-Universität Magdeburg, Universitätsplatz 2, D-39106 Magdeburg, Germany*

^b*Fachbereich Ingenieurwissenschaften II, Fachhochschule für Technik und Wirtschaft Berlin, Blankenburger Pflasterweg 102, D-13129 Berlin, Germany*

^c*Max-Planck-Institut für Dynamik komplexer technischer Systeme, Sandtorstr. 1, D-39106 Magdeburg, Germany*

^d*Institut für Verfahrenstechnik, Lehrstuhl für Bioprozesstechnik, Otto-von-Guericke-Universität Magdeburg, Universitätsplatz 2, D-39106 Magdeburg, Germany*

6.2 State of the art

For many biotechnological processes there is a strong influence of the flow conditions in the cultivation system on increase in cell concentration and product yield (Schmalzriedt et al., 2003). Control of cell growth and cell damage is in particular important for biotechnological processes using mammalian cells for production of recombinant proteins, monoclonal antibodies or vaccines. Because of their lower growth rates, their specific aeration requirements and their high shear sensitivity a detailed knowledge of the exact flow conditions is essential to design and optimize corresponding cultivation conditions. Depending on medium composition, choice of aeration and growth in suspension or on microcarriers, shear stress can have different impact on the cells used (Nienow, 2006).

Different cultivation systems like T-flasks, roller bottles, stirred tanks, and bubble columns are used for the corresponding applications (e.g., Eibl and Eibl, 2006; Freshney, 1994; Genzel and Reichl, 2007; Schmalzriedt et al., 2003; Spier, 2000). Recently, a completely new family of reactors, called Wave Bioreactors[®], has been proposed (Singh, 1999). Because of their attractive design and advantages (Singh, 2001), the Wave Bioreactors[®] are now widely applied in many scientific laboratories and industrial companies (e.g., Eibl and Eibl, 2006; Genzel and Reichl, 2007; Genzel et al., 2006; Hundt et al., 2007; Mikola et al., 2007; Palazón et al., 2003; Singh, 1999; Weber et al., 2002). In contrast to the more classical, axisymmetric stirred flow reactors relying on an internal stirring system, Wave Bioreactors[®] rely on a low-frequency, one- or multi-dimensional oscillation of the enclosed liquid. The employed flexible, disposable PET-bags, usually called wave-bags or cellbags depending on the manufacturer, can be shaken in different modes moving the liquid either gently from one side to the other, or more strongly leading ultimately to the breaking of liquid waves at the liquid surface (Eibl and Eibl, 2006; Singh, 1999). Today, available reactor sizes range from 0.05 L up to 500 L working volume. It has been observed in practice that use of these reactors leads to markedly

* Corresponding author. Tel.: +49-391-6718195; fax: +49-391-6712840.
E-mail address: oncuel@ovgu.de (A.A. Öncül).

different results for the corresponding applications. For the cultivation of adherent MDCK cells higher cell concentrations on microcarriers could be reached compared to cell growth in stirred tank reactors (Genzel et al., 2006). This is expected to result from the complex, non-linear coupling between unsteady flow properties and cell viability, similar to known observations for other chemical engineering reactors (Öncül and Thévenin, 2007).

To characterize accurately the flow conditions within the Wave Bioreactors[®] Computational Fluid Dynamics (CFD) has been employed in the present study. Numerical investigations have been carried out both for 2 L and 20 L cellbags, based on the operating conditions reported by Genzel et al. (2006). These three-dimensional, time-dependent computations fully take into account the evolution of the free liquid surface in the bag by using the Volume of Fluid (VOF) method, which is an Eulerian method proposed by Hirt and Nichols (1981). VOF has been widely employed in the past for successful prediction of various multiphase flows involving a free boundary (e.g., Gao et al., 2003; Gunjal et al., 2005; Tomiyama et al., 1993). As will be demonstrated later, the flow state in the cellbags is laminar for the investigated conditions. As a consequence, there is no need for a turbulence model, so that the computational effort is reduced.

Because the flow conditions observed in the Wave Bioreactor[®] are quite unusual, it is necessary to check and quantify the accuracy of the CFD results by appropriate experimental measurements. Some results pertaining mostly to integral quantities or to qualitative flow features can be found in the literature (Eibl and Eibl, 2006; Singh, 1999) for a wide range of practical parameter sets (rocking rate, rocking angle, filling level). Nevertheless, they do not appear to be sufficient for a comprehensive validation of the observed flow properties in time and space, as obtained from three-dimensional, time-dependent flow simulations considering the free surface of the liquid. As a consequence, specific experiments have been performed using exactly the same set of parameters as used for theoretical computations. In particular, time-dependent measurements of liquid surface height (i.e. liquid level) and liquid velocity have been carried out at many different places in the cellbag (Öncül et al., 2008). A first estimation of the liquid shear stress has also been obtained for a few selected locations.

By comparing the CFD results with the experimental data, the accuracy of the simulations could be assessed, thus allowing a quantitative validation of the developed procedure. The numerical models and settings will be described in the next section. After considering briefly the experimental setup, the obtained results will be analyzed and discussed. Finally, possible improvements and future studies are addressed.

6.3 Numerical calculations

Because of the irregular shape of the flexible cellbags, 2 L and 20 L bag geometries are quite complex during real operation conditions. Because an accurate description of the bag's geometry is essential to determine the resulting flow conditions, bag geometries were scanned under operating conditions using a laser measuring technique with a maximum uncertainty of $\pm 100 \mu\text{m}$. This technique is based on an optical sensor (OptoInspect 3D-Flex), which consists of a line laser and a camera and operates according to the split beam principle without contacting the object. Based on the digitized surfaces the geometry employed to represent the numerical domain was reconstructed using SolidWorks[®] 2008 (Fig. 6.1a). In this manner, a direct comparison of the experimental results with CFD becomes possible.

Furthermore, possible changes of the bag shape as a function of the rocking angle were analyzed for both cellbags (half-filled) with liquid. Experimental results clearly showed that such changes were completely negligible (less than 1 mm at any point), so that it was possible to consider a rigid geometry in the CFD simulation. Even if the PET bags are flexible in principle, the bag overpressure employed during real operation (about 10 mbar) combined with the rigid fixation systems of the bag on the rocking unit, was sufficient to prevent any noticeable change of the bag's geometry, independently from the operator. Moreover, no shape change due to equipment loading was observed.

After designing the real bag geometry, the numerical mesh was generated for both bags using the commercial software Gambit[®] 2.4. Since the geometry and hence the resulting flow is symmetric with

respect to the rotational mid-cross-section of the bag, only half of the full geometry was simulated by CFD, applying a symmetric boundary condition along the interface. An unstructured grid (see Fig. 6.1b-c, for the surface grid), appropriately refined in the most important flow regions was employed in the CFD. After checking systematically grid independency of the obtained CFD results for one set of parameters, the minimum number of tetrahedral volume elements needed for accurate results was found as 200,000 for the 2 L cellbag and 820,000 for the 20 L cellbag.

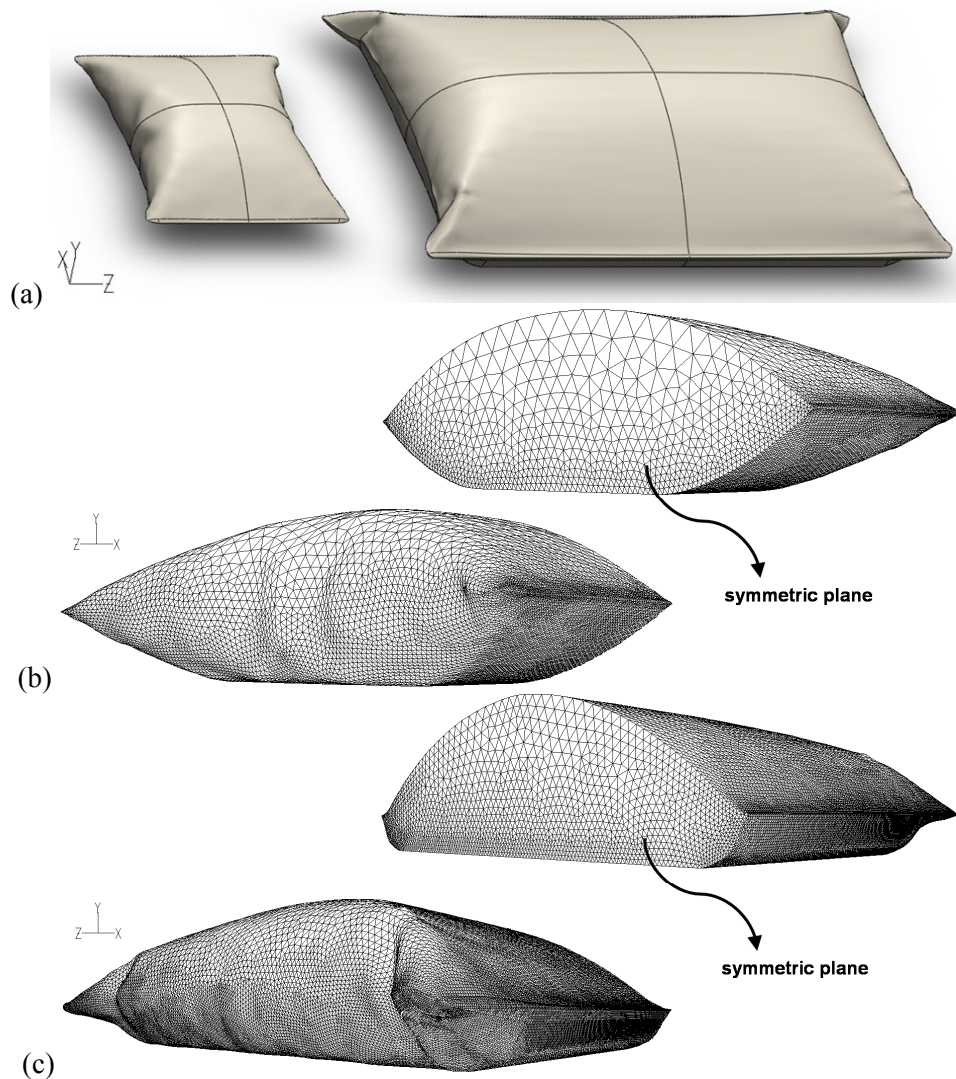


Fig. 6.1. (a) Scanned geometries of 2 L and 20 L cellbags (CB2L and CB20L cellbags, Wave Biotech AG, LDPE material), (b) surface grid of 2 L cellbag and (c) surface grid of 20 L cellbag.

All further three-dimensional, time-dependent flow simulations were carried out using the industrial CFD package ANSYS-FLUENT[®] 6.3. The variable time-stepping method was chosen instead of setting a fixed value, to obtain a more accurate temporal resolution. To simplify the simulations, it was assumed that the bag was not rotating. As a much more convenient alternative, fully equivalent from a computational point of view, the direction of the earth gravity vector was rotated in time during the simulation by comparison with the fixed orientation of the cellbag, in a manner identical to the real application. This procedure was implemented through a user-defined scheme script.

To obtain a realistic prediction of the time-dependent free liquid surface, CFD employed the VOF method. This method is applied to predict the clearly defined interface between immiscible liquids in multiphase flows (like bubble flow in liquid, jet breakup, etc.) by tracking the volume fraction of each

phase in the domain in the Eulerian framework. For the present conditions, corresponding to a full separation between the gas and the liquid phase (no wave breaking), the geometric reconstruction scheme was used. This allowed an accurate description even using unstructured meshes (Fluent Inc., 2006). Since flow was laminar in both cellbags (see below) no turbulence model was required, which reduced the computational effort.

Under these circumstances, the number of time-steps solved after reaching periodic conditions for the simulation of one complete rocking cycle (i.e. one period) was 2030 and 4417 for 2 L and 20 L cellbags, respectively. Considering the complexity of the configuration, the resulting computing time for the simulation of one period was quite high but acceptable. Calculations required about 11 h and 60 h for the 2 L and the 20 L cellbags, respectively, when using six standard PCs (Pentium-IV Linux with 2.7 GHz/2 GB memory) in a parallel simulation.

6.4 Experimental measurements

As the present article concentrates on the results obtained by CFD and on their analysis, the experimental methods are not described here for the sake of simplicity (corresponding experiments were commented at length in Chapter 5). It is worth reminding that the conditions encountered in the experiments were identically taken into account for the corresponding CFD computations in order to carry out meaningful comparisons.

6.5 Results and discussion

The locations of the concerned measurements in the cellbags and the corresponding label for each location are shown in Fig. 6.2 to facilitate understanding the exact positions of the profiles presented later in this section. Additionally, the two horizontal and fully inclined positions of the 2 L cellbag during one rocking cycle are depicted in Fig. 6.3 as a function of time. Similar structures were obtained for the 20 L bag. Fig. 6.3 should be helpful later to better understand the instantaneous position of the liquid volume versus time, when considering liquid surface height, velocity and shear stress.

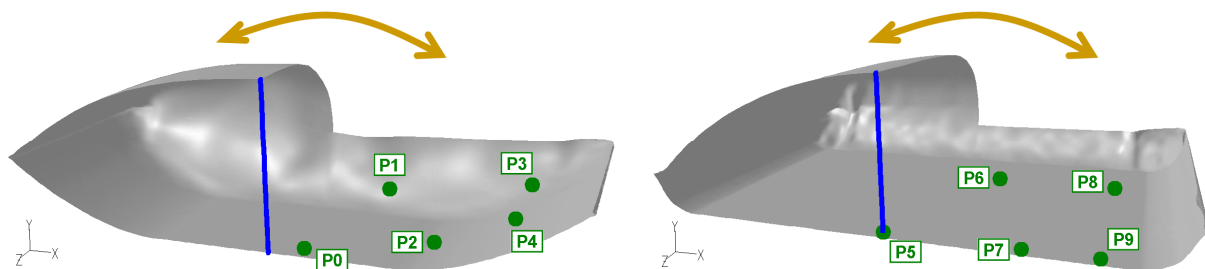


Fig. 6.2. Measurement locations in 2 L (left) and 20 L (right) cellbags. The arrows indicate schematically the rocking direction. The blue vertical line corresponds to the center of the bag.

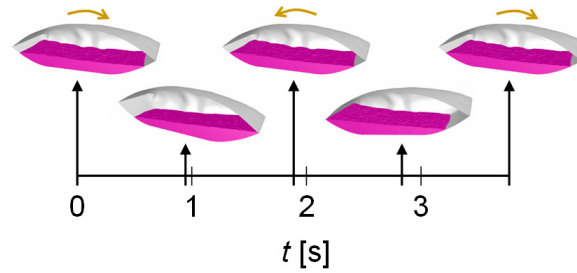


Fig. 6.3. The two horizontal and fully inclined positions of the 2 L cellbag as a function of time during one rocking cycle. The arrows indicate schematically the rocking direction at that time instant. The instantaneous liquid surface (magenta) was obtained by the VOF technique.

The time evolution of the mean liquid velocity (u_{mean}) along the central vertical line (Fig. 6.2) of the 20 L cellbag is given in Fig. 6.4 according to the results of the CFD simulations starting from rest. As can be seen clearly, the liquid flow became fully periodic after around 10 s. Similarly, the periodicity onset in the 2 L cellbag was roughly 30 s, indicating a slightly slower flow establishment, which might be because of the sharper edges and corners, and to the marked convexity of the bottom side of this bag (not shown). Both values corroborated well experimental observations.

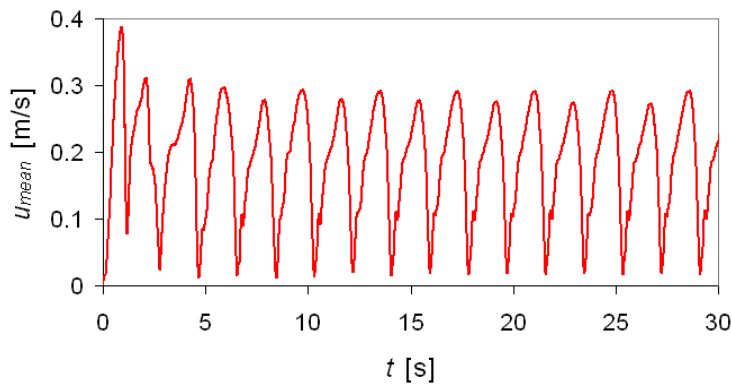


Fig. 6.4. Mean liquid velocity profile according to the numerical results along the central vertical line in 20 L cellbag.

From now on, all the numerical results presented in this article concern the values obtained after reaching full flow periodicity. Hence, the time axis starting from zero in the following plots should not be confused with a newly initiated flow process.

The resulting mean liquid Reynolds numbers (Re_{mean}) during one period (i.e. one rocking cycle) along the central vertical lines (vertical lines in Fig. 6.2) are shown in Fig. 6.5. Here, Re_{mean} was calculated according to the standard expression

$$Re_{mean} = \frac{u_{mean} H_{center}}{\nu} \quad (6.1)$$

where H_{center} is the instantaneous liquid height along the central vertical line and ν is the kinematic viscosity of water.

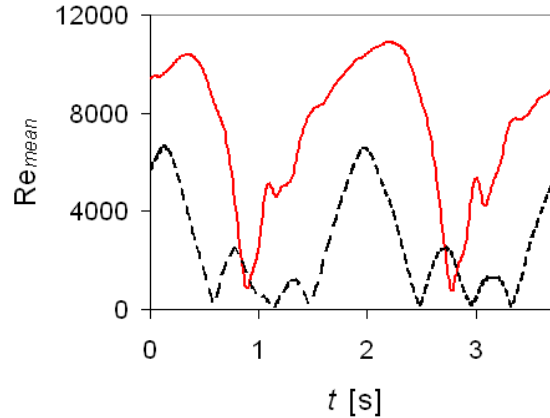


Fig. 6.5. Liquid Reynolds number profiles for one period according to the numerical results along the central vertical lines in 2 L (dashed line) and 20 L (solid line) cellbags.

The accepted value for transition to turbulence in an axisymmetric tube is $Re_{critical} \approx 2300$. Considering this value, it is unclear from Fig. 6.5 if the flow is laminar or turbulent, in particular for the 20 L cellbag. However, the present configuration has almost nothing in common with a steady turbulent flow in a tube. Therefore, a more specific analysis of the flow state was needed, as presented next.

6.5.1 Flow state analysis

Before initiating the CFD simulations, characterization of the flow state in the cellbags was necessary for a proper choice of the models implemented within the numerical domain. The experimental investigation of Kurzweg et al. (1989) considering the estimation of turbulence onset in unsteady oscillating water flows was particularly interesting for this purpose.

Kurzweg et al. (1989) quantified the turbulence onset as a function of the non-dimensional Womersley number (Wo) and of a parameter β . Wo is a classical non-dimensional number used to quantify the unsteady nature of a flow. It is expressed as (see e.g. Loudon and Tordesillas, 1998)

$$Wo = \frac{L}{2} \sqrt{\frac{\omega}{\nu}} \quad (6.2)$$

where, L denotes the characteristic length scale of the flow (which is, in our case, given by the liquid level in the cellbags) and ω is the angular velocity of the oscillations. The obtained value for Wo corresponds to 19.0 and 23.6 for 2 L and 20 L cellbags, respectively, when the operating conditions and the filling levels mentioned above are inserted. A value $Wo > 1$ corresponds to a flow strongly modified by unsteady effects, which is not unexpected in the present configuration. Concerning the transition to turbulence, turbulence first appears in oscillating flows when β exceeds 700 for Wo greater than 8.5 (Kurzweg et al., 1989).

The dimensionless parameter β is defined as follows

$$\beta = \Delta x \sqrt{\frac{\omega}{\nu}} \quad (6.3)$$

where, Δx indicates the maximum fluid element displacement in the vessel during one cycle. A CFD simulation has been carried out employing the Lagrangian discrete phase model and regularly distributed tracers to compute this maximum displacement in the 2 L cellbag. It was found that $\Delta x = 0.122$ m, corresponding to about 40% of the bag length along the rocking direction. Consequently, β

equals to 188.5 for the 2 L cellbag. Similarly, assuming that the maximum displacement would correspond again to around 40% of the bag length in the 20 L cellbag, one estimates a value of β equal to 273.2. Considering these values (which are much below 700), it can definitely be concluded that the liquid flow in both bags is in the laminar state. Hence, no turbulence model is needed in the numerical calculations, so that the computational effort is considerably reduced. This statement would even remain true when using for Δx the full bag length (which is obviously the maximum possible value). Note, however, that the situation might be different for much larger bags.

As an additional control, a CFD simulation employing the low-Reynolds k - ε turbulence model was performed for the 2 L cellbag. Apart from an increase in computing time, no significant difference was observed, confirming once again laminar flow conditions.

6.5.2 Liquid level

The liquid surface height (H_i) profiles according to the results of experimental and numerical investigations for one rocking period at various locations in the 2 L cellbag are shown in Fig. 6.6. These values denote the liquid level above the rocking platform, which does not necessarily mean above the bag bottom, especially at P2 and P3 (curved bottom). Although some slight discrepancies were observed between the numerical results and experimental data, both yielded qualitatively the same trend and agreed very well with each other. The liquid level at P0 fluctuated only slightly since this position is located in the central region of the cellbag, where the amount of liquid did not change considerably. On the contrary, the water reached a level of around 40 mm at P3, which was almost twice the level at P0 when the cellbag was inclined to this side. Moreover, the liquid disappeared at P3 as expected while the bag leaned to the opposite side.

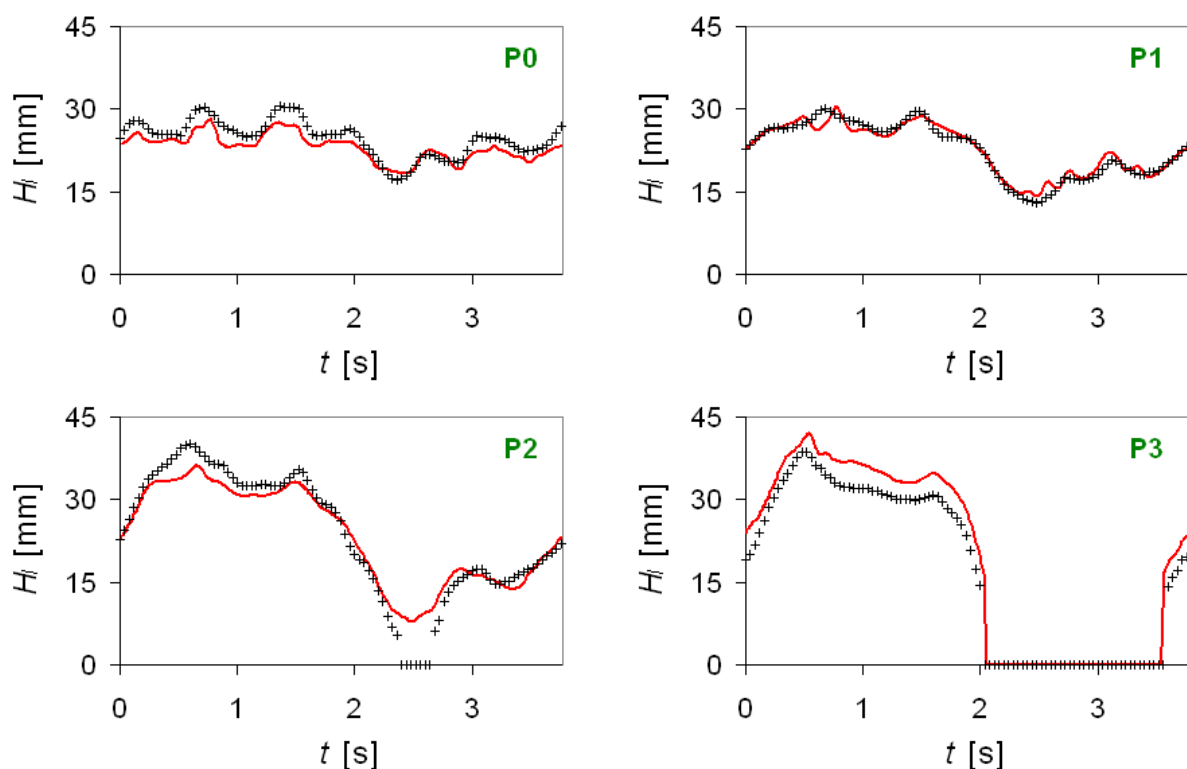


Fig. 6.6. Liquid surface height profiles for one period according to the numerical results (lines) compared to experimental data (plus symbols) at various locations in the 2 L cellbag (Measurement locations: see Fig. 6.2).

Plots of H_i at various locations in the 20 L cellbag are additionally given in Fig. 6.7. Once again, the qualitative trend of the predicted wavy motion was quite close to that of the measured one. Only slight quantitative discrepancies were observed from time to time.

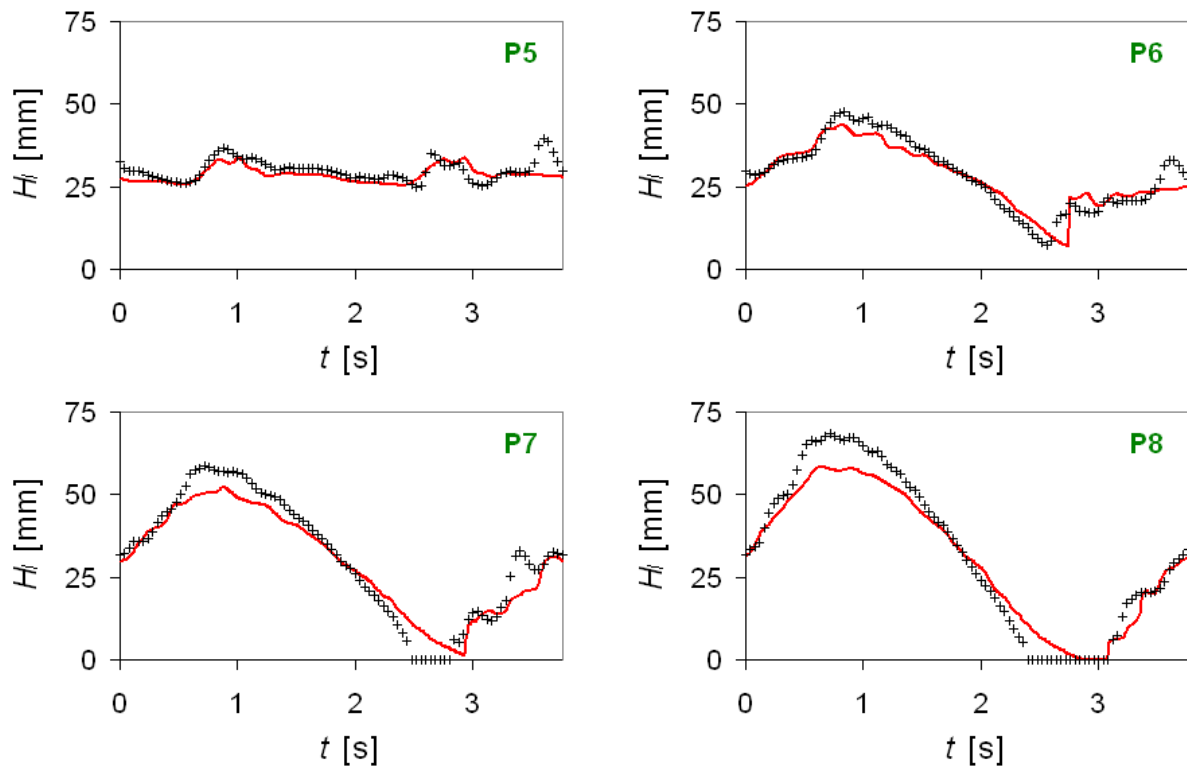


Fig. 6.7. Liquid surface height profiles for one period according to the numerical results (lines) compared to experimental data (plus symbols) at various locations in the 20 L cellbag (Measurement locations: see Fig. 6.2).

As a whole, the CFD predictions for the liquid surface height in the 2 L and 20 L bags under the mentioned operating conditions were in very satisfactory agreement with the experimental data. This was a first positive test (validation) of the simulation procedure.

6.5.3 Liquid velocity

The numerical results for the magnitude of the liquid velocity in the direction of rotation (u_x) in the 2 L cellbag (respectively in the 20 L cellbag) are shown in Fig. 6.8 (respectively in Fig. 6.9) in comparison to experimental data. Only this velocity component will be discussed in what follows. Both numerical and experimental results in these plots show values obtained 5 mm above the bag bottom at each stated location. It is worth reminding that the velocity at a location was null whenever no liquid flowed at that position because the hot film probe measured only the velocity in the liquid phase. Therefore, the numerical results, too, only show the values in the liquid phase.

The maximum velocity in the 20 L cellbag was greater than that in the 2 L cellbag, which can be explained by the lower filling level in the 20 L bag as well as by the larger magnitude of the displacement induced by the larger bag length. As expected, the liquid especially in the middle region of both cellbags (i.e. at P0 and P1 as well as at P5 and P6) flowed faster when the bags aligned horizontally (i.e. at $t = 0$ and ~ 2 s, see Fig. 6.3) due to the maximum angular speed of the rocking platform at this position. Furthermore, the average velocity in the side regions of the cellbags was lower than that in the middle region, because the liquid motion is constrained by the walls of the bags.

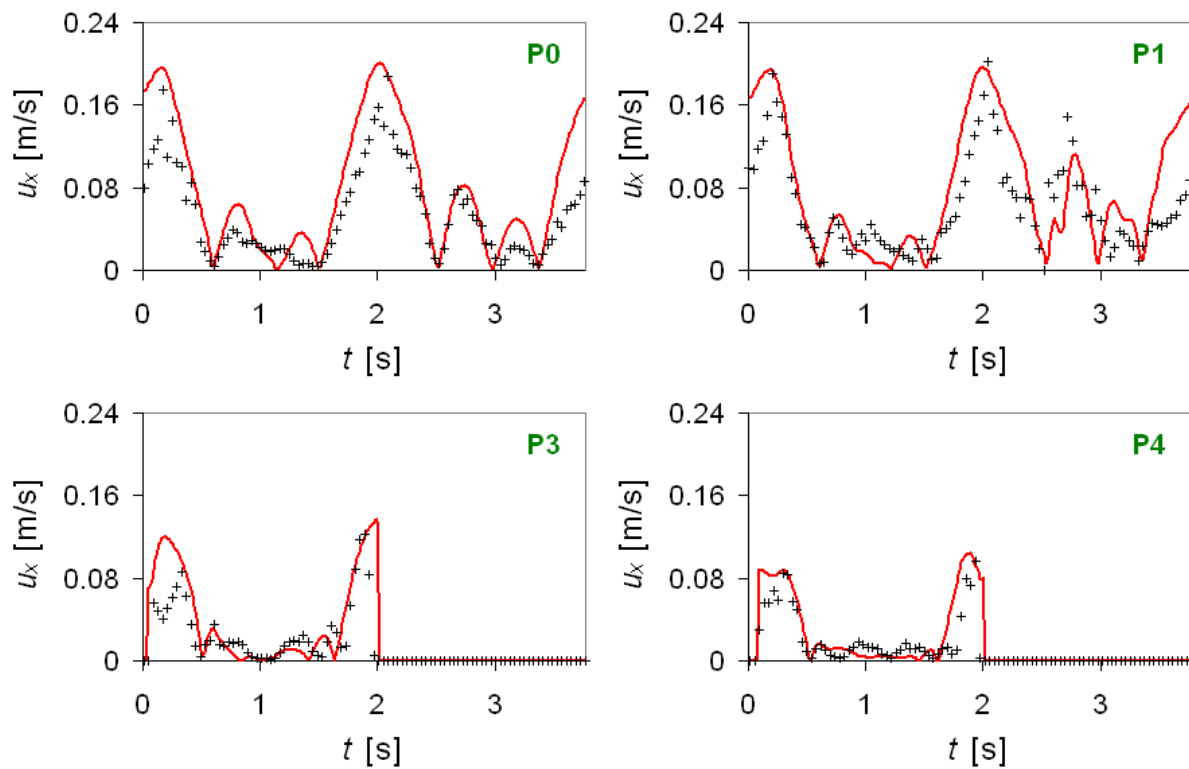


Fig. 6.8. Profiles for the magnitude of the liquid velocity for one period according to the numerical results (lines) compared to experimental data (plus symbols) at various locations (5 mm above the bag bottom) in the 2 L cellbag (Measurement locations: see Fig. 6.2).

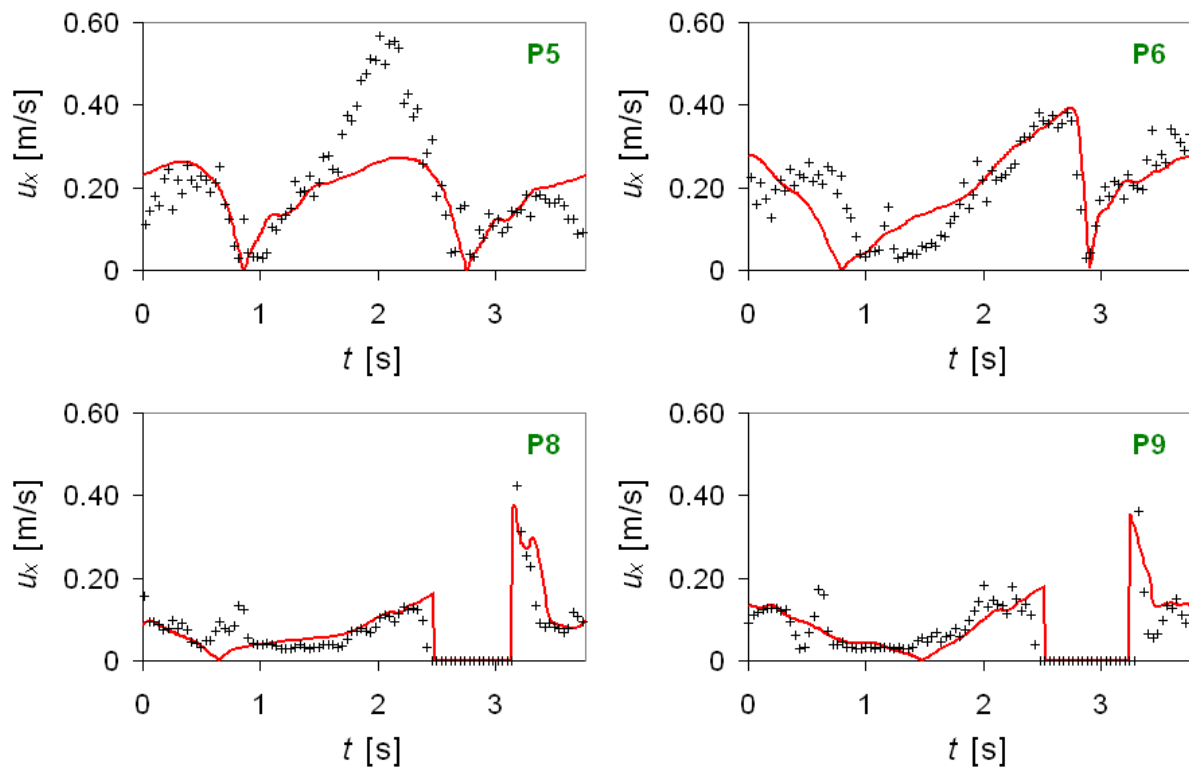


Fig. 6.9. Profiles for the magnitude of the liquid velocity for one period according to the numerical results (lines) compared to experimental data (plus symbols) at various locations (5 mm above the bag bottom) in the 20 L cellbag (Measurement locations: see Fig. 6.2).

In addition to these, velocity plots at various heights above the bag bottom are shown in Fig. 6.10 as well as in Fig. 6.11 for 2 L and 20 L cellbags, respectively. Although the highest velocity at P2 in the 2 L cellbag was almost identical at various heights, this was not the case for P7 in the 20 L cellbag. Instead, the maximum velocity at 5 mm (circa 0.35 m/s) was greater than that at 12 and 22 mm (circa 0.25 m/s). The fact that the maximum velocity was larger near the bag bottom rather than at the liquid surface could be surprising at first. It can in fact be easily supported, however, by a literature analysis concerning oscillating flows (see e.g., Loudon and Tordesillas, 1998, and references within; Richardson and Tyler, 1929). It has been known for a long time that the peak velocities obtained for oscillating flows in tubes migrate from the center line (steady case) towards the wall when increasing the oscillation rate (and thus Wo). Consequently, the fact that this was observed for the 20 L cellbag only confirms that unsteady effects become stronger, as documented by the higher value of Wo compared to the 2 L cellbag.

The quantitative agreement between the numerical and the experimental results was again quite good, although some differences were observed at isolated positions, in particular at P5 for the 20 L cellbag. The observed differences are probably partly because of experimental uncertainties, which are considerably higher for the velocity measurement, both concerning the absolute accuracy ($\pm 13\%$) and the precise positioning of the probe. As a whole, the agreement is better for the 2 L cellbag than for the 20 L bag, which might be a consequence of the more difficult measurements in the larger bag, due to the previously mentioned weight problems on the rocking unit.

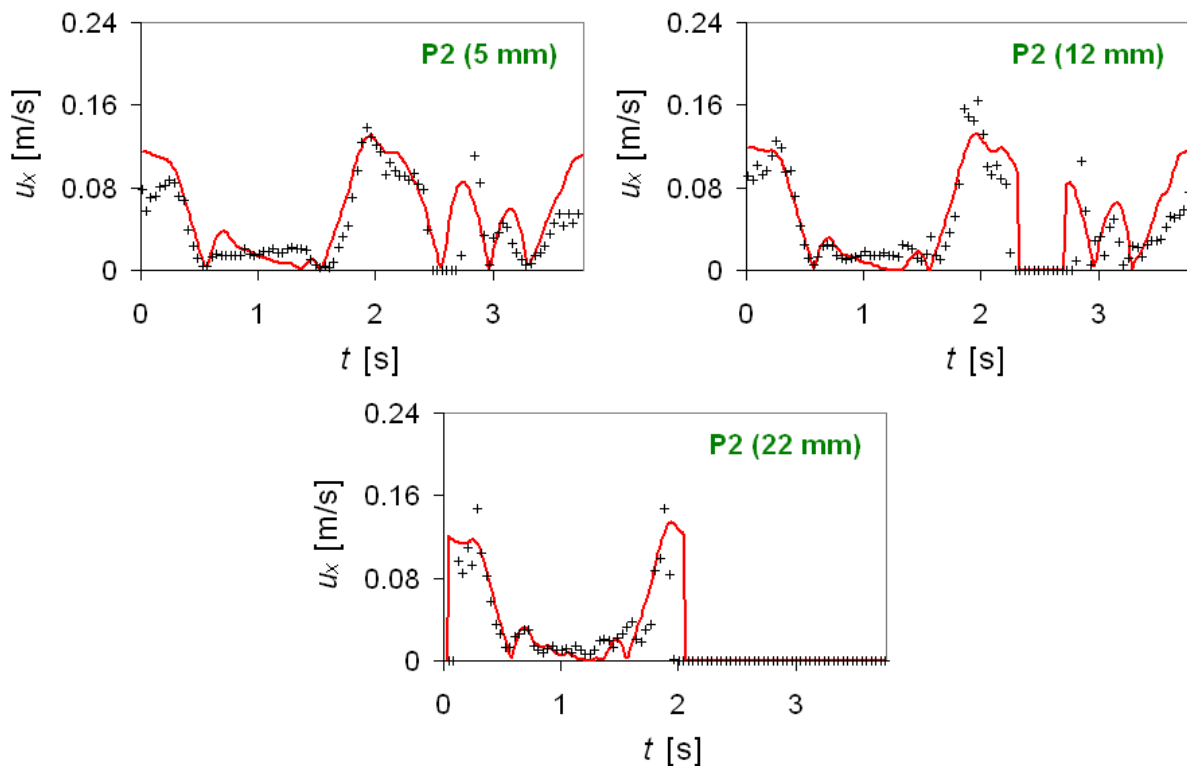


Fig. 6.10. Profiles for the magnitude of the liquid velocity for one period according to the numerical results (lines) compared to experimental data (plus symbols) at location P2 and at various heights above bag bottom in the 2 L cellbag (Measurement locations: see Fig. 6.2).

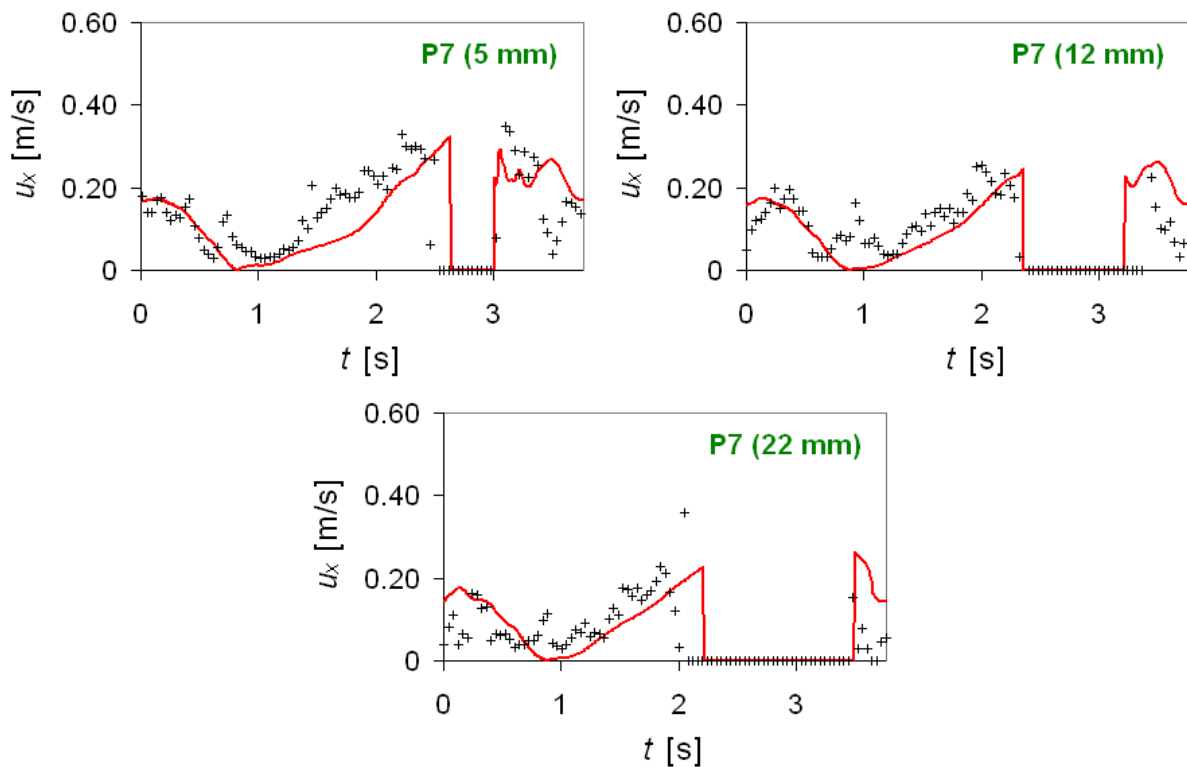


Fig. 6.11. Profiles for the magnitude of the liquid velocity for one period according to the numerical results (lines) compared to experimental data (plus symbols) at location P7 and at various heights above bag bottom in the 20 L cellbag (Measurement locations: see Fig. 6.2).

6.5.4 Liquid shear stress

First investigations regarding liquid shear stress (τ_l) were also made at some selected positions in the liquid. The agreement between the numerical results and the experimental data was sometimes quite satisfactory (Fig. 6.12) but differed by an order of magnitude at other positions. As a matter of fact, currently no probes are available to measure in an accurate manner the shear stress in the bulk of the liquid. Therefore, further studies have been started to measure in a much more accurate manner the wall shear stress at the bottom of the bag.

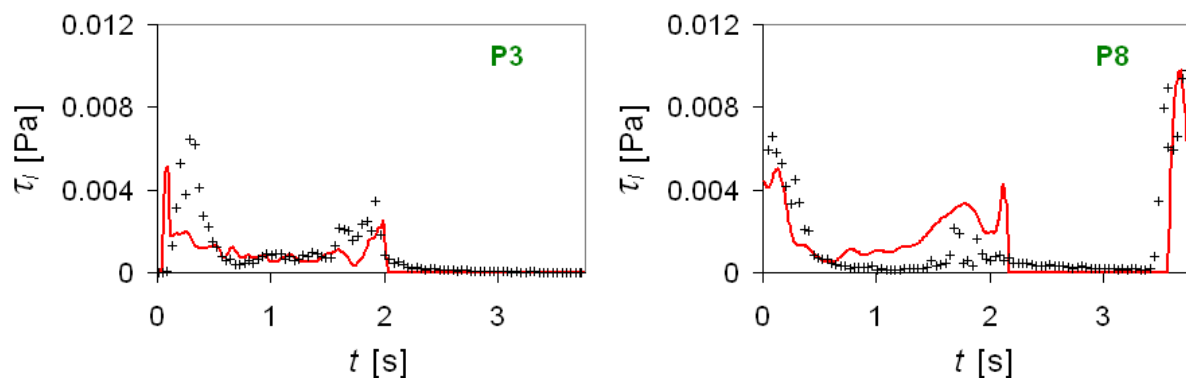


Fig. 6.12. Liquid shear stress profiles for one period according to the numerical results (lines) compared to the experimental data (plus symbols) at two locations in the 2 L (left) and the 20 L (right) cellbags (Measurement locations: see Fig. 6.2).

Nevertheless, the presented results from simulations as well as from measurements clearly suggest very low values for the shear stress in the cellbags (maximum around 0.01 Pa) compared to classical stirred bioreactors, in which values exceeding 1 Pa can be observed (Joshi et al., 1996). This low value probably explains some of the observations found in the literature concerning cultivation in cellbags, considering that a shear stress threshold of at least 0.7 Pa is associated with lethal damage of anchorage-dependent animal cell types (Croughan and Wang, 1991). It could be shown that cells that were usually difficult to cultivate at larger scales gave acceptable results in cellbags (Palazón et al., 2003), and adherent cells grew to higher cell densities on microcarriers in comparison to stirred tank bioreactors (Genzel et al., 2006). Of course, it certainly has to be considered first if adherent cells growing on fast precipitating microcarriers, or growth of suspension cells is of central interest. The recent tendency towards chemically defined, serum-free, animal-component free or protein-free media has an additional effect on cultivation results, as cells become even more sensitive with such poorer media. In other reactors, issues like air bubble entrainment and its connection to local shear stress (Koynov et al., 2007) could also have important effects.

6.6 Conclusions and remarks

In the present chapter, flow conditions in two different Wave Bioreactors[®] (2 L and 20 L cellbags) have been characterized using numerical simulations. This has been realized by solving the time-dependent liquid flow using the CFD technique. The unsteady, three-dimensional simulations include the VOF method, an Eulerian multiphase model which is able to predict the free liquid surface. The operating conditions considered in the computations correspond to those typically used in animal cell cultivation processes. On the basis of such systematic simulations, the possibility of a successful control of cell growth and cell damage during the process can be assessed by checking numerically the influence of each process parameter on the flow properties impacting cell development.

Wave Bioreactors[®] are currently available up to 1000 L total volume (corresponding to maximum 500 L working volume). At larger volumes and with different geometries of the cellbags analogous measurements and computations should clarify the existing flow conditions. At a larger scale different flow properties (e.g. concerning turbulence) are expected, requesting further work.

To quantify the accuracy of the simulations, experimental measurements of important fluid flow quantities (liquid level, liquid velocity, and liquid shear stress) have also been performed (see previous chapter). The general agreement between the numerical results and experimental data was very satisfactory. Thus, the predictions of the developed simulation procedure, relying on the industrial software ANSYS-FLUENT[®] 6.3, have been successfully validated through these experiments.

One important conclusion is that a very low level of shear stress was found in both cellbags compared to classical stirred tank reactors. Furthermore, the flow was observed to be laminar in both cellbags. This confirms the gentle liquid motion obtained in such reactors, which should significantly reduce cell damage.

From a numerical point of view, more complex simulations can now be carried out to couple dynamically the evolution of cell populations (suspension and adherent cell lines) with the obtained flow conditions. In this manner, it will become ultimately possible to optimize cultivation conditions in animal cell culture processes.

References of Chapter 6

- Croughan, M.S., Wang, D.I. (1991). Hydrodynamic effects on animal cells in microcarrier bioreactors. *Biotechnology*, 17, 213-249.
- Eibl, R., Eibl, D. (2006). Design and use of the wave bioreactor for plant cell culture. *Plant Tissue Culture Engineering*, (Dutta Gupta, S., and Ibaraki, Y., Eds.), Dordrecht: Springer, 203-227.
- Fluent Inc. *Fluent 6.3 User's Guide*, Lebanon, USA, 2006.
- Freshney, R.I. (1994). *Culture of Animal Cells: A Manual of Basic Technique*, Third Edition, New York: Wiley-Liss, Inc.
- Gao, D., Morley, N.B., Dhir, V. (2003). Numerical simulation of wavy falling film flow using VOF method. *J. Comp. Phys.*, 192, 624-642.
- Genzel, Y., Olmer, R.M., Schäfer, B., Reichl, U. (2006). Wave microcarrier cultivation of MDCK cells for influenza virus production in serum containing and serum-free media. *Vaccine*, 24, 6074-6087.
- Genzel, Y., Reichl, U. (2007). Vaccine production – state of the art and future needs in upstream processing. *Animal Cell Biotechnology – Methods and Protocols*, (Pörtner, R., Ed.), Totowa: HUMANA Press Inc., 457-473.
- Gunjal, P.R., Ranade, V.V., Chaudhari, R.V. (2005). Dynamics of drop impact on solid surface: Experiments and VOF simulations. *AIChE J.*, 51, 59-78.
- Hirt, C.W., Nichols, B.D. (1981). Volume of fluid (VOF) method for the dynamics of free boundaries. *J. Comp. Phys.*, 39, 201-225.
- Hundt, B., Best, C., Schlawin, N., Kaßner, H., Genzel, Y., Reichl, U. (2007). Establishment of a mink enteritis vaccine production process in stirred-tank reactor and Wave[®] Bioreactor microcarrier culture in 1-10 L scale. *Vaccine*, 25, 3987-3995.
- Joshi, J.B., Elias, C.B., Patole, M.S. (1996). Role of hydrodynamic shear in the cultivation of animal, plant and microbial cells. *Chem. Eng. J.*, 62, 121-141.
- Koynov, A., Tryggvason, G., Khinast, J.G. (2007). Characterization of the localized hydrodynamic shear forces and dissolved oxygen distribution in sparged bioreactors. *Biotechnol. Bioeng.*, 97, 317-331.
- Kurzweg, U.H., Lindgren, E.R., Lothrop, B. (1989). Onset of turbulence in oscillating flow at low Womersley number. *Phys. Fluids A: Fluid Dynam.*, 1, 1972-1975.
- Loudon, C., Tordesillas, A. (1998). The use of the dimensionless Womersley number to characterize the unsteady nature of internal flow. *J. Theor. Biol.*, 191, 63-78.
- Mikola, M., Seto, J., Amanullah, A. (2007). Evaluation of a novel Wave Bioreactor[®] cellbag for aerobic yeast cultivation. *Bioprocess Biosyst. Eng.*, 30, 231-241.
- Nienow, A.W. (2006). Reactor engineering in large scale animal cell culture. *Cytotechnology*, 50, 9-33.
- Öncül, A.A., Thévenin, D. Influence of hydrodynamic conditions on particle size distribution. *Proceedings of the 6th European Congress of Chemical Engineering – ECCE6*, (Gani, R., and Dam-Johansen, K., Eds.), ISBN 978-87-91435-57-9, 2:229-230, Copenhagen, Denmark, September 2007.
- Öncül, A.A., Thévenin, D., Genzel, Y., Reichl, U. Characterization of flow conditions in wave bioreactors using CFD. *7th European Symposium on Biochemical Engineering Science – ESBES-7*, Paper 1064, Faro, Portugal, September 2008.
- Palazón, J., Mallol, A., Eibl, R., Lettenbauer, C., Cusidó, R.M., Piñol, M.T. (2003). Growth and ginsenoside production in hairy root cultures of *Panax ginseng* using a novel bioreactor. *Planta Med.*, 69, 344-349.
- Richardson, E.G., Tyler, E. (1929). The transverse velocity gradient near the mouths of pipes in which an alternating or continuous flow of air is established. *Proc. Phys. Soc.*, 42, 1-15.
- Schmalzriedt, S., Jenne, M., Mauch, K., Reuss, M. (2003). Integration of physiology and fluid dynamics. *Advances in Biochemical Engineering/Biotechnology*, (von Stockar, U., and van der Wielen, L.A.M., Eds.), Berlin/Heidelberg: Springer Verlag, 80, 19-68.

- Singh, V. (1999). Disposable bioreactor for cell culture using wave-induced agitation. *Cytotechnology*, 30, 149-158.
- Singh, V. (2001). Method for culturing cells using wave-induced agitation. *United States Patent*, Patent No. US 6,190,913 B1.
- Spier, R.E. (Ed.) (2000). *Encyclopedia of Cell Technology*, New York: Wiley, 183-278.
- Tomiya, A., Zun, I., Sou, A., Sakaguchi, T. (1993). Numerical analysis of bubble motion with the VOF method. *Nucl. Eng. Des.*, 141, 69-82.
- Weber, W., Weber, E., Geisse, S., Memmert, K. (2002). Optimisation of protein expression and establishment of the Wave Bioreactor for Baculovirus/insect cell culture. *Cytotechnology*, 38, 77-85.

Chapter 7

Simulation of animal cell cultivation using reduced PBM

7.1 Introduction

It is in principle necessary to take into account accurately the complete system in order to identify possible optimization strategies for cultivation conditions. CFD techniques can be employed for a detailed analysis of the cultivation process together with the unsteady flow conditions. However, due to the complexity of the resulting numerical configuration, such sophisticated computations cannot fully account for the long cultivation times (several days) yet. For this reason, model reduction must be introduced.

The aim of this chapter was to investigate the cultivation of mammalian MDCK (Madin-Darby Canine Kidney) cells in a microcarrier (MC) system using a reduced PBM based on a two-population balance approach. Although the applied PBM would reduce the computational effort considerably compared to more standard approaches, it was still unfeasible to perform three-dimensional simulations in time. This limitation was partly due to the complexity of the numerical configuration employing the VOF method and partly to the non-applicability of further reduction techniques (like frozen flow conditions) resulting from the oscillating behavior of the liquid flow with a free surface. Therefore, a reduction from three- to zero-dimensional computations had to be realized in order to reduce the computational time. For this purpose, the computations were carried out for a homogeneous system but taking into account the flow conditions, especially the peak values of shear stress observed during full CFD computations. However, those were below critical values from the literature for similar animal cells. The corresponding model reduction is described in detailed in this chapter. Moreover, optimization of the specific rates used in the cultivation kinetic equations is also presented, finally leading to a closer agreement with experimental measurements.

Related publication

This chapter builds on top of:

Two-population CFD simulation: microcarrier system for adherent cell growth in Wave Bioreactors[®]

Alper A. Öncül^{a,*}, Gábor Janiga^a, Yvonne Genzel^b, Udo Reichl^b, Dominique Thévenin^a

4th International Conference on Population Balance Modelling (2010), Berlin, pp. 667-681

^a*Institut für Strömungstechnik und Thermodynamik, Lehrstuhl für Strömungsmechanik und Strömungstechnik, Otto-von-Guericke-Universität Magdeburg, Universitätsplatz 2, D-39106 Magdeburg, Germany*

^b*Max-Planck-Institut für Dynamik komplexer technischer Systeme, Sandtorstr. 1, D-39106 Magdeburg, Germany*

7.2 State of the art

In most cultivation systems, there is a strong influence of the flow conditions on physiological status of cells and product formation (Schmalzriedt et al., 2003). Therefore, the detailed understanding of growth characteristics and of factors related to cell damage and cell deterioration in the complex flows found in bioreactors is essential to improve and optimize corresponding processes. This is particularly true for mammalian cells, used e.g. for production of recombinant proteins, monoclonal antibodies or vaccines (Genzel and Reichl, 2007), since those cells are highly sensitive to shear stress.

Different cultivation systems like T-flasks, roller bottles, stirred tanks, and bubble columns are being used for biotechnological applications (e.g. Eibl and Eibl, 2006; Freshney, 1994; Genzel and Reichl, 2007; Schmalzriedt et al., 2003; Spier, 2000). A possible alternative to these well-established cultivation systems is a bioreactor with wave-induced motion, like the Wave Bioreactor[®] (Fig. 7.1) which has been proposed some years ago (Singh, 1999 and 2001). This system consists of a cellbag on a wave holder that periodically inclines and declines. This motion induces a flow with a wavy free surface in the liquid volume (cell suspension). Wave Bioreactors[®] are now widely applied in many scientific laboratories and pharmaceutical industry (e.g. Eibl and Eibl, 2006; Genzel and Reichl, 2007; Genzel et al., 2006; Mikola et al., 2007; Palazón et al., 2003; Singh, 1999) due to their attractive design and advantages like single-use operation, low design complexity and a fast setup of new production lines (Singh, 2001). Currently, cellbags are available up to a working volume of 500 L.

Use of Wave Bioreactors[®] has led to markedly different results for some biotechnological applications. For instance, for adherent MDCK (Madin-Darby Canine Kidney) cells in microcarrier (MC) systems higher cell concentrations could be obtained compared to stirred tank cultivations performed under similar growth conditions (Genzel et al., 2006). A maximum number of about 350 cells/MC was observed in the Wave Bioreactor[®], while there were only about 250 cells/MC covering the MC surface in a comparable stirred tank bioreactor (STR). This difference was in particular assumed to be related to the unsteady flow field and to the expected lower shear stress in the Wave Bioreactor[®]. Experimental measurements as well as numerical computations performed in previous studies (Kalmbach et al., 2010; Öncül et al., 2010) confirmed that there is indeed a lower level of shear stress compared to other conventional bioreactors. Moreover, it was shown that the unsteady flow is in the laminar regime indicating a gentle mixing in the cellbags (Öncül et al., 2010).

* Corresponding author. Tel.: +49-391-6718195; fax: +49-391-6712840.
E-mail address: oncuel@ovgu.de (A.A. Öncül).

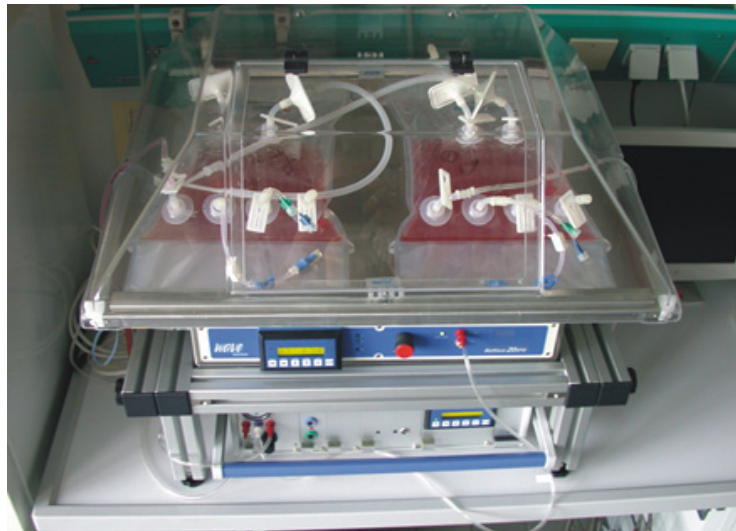


Fig. 7.1. Bioreactor with wave-induced motion with two cellbags (2 L) on its holder. Inclination/declination motion of the holder is along top-bottom direction with respect to this picture.

Mathematical models for growth of suspension and anchorage-dependent cells have been established since the 1970s (Möhler et al., 2008). In contrast, Computational Fluid Dynamics (CFD) simulations in bioreactors employing population balance models (PBMs) to describe cell growth dynamics just started recently, at the beginning of this century (e.g. Bezzo et al., 2003; Lapin et al., 2006; Zhang et al., 2009). Due to continuous progress in development of efficient numerical methods and to the availability of more accurate models, a growing number of research groups now consider such problems. However, for long cultivation times dynamic modelling of cell populations coupled with unsteady flow is still much beyond the capabilities of current CFD techniques and computers (Bezzo et al., 2003).

In the present study, CFD simulations have been employed to investigate numerically the time course of the distribution and properties of two interacting populations: animal cells on MCs and in suspension. Due to the complexity of the three-dimensional numerical configuration and to the long cultivation time (4 days), the final simulations rely on a model reduction, in which a zero-dimensional (i.e., spatially homogeneous) model represents the dynamic evolution of the populations. However, the impact of shear stress is taken into account in principle by carrying out first a full three-dimensional CFD simulation of the flow. In addition, the parameters controlling cell kinetics have been optimized for the conditions found in Wave Bioreactors[®], leading finally to a good agreement between numerical results and experimental data.

7.3 Cultivation kinetics and model equations

The cultivation kinetics of the adherent MDCK cells in the MC system were described by four main mechanisms: attachment, detachment, growth and death (Fig. 7.2).

During a lag phase of about 24 h after inoculation cells in suspension attach to the surface of spherical MCs (Cytodex 1, GE Healthcare, Uppsala, Sweden). Afterwards, cell concentration increases (proliferation phase) until a monolayer of confluent cells covers the MCs (stationary phase). The maximum cell number per MC obtained experimentally (350 cells/MC) is retained as a limiting factor for cell growth in the model (Fig. 7.2). Cells remaining in suspension or cells detaching from the MCs die after some hours due to apoptosis. More details including time courses of main metabolites can be found in Möhler et al. (2008).

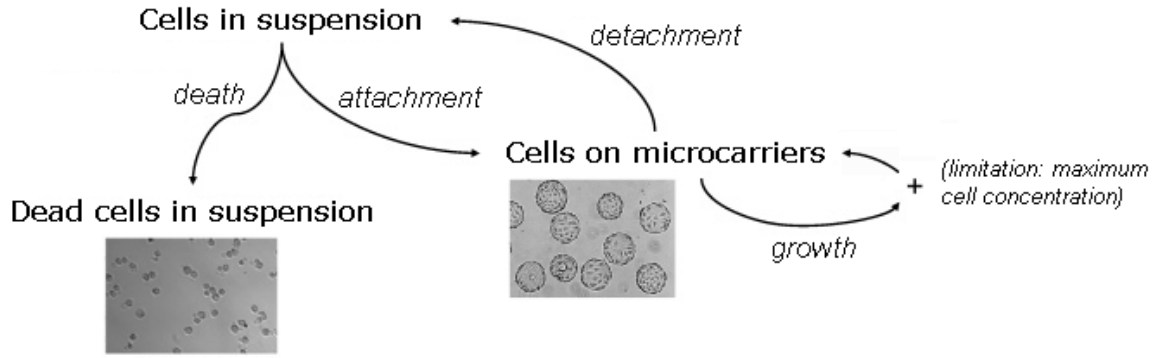


Fig. 7.2. Sketch of the cultivation model and coupling between the cells and the microcarriers.

Based on the mechanisms shown in Fig. 7.2 with the MC surface as the main factor limiting maximum cell concentration, the change with time (t) in the concentration of cells on MCs (X_{MC}), in the total concentration of viable cells (X_{sus}) and in the concentration of dead cells (X_d) in suspension can be formulated as follows (Möhler et al., 2008):

$$\frac{dX_{MC}}{dt} = \mu X_{MC} + k_{at} \frac{X_{max} - X_{MC}}{X_{max}} X_{sus} - k_{det} X_{MC} \quad (7.1)$$

$$\frac{dX_{sus}}{dt} = k_{det} X_{MC} - k_{at} \frac{X_{max} - X_{MC}}{X_{max}} X_{sus} - k_d X_{sus} \quad (7.2)$$

$$\frac{dX_d}{dt} = k_d X_{sus} - k_{lys} X_d \quad (7.3)$$

where μ indicates the specific cell growth rate which is expressed as

$$\mu = \mu_{max} \frac{X_{max} - X_{MC}}{X_{max}} \quad (7.4)$$

and μ_{max} as maximum specific cell growth rate and X_{max} as maximum concentration of cells on MCs at confluence. Dead cells X_d eventually lyse. However, as the concentration of these cells can only be determined indirectly by experimental measurements, the concentration of the lysed cells is here only subtracted from the source term of dead cells. Note that any substrate limitations or inhibitor accumulations are assumed to be negligible in the present modelling approach. Hence, release and uptake of metabolites are not taken into account yet. Further studies have demonstrated that cell growth in Wave Bioreactors[®] is not limited by partial pressure of oxygen under the given cultivation conditions.

The specific kinetic rates given in the above equations have been estimated based on experimental data obtained from a stirred tank bioreactor, assuming first-order reaction kinetics. Corresponding results are presented in Table 7.1 with their respective standard deviations (Möhler et al., 2008).

Table 7.1. Specific rates measured in a stirred tank bioreactor. All values in h^{-1} .

| Parameter | Mean value | Standard deviation (%) |
|---|------------|------------------------|
| Specific attachment rate, k_{at} | 0.0339 | 129.26 |
| Specific detachment rate, k_{det} | 0.00203 | 49.75 |
| Specific death rate, k_d | 0.07 | 42.86 |
| Specific lysis rate, k_{lys} | 0.35 | 85.71 |
| Maximum specific growth rate, μ_{max} | 0.0642 | 28.42 |

7.4 Numerical methods

In this section, the numerical methods and models used for the simulation of MDCK cell growth in a Wave Bioreactor[®] are explained.

Numerical computations describe the cultivation of MDCK cells in a half-filled 2 L size cellbag, which was rocked with an angle of 7° and a speed of 15 rpm. The cell culture was started with an initial volumetric cell number of 2×10^5 cells/mL with 2 g/L MCs (Genzel et al., 2006). The three-dimensional simulations took into account the exact geometry of the cellbag, obtained during standard operation by a laser measurement technique (Fig. 7.3).

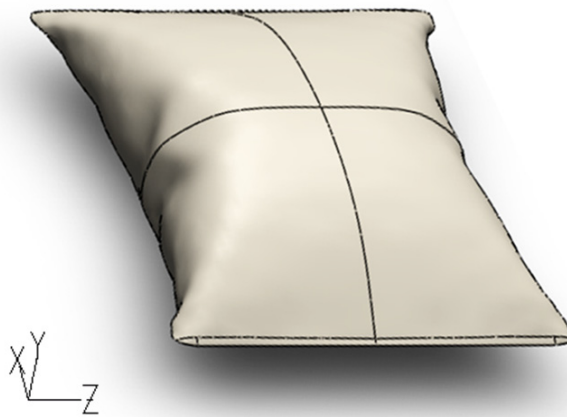


Fig. 7.3. Geometry of the 2 L cellbag considered in the three-dimensional CFD simulations.

All simulations were performed using the industrial CFD code ANSYS-FLUENT[®] 6.3. In order to correctly describe the free liquid surface in an unsteady manner, the three-dimensional calculations were extended with the Volume of Fluid (VOF) method, leading to even higher computational costs. All flow conditions found by CFD have been validated quantitatively concerning liquid surface height, flow velocity and shear stress by comparison with experimental data, as described in Öncül et al. (2010). Hence, three-dimensional simulations in the present study rely on realistic flow conditions.

The kinetic model and PBM equations were implemented in the CFD code via in-house built user-defined scalars (UDS) and functions (UDF).

7.4.1 MC population

The MC population was not described at the level of each individual particle, and the following assumptions were made to facilitate simulations. First, the inert MCs were assumed to be monodisperse in size (about 190 μm in diameter). This is justified by the comparatively very narrow size distribution given by the manufacturer. Second, it was assumed that MCs do not aggregate. This is confirmed by visual observations towards the end of cultivation showing less than 1% aggregates, occurring only through isolated cell bridges formed between two MCs. Third, the buoyancy effect on the MCs was ignored since the difference between the densities of the medium and the MCs is quite low ($< 3\%$). Finally, a perfect homogenization of the MCs was assumed as previous studies confirmed a homogeneous spatial distribution of the MCs in the bag. In fact, the level of homogeneity obtained for the MCs was higher than 97% within 180 s after starting the rocking movement in a 3D CFD simulation. In Fig. 7.4, the evolution of the MC distribution with time, starting from MCs initially deposited near the bottom of the reactor, is shown as obtained numerically by the standard method of moments (SMOM) (Hulburt and Katz, 1964). As addressed above, experimental observations using colored MCs confirmed the fast homogenization of the microcarriers.

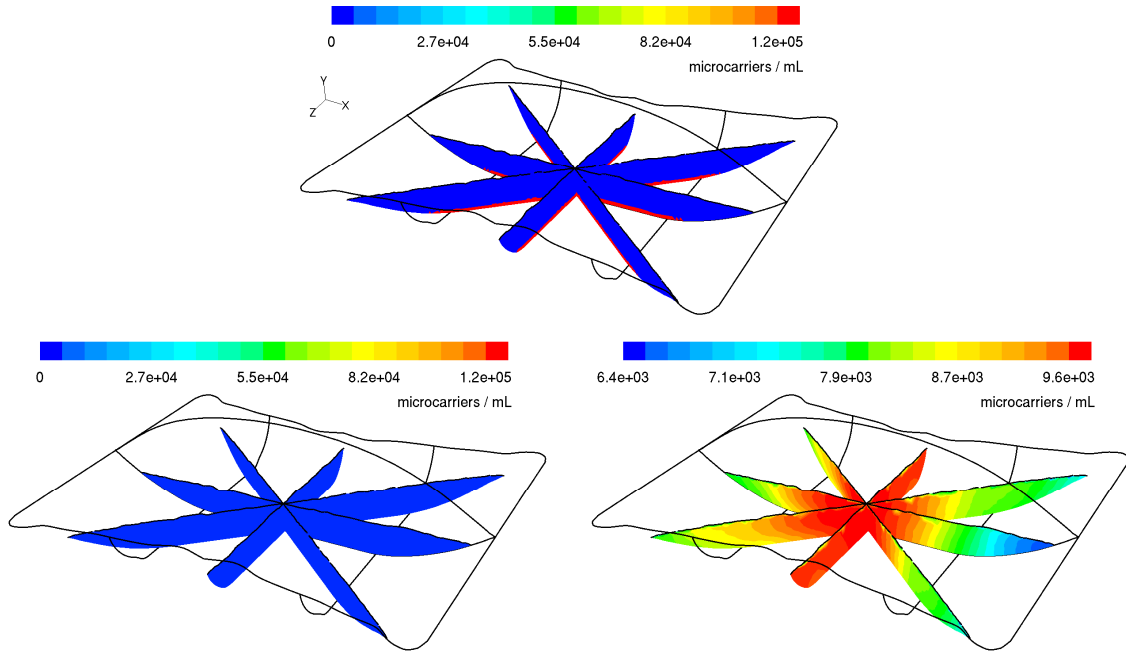


Fig. 7.4. Homogenization of the MC distribution induced by the unsteady flow movement in the 2 L cellbag. The MCs are initially ($t = 0$) all located at the bottom of the bag (top image). The distribution of the MCs after 15 rocking cycles ($t \sim 60$ s) of mixing process is shown with fixed color map (bottom left) and with min/max adapted color map (bottom right), as obtained by SMOM coupled with CFD.

Considering all these assumptions, it was finally not necessary to define the MC population separately and to couple it with the external coordinates (unsteady flow transport) for this simplified numerical approach. In the reduced model, the MC distribution was hence only described with its mean size (diameter, fixed internal coordinate) and its mean spatial concentration (fixed external coordinate) for all simulations. It therefore does not appear as a real population. Nevertheless, the developed numerical model could be extended to take fully into account the additional MC population, if required for further applications.

7.4.2 PBM for animal cells

The evolution of animal cells in suspension and on MCs was defined via two separate populations with interaction terms (two-population balance approach). All cells in suspension were treated as a single population with an additional internal coordinate quantifying the percentage of viable vs. dead cells. In this manner, it is still possible to analyze in detail all three cell families with only two populations.

The concerned cell classes and their corresponding source terms given in Eqs. (7.1)-(7.4) were implemented in the CFD code. Hence, the cell populations interact with the unsteady free-surface flow found in the reactor during a three-dimensional, time-dependent simulation.

7.4.3 Three-dimensional simulation of cultivation

In a first stage, a three-dimensional computation was initiated describing cell growth relying on the full 3D, unsteady flow conditions in a fully coupled manner. However, the complexity of the three-dimensional numerical configuration employing the VOF method and the additional UDS/UDF describing the populations resulted finally in an extremely high computational burden. Employing eight computing cores in parallel, one rocking cycle was simulated in about 3 hours of user-waiting time. While interesting to follow the very first steps of the cultivation process and to check model

implementation, this “brute force” approach could not be used to cover the full cultivation time (this would require about 30 years of simulation using present resources). In order to compare simulation results for cell concentration with the first measurement point (at $t = 1$ h), 4 months of computation time would be required. Consequently, the simulation was stopped after just a few minutes of physical cultivation time, after making sure that all models describing flow, cell and MC populations are working as expected. Eventually, further model reduction was necessary to simulate the complete cultivation process. For this purpose, the conditions found in the three-dimensional bag were considered to be homogeneous as explained next. Nevertheless, the shear stress level found during 3D CFD simulations is still taken into account in the reduced model and can therefore influence cell development and viability.

7.4.4 Zero-dimensional simulation of cultivation

As justified previously, zero-dimensional simulations were performed assuming a spatially homogeneous distribution for MCs. In addition, the distribution of all animal cells was assumed to be homogeneous as well. Cells attached to the MCs are expected to be homogeneously distributed, following the MC distribution. Suspension cells have an extremely low Stokes number (about 0.001), and therefore completely follow the flow in the bag. This results again in a homogeneous distribution. As a consequence, zero-dimensional time-dependent computations appeared suitable for all populations. Such computations on a standard PC yielded a complete solution for the whole cultivation period within a few minutes.

One essential impact of the actual flow conditions on the cultivation process comes from the shear stress. Excessively high values would lead to cell death while high values may prevent cell attachment, inhibit cell growth or induce cell detachment. For this reason, it appeared necessary to include shear stress in the reduced model. In the present study, only the maximum shear stress found in the cellbag was implemented. Since experimental measurements could only be carried out for a limited number of locations, it was not possible to obtain the global peak value via experiments (Kalmbach et al., 2010). On the other hand, a companion numerical investigation was able to describe in a quantitative manner all conditions found in the bioreactor, including shear stress (Öncül et al., 2010). Such simulations were performed employing the numerical methods described previously for several rocking cycles, until periodic flow conditions were achieved. According to the numerical results based on the final periodic flow, maximum shear stress value was 0.2 Pa and 0.5 Pa in the liquid and at the bottom bag wall, respectively (Fig. 7.5). Obviously, the shear stress varied with time and with position within the cellbag. In a first attempt to take into account the influence of shear stress, the spatial variations have been neglected (homogeneous assumptions, all cells are exposed to the same shear stress at the same time). Furthermore, due to the fact that the duration of one rocking cycle (around 4 s) is negligible compared to the cultivation time-scale (around 4 days) and considering the further response time of cells, the time variation of shear stress during one cycle (Fig. 7.5) was neglected as well. Finally, in the reduced model, only the peak shear stress value listed above (0.5 Pa) was taken into account, possibly impacting cell growth, attachment/detachment and viability by increasing accordingly death and detachment rate and reducing growth and attachment rates as a function of the shear stress value. In order to quantify this impact, critical shear stress values obtained from corresponding experiments were then needed.

To our knowledge, there is no information available in literature concerning critical shear stress values for adherent MDCK cells. However, for human diploid fibroblasts (FS-4) Croughan and Wang (1991) reported a critical shear stress level of about 0.7 Pa. While further experiments would be required for adherent MDCK cells, this suggests that the maximum shear stress found in the Wave Bioreactor® (0.5 Pa) was below known critical level under the cultivation conditions investigated. Therefore, even if the reduced model could indeed take into account the influence of peak shear stress on cell development, this part of the numerical model was not active in the results described afterwards, since the observed peak shear stress was below critical shear stress (assumed as 0.7 Pa). This shear stress model could nevertheless easily be activated in future studies if quantitative details are known concerning shear stress impact on MDCK cells.

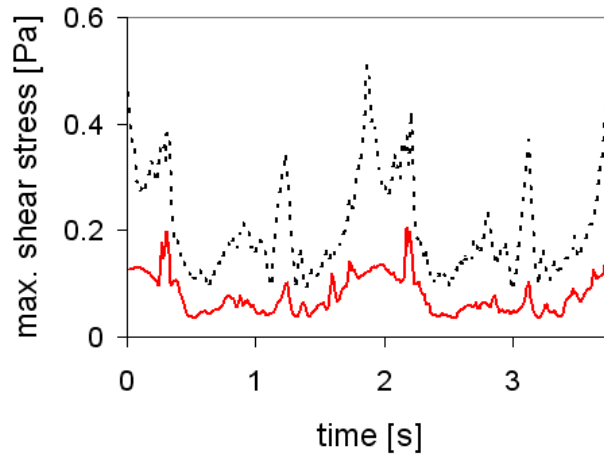


Fig. 7.5. Profiles for the maximum shear stress for one period according to the numerical results in the liquid (solid line) and at the bottom wall (dotted line) of the 2 L cellbag.

7.4.5 Optimization of model parameters for cell kinetics in the Wave Bioreactor[®]

As explained previously, the kinetic parameters for adherent MDCK cells have been estimated experimentally in stirred tank bioreactors and are associated with comparatively large uncertainties, as usual for most bioreactors (Table 7.1). In order to describe the time course of cell populations in a Wave Bioreactor[®], it was therefore necessary to check and possibly refit the kinetic parameters again for such different conditions. The objective here was to obtain the more accurate numerical prediction for the really considered cultivation conditions by comparison with experimental data. For this purpose, zero-dimensional numerical computations delivering the time course of cell populations appeared to be sufficient.

As cell concentrations differ by more than two orders of magnitude during the cultivation process an absolute comparison of errors would be misleading. Therefore, simulated and measured values were compared in this study using logarithmic scales.

The optimization target was to find the best possible set of parameters as appearing in the differential equation system (Eqs. 7.1-7.4) and fitting the measurement results as close as possible (see later Fig. 7.7). The time-dependent computational results representing 4 days of cultivation process were saved at all N measurement points in the experiments. The comparison between simulation and experiments was then computed according to the following formula:

$$\sum_{i=1}^N \left| \log \left(\frac{M_i}{S_i} \right) \right| \rightarrow \min \quad (7.5)$$

where S_i denotes the simulated data, M_i represents the measured values and N is the number of measurement points. The absolute values of the logarithm was necessary to prevent negative values for $M_i < S_i$. The S_i and M_i values were always strictly positive.

The absolute differences between the three cell concentrations obtained by the simulation (i.e., X_{MC} , X_{sus} and X_d) and by measurements were considered as three separate objective functions for the optimization. The aim was to minimize these objective functions simultaneously in order to match as well as possible the measured values. The function given by Eq. (7.5) must be minimized for all three populations simultaneously (multi-objective optimization).

This multi-objective problem finally involved the five parameters (k_{at} , k_{det} , k_d , k_{lys} , μ_{max}) of Table 7.1 as degrees of freedom for the optimization. Considering that the cultivation conditions were still relatively similar in an STR and a Wave Bioreactor[®], all parameters were allowed to vary freely in a

domain limited by their mean value plus/minus standard deviation as measured in the STR (Table 7.1; Möhler et al., 2008), but must at the same time remain strictly positive.

In order to minimize simultaneously all three objective functions, the Genetic Algorithm proposed by Fonseca and Fleming (1993) was employed to determine the optimal set for the considered biological process. The interested reader may find further details concerning the optimization procedure in Thévenin and Janiga (2008). 20 generations involving 20 individuals were computed, yielding more than 200 zero-dimensional simulations. The full optimization procedure took less than one day on a standard PC.

A difficulty was the parallel representation of the results with all degrees of freedom (parameters that should be optimized) and objective functions, yielding an eight-dimensional space. Two-dimensional scatter-plots would be more useful to visualize the correlations between two variables. Fig. 7.6 illustrates all possible combinations of the quantities taken into account in the optimization. These scatter-plots can be considered as the projections of the eight-dimensional space onto two-dimensional spaces. Due to symmetry, scatter-plots are only shown in the upper half of the scatter-plot matrix. On the lower half, the value of the correlation between the corresponding variables is shown. In the main diagonal of the scatter-plot matrix, the probability of the values is displayed by histograms. In this manner, dominating correlations can be clearly identified. Two scatter-plots indicated a particularly strong correlation. The value of k_{lys} determined almost completely the result for X_d (correlation 93%). Furthermore, the value of k_{at} governed to a large extent the result for X_{sus} (correlation 81%). No further clear correlation could be observed, illustrating the complexity of the coupled problem.

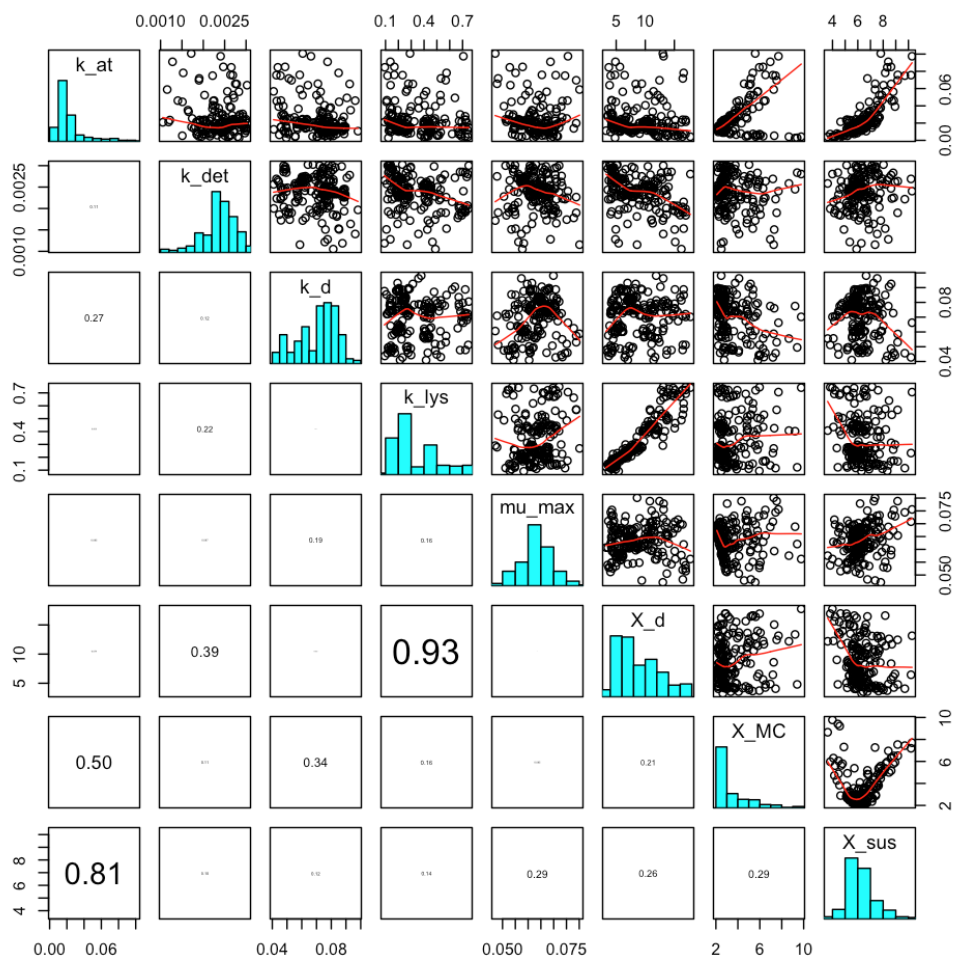


Fig. 7.6. Scatter-plot matrix showing all correlations between the five degrees of freedom and the three objective functions.

7.5 Results and discussion

7.5.1 Evolution of cell concentrations

In a first step, the profiles of all cell concentrations as a function of time obtained using the mean values of the specific kinetic rates measured in an STR (mean values in Table 7.1) are shown in Fig. 7.7 in comparison to the experimental findings. As can be seen, a satisfactory agreement for the cell concentration on MCs (X_{MC}) was already obtained with the standard parameter set, demonstrating that the conditions in the STR were not fundamentally different from those found in the Wave Bioreactor[®]. The final cell yield on MCs (2.8×10^6 cells/mL) was almost successfully predicted by this analysis. On the other hand, although the general agreement of the numerical results for viable cell concentration in suspension was acceptable by comparison to the measured values, the concentration of dead cells was strongly under-predicted. As a whole, the mean values of the kinetic rates used in the simulation did not deliver very accurate results for all cell classes at all times. Furthermore, it must be kept in mind that the left scale in Fig. 7.7 is logarithmic and therefore artificially reduced visible discrepancies between the results. Again, these differences are not a surprise since the kinetic parameters measured in a stirred tank bioreactor were employed here for a different system, the Wave Bioreactor[®].

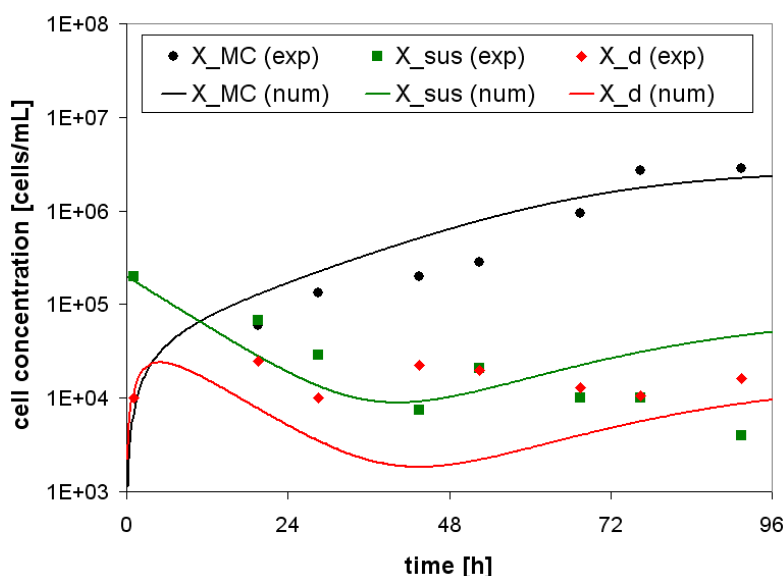


Fig. 7.7. Evolution of cells on microcarriers (black) and in suspension (green for viable, red for dead) according to zero-dimensional simulation using the mean kinetic rates in Table 7.1 (measured in an STR; lines) compared with experimental data in the Wave Bioreactor[®] (symbols).

7.5.2 Results of parameter optimization

According to the classical Pareto rule (Thévenin and Janiga, 2008) the non-dominated solutions were extracted from the optimization and represented the set of all optimal solutions (so-called Pareto boundary). In the present problem, 34 optimal solutions were obtained as shown in a three-dimensional scatter plot representing the three objective functions in Fig. 7.8. Due to the three simultaneous objectives, there is not a single solution better than all others. For instance, the best agreement for dead cells in solutions does not lead to the best agreement for the attached cells. Therefore, a compromise has to be found based on additional user input. Considering that the attached cell population X_{MC} is the most important one for the process considered, the best solution for X_{MC} belonging to the Pareto boundary was finally retained. The process description obtained with the optimal set of parameters (Fig. 7.9) shows as expected a clear improvement compared to the original

results employing the mean parameters from Möhler et al. (2008) based on measurements in an STR (Fig. 7.7).

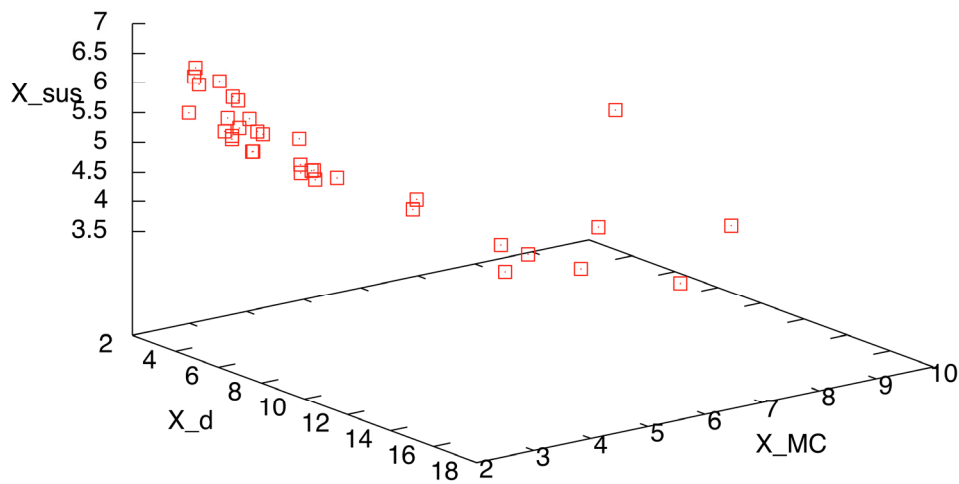


Fig. 7.8. Three-dimensional scatter plot of objective functions for all optimal results (Pareto boundary).

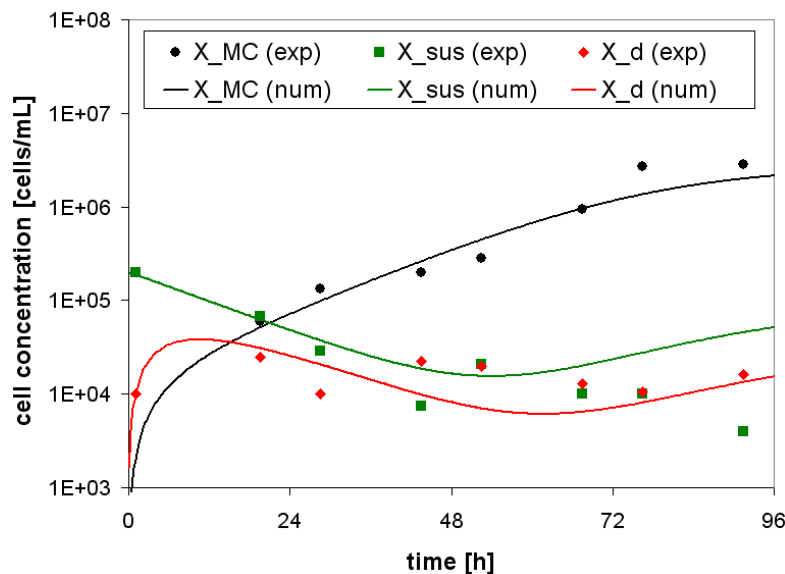


Fig. 7.9. Evolution of cells on microcarriers (black) and in suspension (green for viable, red for dead) according to zero-dimensional simulation using the retained optimal set of parameters (lines) compared with experimental data (symbols) in the Wave Bioreactor®.

The specific kinetic rates corresponding to the retained optimal solution for the conditions found in a Wave Bioreactor® are finally given in Table 7.2. This selected solution described the cultivation system in a very satisfactory manner compared with the measured values (see again Fig. 7.9). The numerical results are in very good agreement for all three populations, even for the concentration of dead cells in the suspension. A slight over-prediction of the viable cells in suspension at the end of the cultivation process remained, while the adherent cell population was very well predicted. Since this quantity is the most interesting information for practical purposes, the optimized kinetic parameters listed in Table 7.2 are recommended to represent cultivation of MDCK cells in Wave Bioreactor® in a realistic manner.

Table 7.2. Specific rates corresponding to the retained optimal solution (all values in h^{-1}). Relative changes with respect to the original values measured in an STR (see Table 7.1) are also given.

| Parameter | Optimized value for Wave Bioreactor [®] | Relative change compared to measurements in STR (%) |
|---|--|---|
| Specific attachment rate, k_{at} | 0.009717 | -71.3 |
| Specific detachment rate, k_{det} | 0.001867 | -8.0 |
| Specific death rate, k_d | 0.05067 | -27.6 |
| Specific lysis rate, k_{lys} | 0.1410 | -59.7 |
| Maximum specific growth rate, μ_{max} | 0.06948 | +8.2 |

Compared to the kinetic parameters measured experimentally in the STR (Möhler et al., 2008), the largest parameter modification coming out of the optimization in the Wave Bioreactor[®] was a considerable reduction of the attachment rate k_{at} (Table 7.2). This could possibly be an indirect effect of flow shear stress or of differences in the cultivation conditions, hindering the attachment process on the MCs in the Wave Bioreactor[®], while being too low to directly induce cell death or cell detachment. Note, however, that some of these differences are probably simply a result of differing model assumptions, since the optimized values (second column of Table 7.2) were obtained by neglecting all substrate limitations or inhibitor accumulations, while those aspects were taken into account when measuring experimentally the kinetic rates in an STR (Möhler et al., 2008).

7.6 Conclusions and remarks

In this work, numerical investigations for the cultivation of MDCK cells adherent on microcarriers in a 2 L size Wave Bioreactor[®] were presented. Since a three-dimensional CFD simulation fully coupled with the time-dependent evolution of the populations was definitely unfeasible due to the resulting numerical costs, a significant model reduction was considered. The numerical computations considered a zero-dimensional case in space, assuming homogeneous conditions for MC population as well as for all cell populations in the cellbag. Only time evolutions were finally considered. The influence of shear stress on cell growth, detachment and death has also been implemented in the computational model in principle. However, the peak shear stress found in the present bioreactor was below critical values from the literature for similar animal cells. Since data for MDCK cells could not be found, this shear stress sub-model was hence not activated in the present work.

The applied mathematical model allowed a simulation of the whole cultivation process in the reactor including the initial lag phase. The specific kinetic rates were estimated based on experimental data obtained in a stirred tank bioreactor assuming first-order reaction kinetics. All model equations were implemented in the CFD code via UDS and UDF.

As expected, the initial numerical results obtained using the mean values for the specific kinetic rates measured in a different bioreactor were relatively far from the measurement points. Therefore, a parameter optimization was performed around the mean parameter value, taking into account the measured standard deviations, in order to determine a parameter set suitable to describe cultivation conditions in a Wave Bioreactor[®]. The finally retained optimal solution allowed a very good agreement between numerical prediction and measurements for the really considered cultivation conditions.

At this point, it would be easily possible to perform systematic studies while varying for instance initial cell concentrations and/or MC concentrations. Moreover, similar studies could also be carried out for the 20 L size cellbag, for which numerical investigations of the flow field are already available (Öncül et al., 2010).

Nevertheless, the strong model reduction considered in the present work might have a strong impact on the obtained accuracy. Since fully coupled three-dimensional simulations will clearly remain beyond reach for some years, two issues will be particularly considered in future studies:

1. The influence of shear stress on MDCK cell growth, attachment and detachment must be quantified experimentally in a much more detailed manner. In this way, a more realistic coupling between flow and cultivation results can be implemented.
2. A more accurate coupling would be obtained by freezing the periodic flow solution and integrating the population equations on top of this frozen flow. Such a procedure requires many tricky algorithm transformations for the present problem involving a moving, free surface boundary. It should however be possible in a near future.

References of Chapter 7

- Bezzo, F., Macchietto, S., Pantelides, C.C. (2003). General hybrid multizonal/CFD approach for bioreactor modelling. *AIChE J.*, 49, 2133-2148.
- Croughan, M.S., Wang, D.I. (1991). Hydrodynamic effects on animal cells in microcarrier bioreactors. *Biotechnology*, 17, 213-249.
- Eibl, R., Eibl, D. (2006). Design and use of the wave bioreactor for plant cell culture. *Plant Tissue Culture Engineering*, (Dutta Gupta, S., and Ibaraki, Y., Eds.), Dordrecht: Springer, 203-227.
- Fonseca, C.M., Fleming, P.J. Genetic algorithms for multiobjective optimization: formulation, discussion and generalization, in: *Genetic Algorithms: Proceedings of the Fifth International Conference*, San Mateo, California, 1993, pp. 416-423.
- Freshney, R.I. (1994). *Culture of Animal Cells: A Manual of Basic Technique*, Third Edition, New York: Wiley-Liss, Inc.
- Genzel, Y., Olmer, R.M., Schäfer, B., Reichl, U. (2006). Wave microcarrier cultivation of MDCK cells for influenza virus production in serum containing and serum-free media. *Vaccine*, 24, 6074-6087.
- Genzel, Y., Reichl, U. (2007). Vaccine production – state of the art and future needs in upstream processing. *Animal Cell Biotechnology – Methods and Protocols*, (Pörtner, R., Ed.), Totowa: HUMANA Press Inc., 457-473.
- Hulburt, H.M., Katz, S. (1964). Some problems in particle technology, a statistical mechanical formulation. *Chem. Eng. Sci.*, 19, 555-574.
- Kalmbach, A., Bordás, R., Öncül, A.A., Thévenin, D., Genzel, Y., Reichl, U. Experimental characterization of flow conditions in 2 L and 20 L bioreactors with wave-induced motion. *Biotechnol. Prog.*, in press, 2010.
- Lapin, A., Schmid, J., Reuss, M. (2006). Modeling the dynamics of *E. coli* populations in the three-dimensional turbulent field of a stirred-tank bioreactor – A structured–segregated approach. *Chem. Eng. Sci.*, 61, 4783-4797.
- Mikola, M., Seto, J., Amanullah, A. (2007). Evaluation of a novel Wave Bioreactor[®] cellbag for aerobic yeast cultivation. *Bioprocess Biosyst. Eng.*, 30, 231-241.
- Möhler, L., Bock, A., Reichl, U. (2008). Segregated mathematical model for growth of anchorage-dependent MDCK cells in microcarrier culture. *Biotechnol. Prog.*, 24, 110-119.
- Öncül, A.A., Kalmbach, A., Genzel, Y., Reichl, U., Thévenin, D. (2010). Characterization of flow conditions in 2 L and 20 L Wave Bioreactors[®] using Computational Fluid Dynamics. *Biotechnol. Prog.*, 26, 101-110.
- Palazón, J., Mallol, A., Eibl, R., Lettenbauer, C., Cusidó, R.M., Piñol, M.T. (2003). Growth and ginsenoside production in hairy root cultures of *Panax ginseng* using a novel bioreactor. *Planta Med.*, 69, 344-349.
- Schmalzriedt, S., Jenne, M., Mauch, K., Reuss, M. (2003). Integration of physiology and fluid dynamics. *Advances in Biochemical Engineering/Biotechnology*, (von Stockar, U., and van der Wielen, L.A.M., Eds.), Berlin/Heidelberg: Springer Verlag, 80, 19-68.
- Singh, V. (1999). Disposable bioreactor for cell culture using wave-induced agitation. *Cytotechnology*, 30, 149-158.
- Singh, V. (2001). Method for culturing cells using wave-induced agitation. *United States Patent*, Patent No. US 6,190,913 B1.
- Spier, R.E. (Ed.) (2000). *Encyclopedia of Cell Technology*, New York: Wiley, 183-278.
- Thévenin, D., Janiga, G. (Eds.) (2000). *Optimization and Computational Fluid Dynamics*. Berlin: Springer.
- Zhang, H., Zhang, K., Fan, S. (2009). CFD simulation coupled with population balance equations for aerated stirred bioreactors. *Eng. Life Sci.*, 9, 421-430.

Chapter 8

Conclusions and outlook

In the present work, CFD simulations were performed to investigate particle populations in homogeneous as well as inhomogeneous flows for various applications in chemical and biochemical engineering. For this purpose, various PBMs (depending on the application) were coupled with the CFD code and the resulting numerical tool was employed using increasingly complex numerical methods and models (such as Eulerian method, adaptive time-stepping method, turbulence model, sliding mesh model, etc.). Furthermore, various hydrodynamic and initial conditions were examined during the computations. Moreover, to check the validity of the employed numerical tool, either corresponding experimental data or analytical solutions were considered.

In the initial part of the work, bulk precipitation (i.e., reactive crystallization) of BaSO_4 in a coaxial pipe mixer was numerically investigated for various mixing-controlled hydrodynamic conditions as well as various reactant concentrations. For this purpose, the kinetic model was coupled with an appropriate PBM (here SMOM) using the first four moments in order to compute the evolution of the BaSO_4 crystal population. All model equations and source terms were then implemented in the CFD code via in-house built supplementary UDS and UDF in an Eulerian framework. Moreover, this initial study provided the opportunity to prove the reliability of the numerical results obtained from the CFD/PBM tool by the validation of time-dependent zero-dimensional computations through a corresponding semi-analytical solution. Hence, the basis of the PBM applications in CFD computations was constituted during this initial study, to be used again in all further studies. The successful reconstruction of the CSD of the resulting BaSO_4 population assuming a prescribed shape (such as Gaussian function or β -function) was another interesting result of this study.

After completing successfully the investigations on the CFD modelling of reactive crystallization coupled with PBM, similar coupled numerical analyses on the preferential crystallization of threonine crystals were carried out. However, CFD was coupled in this case with a two-population balance approach (each population representing a threonine enantiomer), based again on SMOM. The obtained numerical results were validated through the available experimental data. The same two-population balance approach was used later for the simulation of the cultivation of animal cells. Another important result of this study was the simulation of a process in a three-dimensional CSBR geometry applying a moving mesh technique (SMM) to represent the impeller motion. Frozen flow conditions were applied in order to reduce the high computational effort resulting from the complex three-dimensional modelling without losing any information on the turbulent flow field. All the experiences gained during this study were useful for further studies.

Afterwards, numerical computations were performed to investigate the microemulsion precipitation of BaSO_4 in a semi-batch reactor. A reduced PBM was employed for this configuration to obtain an efficient numerical solution. This reduced PBM was first validated up to an acceptable degree with the help of experimental data via a zero-dimensional (spatially homogeneous) analysis. Thereafter, three-dimensional inhomogeneous simulations were performed for a more realistic investigation by embedding the reduced PBM formulation into the CFD code via in-house built supplementary UDS and UDF, as done in the previous studies. The motion of the impeller was again defined via moving mesh techniques (MRF and SMM). Additionally, building on top of the numerical experiences gained during the investigation of preferential crystallization, frozen flow conditions were employed in order to reduce the computational effort. The employed CFD/reduced PBM tool yielded reasonable results in acceptable computing times. The interest of model reduction was demonstrated during this study.

In the next part of the work, investigations were made on liquid flows involving animal cell cultivation in a bioreactor. The aim of these investigations was to quantify the influence of flow conditions on cell viability so that a better understanding of cell growth and cell damage would become possible. The reactor used for the considered biochemical process was a disposable bioreactor with wave-induced motion (commercial name: Wave Bioreactor[®]) in 2 L and 20 L sizes, which has several advantages and has led to markedly improved results for some biotechnological applications. Firstly, experiments were carried out in order to characterize the flow conditions within the Wave Bioreactors[®] by measuring the most important flow parameters (liquid surface level, liquid velocity, liquid and wall shear stress). By this way, later CFD simulations describing the flow conditions within the concerned cellbags could be validated by comparison with experiments. The measurements showed in particular a low level of shear stress in the Wave Bioreactors[®] compared to classical bioreactors like stirred tanks, indicating favorable hydrodynamic conditions for cell cultivation.

In the next step, CFD simulations were performed in order to characterize numerically the flow conditions in the Wave Bioreactors[®]. One important feature of this study was that the unsteady, three-dimensional computations employed the VOF method, an Eulerian multiphase model which is able to predict correctly the free liquid surface. By this way, the interface between the liquid and gas phases in the used cellbags (that were partially filled with liquid) could be accurately described. Another important aspect of this study was the realistic reconstruction of the numerical geometry on the basis of the scanned bioreactor surfaces (under operating conditions) with the help of a laser measuring technique. In this manner, a direct comparison of the CFD predictions with the experimental data became possible. The most important conclusion of this study is that the CFD predictions for the flow conditions in the concerned cellbags were successfully validated, since the agreement between the obtained numerical results and the experimental findings was satisfactory. Another conclusion is that the low level of shear stress (well below known threshold values leading to damage of animal cells) was confirmed by the computations. Furthermore, it was shown that the obtained flows (under the considered operating conditions) stayed in the laminar regime, confirming gentle mixing conditions, which would result in lower cell damage and consequently higher cell viability.

Finally, simulations of animal cell cultivation in a microcarrier (MC) system were carried out. These simulations employed an appropriately reduced PBM based on a two-population balance approach with mutual interaction. For this purpose, the corresponding experience from previous investigations was important. The two populations described animal cells in suspension and animal cells on MCs. The cell population in suspension was represented with an additional internal property; viable or dead. According to some reasonable assumptions (MCs were monodisperse in size, they are spatially homogeneously distributed in the liquid, etc.), it was not necessary to define the MC population separately. A realistic three-dimensional CFD simulation carried out to analyze the spatial distribution of the MCs confirmed a fast homogenization. For this purpose, SMOM was employed to describe the MC population, using once again the numerical experiences from previous studies. Due to the complexity of the three-dimensional configuration, the simulations could finally only be performed for a zero-dimensional case, but considering the flow conditions (maximum shear stress values) obtained from the three-dimensional CFD computations in the previous steps. However, since the obtained peak values of shear stress were below critical values from the literature for similar animal cells, the corresponding shear stress sub-model was inactive in the present work. A parameter optimization was carried out to obtain a more satisfactory agreement with the experimental data for Wave Bioreactor[®], taking into account the measured standard deviations of the mean values for the relevant kinetic rates measured in a different bioreactor. The retained optimal solution allowed a considerably better agreement between numerical predictions and measurements for the considered cultivation conditions.

As a whole, the predictions of the developed numerical procedure were generally found to be satisfactory and highly useful to understand the coupled processes. Numerous journal articles and conference contributions appeared in the literature in relation with these different studies (see Appendix C). Only the most relevant ones were discussed in this thesis.

From a numerical point of view, more complex simulations could be carried out in the future. It would be in particular possible to consider further physical processes (e.g. aggregation of MCs and animal cells) as well as different hydrodynamic conditions (e.g. various rocking rates, angles and

strategies for Wave Bioreactor[®]). Moreover, a more accurate coupling would be obtained by freezing the periodic flow solution and integrating the population equations on top of this frozen flow. By this way, more accurate solutions could be obtained, opening the door for process optimization and scale-up strategies based on corresponding simulations.

Appendices

A Semi-analytical solution for the zero-dimensional stoichiometric case

The specific crystal growth rate depends from the supersaturation ratio through two terms: m_2 and G . At the same time, the supersaturation ratio is dependent on reactant concentrations (Eq. (2.7)). It is therefore possible to express the specific crystal growth rate (Eq. (2.3)) in terms of concentrations, in order to perform an analytical analysis of the precipitation process. For this purpose, following procedure is applied:

$$\frac{dC}{dt} = -Km_2(S-1)^2, \quad \text{where } K = 3k_gk_v \frac{\rho_{BaSO_4}}{W_{BaSO_4}}. \quad (\text{A.1})$$

In the case of stoichiometric initial concentrations of Ba^{2+} and SO_4^{2-} the supersaturation ratio given in Eq. (2.7) simplifies to

$$S = \gamma \left(\frac{CC}{K_{sp}} \right)^{0.5} = \alpha C \quad \text{for } C_{Ba} = C_{SO_4} = C, \quad (\text{A.2})$$

$$\text{where } \alpha = \frac{\gamma}{\sqrt{K_{sp}}}.$$

Note that the further developments do not require the (often used) hypothesis of a unity activity coefficient ($\gamma=1$). Any constant value can be considered. Defining the first three moment source terms as a function of C according to Eq. (2.4):

$$\frac{dm_0}{dt} = B \exp \left[-\frac{A}{\ln^2(\alpha C)} \right], \quad (\text{A.3})$$

$$\frac{dm_1}{dt} = m_0 k_g (\alpha C - 1)^2, \quad (\text{A.4})$$

$$\frac{dm_2}{dt} = 2m_1 k_g (\alpha C - 1)^2. \quad (\text{A.5})$$

Rewriting Eq. (A.1) in terms of C :

$$\frac{dC}{dt} = -Km_2(\alpha C - 1)^2, \quad (\text{A.6})$$

$$m_2 = -\frac{1}{K(\alpha C - 1)^2} \frac{dC}{dt}. \quad (\text{A.7})$$

Taking the derivative of Eq. (A.6) with respect to time:

$$\frac{d^2C}{dt^2} = -K(\alpha C - 1)^2 \frac{dm_2}{dt} - 2\alpha K m_2 (\alpha C - 1) \frac{dC}{dt}. \quad (\text{A.8})$$

Substituting Eqs. (A.5) and (A.7) into (A.8):

$$\frac{d^2C}{dt^2} = -2Kk_g (\alpha C - 1)^4 m_1 + \frac{2\alpha}{\alpha C - 1} \left(\frac{dC}{dt} \right)^2. \quad (\text{A.9})$$

Taking the derivative of Eq. (A.9) with respect to time:

$$\frac{d^3C}{dt^3} = -2Kk_g (\alpha C - 1)^4 \frac{dm_1}{dt} - 8\alpha Kk_g (\alpha C - 1)^3 m_1 \frac{dC}{dt} + \frac{4\alpha}{\alpha C - 1} \frac{dC}{dt} \frac{d^2C}{dt^2} - \frac{2\alpha^2}{(\alpha C - 1)^2} \left(\frac{dC}{dt} \right)^3. \quad (\text{A.10})$$

From Eq. (A.9):

$$m_1 = -\frac{1}{2Kk_g (\alpha C - 1)^4} \frac{d^2C}{dt^2} + \frac{\alpha}{Kk_g (\alpha C - 1)^5} \left(\frac{dC}{dt} \right)^2. \quad (\text{A.11})$$

Substituting Eqs. (A.4) and (A.11) into (A.9):

$$\begin{aligned} \frac{d^3C}{dt^3} = & -2Kk_g^2 (\alpha C - 1)^6 m_0 + \frac{4\alpha}{\alpha C - 1} \frac{dC}{dt} \frac{d^2C}{dt^2} - \frac{8\alpha^2}{(\alpha C - 1)^2} \left(\frac{dC}{dt} \right)^3 \\ & + \frac{4\alpha}{\alpha C - 1} \frac{dC}{dt} \frac{d^2C}{dt^2} - \frac{2\alpha^2}{(\alpha C - 1)^2} \left(\frac{dC}{dt} \right)^3 \end{aligned} \quad (\text{A.12})$$

$$\frac{d^3C}{dt^3} = -2Kk_g^2 (\alpha C - 1)^6 m_0 + \frac{8\alpha}{\alpha C - 1} \frac{dC}{dt} \frac{d^2C}{dt^2} - \frac{10\alpha^2}{(\alpha C - 1)^2} \left(\frac{dC}{dt} \right)^3. \quad (\text{A.13})$$

Taking the derivative of Eq. (A.13) with respect to time:

$$\begin{aligned} \frac{d^4C}{dt^4} = & -2Kk_g^2 (\alpha C - 1)^6 \frac{dm_0}{dt} - 12\alpha Kk_g^2 (\alpha C - 1)^5 \frac{dC}{dt} m_0 + \frac{8\alpha}{\alpha C - 1} \left(\frac{d^2C}{dt^2} \right)^2 + \frac{8\alpha}{\alpha C - 1} \frac{dC}{dt} \frac{d^3C}{dt^3} \\ & - \frac{8\alpha^2}{(\alpha C - 1)^2} \left(\frac{dC}{dt} \right)^2 \frac{d^2C}{dt^2} - \frac{30\alpha^2}{(\alpha C - 1)^2} \left(\frac{dC}{dt} \right)^2 \frac{d^2C}{dt^2} + \frac{20\alpha^3}{(\alpha C - 1)^3} \left(\frac{dC}{dt} \right)^4 \end{aligned} \quad (\text{A.14})$$

From Eq. (A.13):

$$m_0 = -\frac{1}{2Kk_g^2 (\alpha C - 1)^6} \frac{d^3C}{dt^3} + \frac{4\alpha}{Kk_g^2 (\alpha C - 1)^7} \frac{dC}{dt} \frac{d^2C}{dt^2} - \frac{5\alpha^2}{Kk_g^2 (\alpha C - 1)^8} \left(\frac{dC}{dt} \right)^3. \quad (\text{A.15})$$

Substituting Eqs. (A.3) and (A.13) into (A.14) one finally gets:

$$\begin{aligned} \frac{d^4C}{dt^4} = & -2BKk_g^2(\alpha C - 1)^6 \exp\left[-\frac{A}{\ln^2(\alpha C)}\right] + \frac{14\alpha}{\alpha C - 1} \frac{dC}{dt} \frac{d^3C}{dt^3} \\ & - \frac{86\alpha^2}{(\alpha C - 1)^2} \left(\frac{dC}{dt}\right)^2 \frac{d^2C}{dt^2} + \frac{80\alpha^3}{(\alpha C - 1)^3} \left(\frac{dC}{dt}\right)^4 + \frac{8\alpha}{\alpha C - 1} \left(\frac{d^2C}{dt^2}\right)^2 \end{aligned} \quad (\text{A.16})$$

This ordinary differential equation is still too complex to be solved analytically, in particular due to the exponential term. Nevertheless, a very accurate numerical solution of this fourth-order ordinary differential equation can be readily obtained using available mathematical software. In the present case, Maple[®] is employed to solve this equation. Of course, the change in the values of the constants A and B for different values of the supersaturation ratio (Eq. (2.6)) must be taken into account. The corresponding reactant concentration value at the threshold between both sets of parameters is for example equal to 0.01049 kmol/m³ according to Eq. (2.7) for stoichiometric mixtures and $\gamma = 1$.

B Calculation of the activity coefficient γ according to Bromley's Method

The activity coefficient of the salt 12, γ_{12} , in a multi-component solution is formulated as:

$$\log \gamma_{12} = \frac{-A_\gamma |Z_1 Z_2| \sqrt{I}}{1 + \sqrt{I}} + \frac{|Z_1 Z_2|}{|Z_1| + |Z_2|} \left[\frac{F_1}{|Z_1|} + \frac{F_2}{|Z_2|} \right], \quad (\text{B.1})$$

where A_γ is the Debye-Hückel constant, which is equal to $0.511 \text{ kg}^{1/2}/\text{mol}^{1/2}$ at 25°C , I is the ionic strength of the solution, Z_1 and Z_2 denote the charge numbers on the cation and anion respectively and F_1 and F_2 are functions that are calculated by following equations:

$$F_1 = \dot{B}_{12} \bar{Z}_{12}^2 C_2 + \dot{B}_{14} \bar{Z}_{14}^2 C_4 + \dot{B}_{16} \bar{Z}_{16}^2 C_6 + \dots, \quad (\text{B.2})$$

$$F_2 = \dot{B}_{12} \bar{Z}_{12}^2 C_1 + \dot{B}_{32} \bar{Z}_{32}^2 C_3 + \dot{B}_{52} \bar{Z}_{52}^2 C_5 + \dots, \quad (\text{B.3})$$

Here, it is worth noting that the odd numbers in the subscripts of the above equations denote the cations whereas the even numbers denote the anions in the multi-component solution. Arithmetic average charge numbers (\bar{Z}_{+-}) and the variables, \dot{B}_{+-} , are expressed in the following equations:

$$\bar{Z}_{+-} = \frac{|Z_+| + |Z_-|}{2}, \quad (\text{B.4})$$

$$\dot{B}_{+-} = \frac{(0.06 + 0.6B_{+-})|Z_+ Z_-|}{\left(1 + \frac{1.5}{|Z_+ Z_-|} I\right)^2} + B_{+-}. \quad (\text{B.5})$$

The constant B_{+-} of a salt defined in the above equation is calculated as

$$B_{+-} = B_+ + B_- + \delta_+ \delta_-. \quad (\text{B.6})$$

All the terms in the B_{+-} equation are specific for every ion and the individual values can be obtained in literature (for example in Bromley, 1973, see References of Chapter 2).

Moreover, the ionic strength of the solution can be calculated by

$$I = \frac{\sum C_i Z_i^2}{2}. \quad (\text{B.7})$$

The activity coefficient of BaSO_4 in a solution involving 0.04 M BaCl_2 and $0.04 \text{ M Na}_2\text{SO}_4$ is calculated below as an example. In fact, this mixture can be considered as the initial mixture at the point where two inlet streams meet each other in the coaxial pipe mixer for 0.08 M inlet concentrations. Accordingly, the calculated activity coefficient value is the initial value for the mixture in the pipe in this case. The individual ion values associated with this mixture are listed in Table B.1.

Table B.1. Individual ion values in an aqueous solution at 25°C (Bromley, 1973)

| Cation | B_+ (kg/mol) | δ_+ | Anion | B_- (kg/mol) | δ_- |
|------------------|----------------|------------|--------------------|----------------|------------|
| Na^+ | 0.0000 | 0.028 | Cl^- | 0.0643 | -0.067 |
| Ba^{2+} | 0.0022 | 0.098 | SO_4^{2-} | 0.0000 | -0.400 |

Assigning numbers to each ion:

$$\begin{array}{ll} 1 \rightarrow \text{Ba}^{2+} & 3 \rightarrow \text{Na}^+ \\ 2 \rightarrow \text{SO}_4^{2-} & 4 \rightarrow \text{Cl}^- \end{array}$$

$$|Z_1| = |Z_2| = 2, \quad (\text{B.8})$$

$$|Z_3| = |Z_4| = 1, \quad (\text{B.9})$$

$$I = \frac{(0.04 \times 2^2) + (0.04 \times 2^2) + (0.08 \times 1^2) + (0.04 \times 1^2)}{2} = 0.24 \text{ mol/kg}. \quad (\text{B.10})$$

$$\bar{Z}_{12} = \frac{2+2}{2} = 4; \quad \bar{Z}_{14} = \frac{2+1}{2} = 1.5; \quad \bar{Z}_{32} = \frac{1+2}{2} = 1.5, \quad (\text{B.11})$$

$$B_{12} = 0.0022 + 0 + 0.098 \times (-0.4) = -0.037 \text{ kg/mol}, \quad (\text{B.12})$$

$$B_{14} = 0.0022 + 0.0643 + 0.098 \times (-0.067) = 0.06 \text{ kg/mol}, \quad (\text{B.13})$$

$$B_{32} = 0 + 0 + 0.028 \times (-0.4) = -0.0112 \text{ kg/mol}, \quad (\text{B.14})$$

$$\dot{B}_{12} = \frac{(0.06 + 0.6 \times (-0.037)) \times 4}{\left(1 + \frac{1.5}{4} \times 0.24\right)^2} + (-0.037) = 0.09 \text{ kg/mol}, \quad (\text{B.15})$$

$$\dot{B}_{14} = \frac{(0.06 + 0.6 \times 0.06) \times 2}{\left(1 + \frac{1.5}{2} \times 0.24\right)^2} + 0.06 = 0.198 \text{ kg/mol}, \quad (\text{B.16})$$

$$\dot{B}_{32} = \frac{(0.06 + 0.6 \times (-0.0112)) \times 2}{\left(1 + \frac{1.5}{2} \times 0.24\right)^2} + (-0.0112) = 0.065 \text{ kg/mol}, \quad (\text{B.17})$$

$$F_1 = 0.09 \times 2^2 \times 0.04 + 0.198 \times 1.5^2 \times 0.08 = 0.05, \quad (\text{B.18})$$

$$F_2 = 0.09 \times 2^2 \times 0.04 + 0.065 \times 1.5^2 \times 0.08 = 0.026, \quad (\text{B.19})$$

$$\log \gamma_{12} = \frac{-0.511 \times 4 \times \sqrt{0.24}}{1 + \sqrt{0.24}} + \frac{4}{2+2} \left[\frac{0.05}{2} + \frac{0.026}{2} \right] = -0.634, \quad (\text{B.20})$$

$$\gamma_{12} = 0.23229. \quad (\text{B.21})$$

C List of publications of A.A. Öncül

Journal articles:

- [1] **Öncül, A.A.**, Sundmacher, K., Thévenin, D. Numerical investigation of the influence of the activity coefficient on barium sulphate crystallization. *Chemical Engineering Science*, 60:5395-5405, 2005.
- [2] **Öncül, A.A.**, Elsner, M.P., Thévenin, D., Seidel-Morgenstern, A. Numerische Untersuchung der Kristallisation zur Enantiomerentrennung in komplexen Strömungen. *Chemie Ingenieur Technik*, 77:1040-1041, 2005.
- [3] **Öncül, A.A.**, Sundmacher, K., Seidel-Morgenstern, A., Thévenin, D. Numerical and analytical investigation of barium sulphate crystallization. *Chemical Engineering Science*, 61:652-664, 2006.
- [4] John, V., Angelov, I., **Öncül, A.A.**, Thévenin, D. Techniques for the reconstruction of a distribution from its moments. *Chemical Engineering Science*, 62:2890-2904, 2007.
- [5] Kurt, T., **Öncül, A.A.**, El-Rabii, H., Thévenin, D. Vorhersage der Rußbildung in abgehobenen Diffusionsflammen anhand Momenten-Methoden. *VDI-Berichte*, 1988:325-330, 2007.
- [6] **Öncül, A.A.**, Thévenin, D. Einfluss der Partikelmorphologie auf die numerische Modellierung der BaSO₄-Fällung. *Chemie Ingenieur Technik*, 79:1460, 2007.
- [7] **Öncül, A.A.**, Niemann, B., Sundmacher, K., Thévenin, D. CFD modelling of BaSO₄ precipitation inside microemulsion droplets in a semi-batch reactor. *Chemical Engineering Journal*, 138:498-509, 2008.
- [8] **Öncül, A.A.**, Janiga, G., Thévenin, D. Comparison of various micromixing approaches for computational fluid dynamics simulation of barium sulfate precipitation in tubular reactors. *Industrial and Engineering Chemistry Research*, 48:999-1007, 2009.
- [9] **Öncül, A.A.**, Kalmbach, A., Genzel, Y., Reichl, U., Thévenin, D. Numerische und experimentelle Untersuchung der Fließbedingungen in Wave-Bioreaktoren. *Chemie Ingenieur Technik*, 81:1241, 2009.
- [10] **Öncül, A.A.**, Kalmbach, A., Genzel, Y., Reichl, U., Thévenin, D. Characterization of flow conditions in 2 L and 20 L Wave Bioreactors® using Computational Fluid Dynamics. *Biotechnology Progress*, 26:101-110, 2010.
- [11] **Öncül, A.A.**, Bordás, R., Thévenin, D., Genzel, Y., Reichl, U. CFD-Modellierung der Zellkultivierung in Wave-Bioreaktoren. *Chemie Ingenieur Technik*, 82:1512-1513, 2010.
- [12] Czapla, F., Kail, N., **Öncül, A.A.**, Lorenz, H., Briesen, H., Seidel-Morgenstern, A. Application of a recent FBRM-probe model to quantify preferential crystallization of DL-threonine. *Chemical Engineering Research and Design*, 88:1494-1504, 2010.
- [13] Kalmbach, A., Bordás, R., **Öncül, A.A.**, Thévenin, D., Genzel, Y., Reichl, U. Experimental characterization of flow conditions in 2 L and 20 L bioreactors with wave-induced motion. *Biotechnology Progress*, in press (DOI 10.1002/btpr.516).

Conferences and proceedings:

- [1] **Öncül, A.A.**, Thévenin, D., Elsner, M.P., Seidel-Morgenstern, A. Numerical analysis of the preferential crystallization of enantiomers (Oral). *11th Workshop on Two-phase Flow Predictions*, ISBN 3-86010-767-4, pp. 5.10/1-5.10/15, Merseburg-Halle, Germany, April 5-8, 2005.
- [2] **Öncül, A.A.**, Thévenin, D., Elsner, M.P., Seidel-Morgenstern, A. Numerische Untersuchung der Kristallisation zur Enantiomerentrennung in komplexen Strömungen (Oral). *GVC/DECHEMA Jahrestagungen*, Paper No: V5.02, Wiesbaden, Germany, September 6-8, 2005.

- [3] **Öncül, A.A.**, Thévenin, D., Elsner, M.P., Seidel-Morgenstern, A. Numerical analysis of the preferential crystallization of enantiomers in complex flows (Poster). *12th International Workshop on Industrial Crystallization – BIWIC12*, ISBN 3-86010-797-6, pp. 165-172, Halle, Germany, September 7-9, 2005.
- [4] John, V., Angelov, I., **Öncül, A.A.**, Sundmacher, K., Thévenin, D. Towards the optimal reconstruction of a distribution from its moments (Poster). *AIChE Annual Meeting*, ISBN 0-8169-0996-2, Paper No: 287p, Cincinnati, USA, October 30-November 4, 2005.
- [5] **Öncül, A.A.**, Niemann, B., Thévenin, D., Sundmacher, K. CFD model of a semi-batch reactor for the precipitation of nanoparticles in the droplets of a microemulsion (Oral). *16th International Symposium on Computer Aided Process Engineering & 9th International Symposium on Process Systems Engineering – ESCAPE16 & PSE2006*, ISBN 978-0-444-52257-3, pp. 203-208, Garmisch-Partenkirchen, Germany, July 9-13, 2006.
- [6] Bordás, R., **Öncül, A.A.**, Zähringer, K., Thévenin, D. Optical measurements in two-phase flows involving particles (Oral). *12th International Symposium on Flow Visualization – ISFV12*, ISBN 0-9533991-8-4, Paper No: 25, Göttingen, Germany, September 10-14, 2006.
- [7] **Öncül, A.A.**, Thévenin, D., Sundmacher, K. Numerical simulation of BaSO₄ precipitation in a coaxial pipe mixer with micromixing effects (Oral). *AIChE Annual Meeting*, ISBN 0-8169-1012-X, Paper No: 70c, San Francisco, USA, November 12-17, 2006.
- [8] **Öncül, A.A.**, Kurt, T., Thévenin, D. Simulation of barium sulphate precipitation in a tubular reactor including micromixing effects (Oral). *6th International Conference on Multiphase Flow – ICMF 2007*, ISBN 978-3-86010-913-7, Paper No: S6_Wed_A_31, Leipzig, Germany, July 9-13, 2007.
- [9] **Öncül, A.A.**, El-Rabii, H., Thévenin, D. Prediction of soot formation in non-premixed flames using DQMOM (Oral). *6th International Conference on Multiphase Flow – ICMF 2007*, ISBN 978-3-86010-913-7, Paper No: S4_Fri_B_67, Leipzig, Germany, July 9-13, 2007.
- [10] Kurt, T., **Öncül, A.A.**, El-Rabii, H., Thévenin, D. Soot formation in non-premixed lifted flames predicted with moment-based methods (Oral). *23rd German Flame Day – Combustion and Furnaces*, Session IV_06, Berlin, Germany, September 12-13, 2007.
- [11] **Öncül, A.A.**, Thévenin, D. Influence of hydrodynamic conditions on particle size distribution (Poster). *6th European Congress of Chemical Engineering – ECCE6*, ISBN 978-87-91435-57-9, pp. Vol.2:229-230, Copenhagen, Denmark, September 16-20, 2007.
- [12] **Öncül, A.A.**, Thévenin, D. Einfluss der Partikelmorphologie auf die numerische Modellierung der BaSO₄-Fällung (Poster). *ProcessNet – Jahrestagung*, Paper No: P10.03, Aachen, Germany, October 16-18, 2007.
- [13] **Öncül, A.A.**, Thévenin, D., Genzel, Y., Reichl, U. Characterization of flow conditions in wave bioreactors using CFD (Oral). *7th European Symposium on Biochemical Engineering Science – ESBES-7*, Paper No: 1064, Faro, Portugal, September 7-10, 2008.
- [14] **Öncül, A.A.**, Thévenin, D., Kalmbach, A., Genzel, Y., Reichl, U. Flow characterization in wave bioreactors (Poster). *European BioPerspectives*, Paper No: 1063, Hanover, Germany, October 7-9, 2008.
- [15] **Öncül, A.A.**, Janiga, G., Thévenin, D. CFD analysis of the influence of mixing conditions on Particle Size Distributions in liquid-phase reactors (Oral). *ANSYS Conference & 26th CADFEM Users' Meeting 2008 – ACUM 2008*, ISBN 3-937523-06-5, Paper No: 2.3.4, Darmstadt, Germany, October 22-24, 2008.
- [16] **Öncül, A.A.**, Genzel, Y., Reichl, U., Thévenin, D. Flow characterization in wave bioreactors using Computational Fluid Dynamics (Poster). *21st Meeting of the European Society for Animal Cell Technology – ESACT-21*, Paper No: P187, Dublin, Ireland, June 7-10, 2009.
- [17] **Öncül, A.A.**, Thévenin, D., Kalmbach, A., Genzel, Y., Reichl, U. Numerical and experimental investigation of flow conditions in wave bioreactors (Oral). *27th DECHEMA Jahrestagung der Biotechnologen – DJB 2009*, Paper No: V11.08, Mannheim, Germany, September 8-10, 2009.
- [18] **Öncül, A.A.**, Genzel, Y., Reichl, U., Thévenin, D. Investigation of oxygen transfer process in wave bioreactors using Computational Fluid Dynamics (Oral). *5th International Berlin Workshop – IBW5*, Berlin, Germany, October 8-9, 2009.

-
- [19] **Öncül, A.A.**, Thévenin, D., Genzel, Y., Reichl, U. Flow characterization and two-population simulation in wave bioreactors using Computational Fluid Dynamics (Oral). *Vortrags- und Diskussionsstagung – Bioprozessorientiertes Anlagendesign*, Paper No: 1021, Nuremberg, Germany, May 10-12, 2010.
- [20] **Öncül, A.A.**, Thévenin, D., Genzel, Y., Reichl, U. Flow characterization and two-population CFD simulation in wave bioreactors (Poster). *8th European Symposium on Biochemical Engineering Science – ESBES-8*, Paper No: 9248, Bologna, Italy, September 5-8, 2010.
- [21] **Öncül, A.A.**, Janiga, G., Genzel, Y., Reichl, U., Thévenin, D. Two-population CFD simulation: microcarrier system for adherent cell growth in wave bioreactors (Poster). *4th International Conference on Population Balance Modelling – PBM 2010*, Paper No: 20, pp. 667-681, Berlin, Germany, September 15-17, 2010.
- [22] **Öncül, A.A.**, Bordás, R., Thévenin, D., Genzel, Y., Reichl, U. CFD modeling and validation of cell cultivation in wave bioreactors (Oral). *28th DECHEMA Jahrestagung der Biotechnologen – DJB 2010*, Paper No: 5042, Aachen, Germany, September 21-23, 2010.

D Curriculum vitae of A.A. Öncül

Personal information:

Date of birth: 23. February 1979
Place of birth: Ankara
Nationality: Turkish
Marital Status: Single

Professional practice:

08/2004 – 06/2010 **Research assistantship**
Laboratory of Fluid Dynamics and Technical Flows (LSS)
Otto-von-Guericke University (OvGU), Magdeburg/Germany

- Computational Fluid Dynamics, CFD
- Application of commercial CFD-Software
- Simulation of turbulent inhomogeneous flows
- Coupling of CFD with population balance models
- Numerous publications and conference contributions

11/2001 – 06/2002 **Student assistantship**
Institute of Particle Technology (LFG)
Friedrich-Alexander University (FAU), Erlangen/Germany

- Experiments on gas-solid flows in a fluidized bed

Education and training:

10/2002 – 01/2003 **Internship**
Main emphasis on thermal hydraulics and fluid mechanics
Framatome ANP GmbH, Erlangen/Germany

- Design of a high-pressure water-water vapor separator
- Analysis of mechanical strength of a high-pressure separator
- Simulation of acoustic disturbances in T-pipe employing Simulink

10/2001 – 03/2004 **Friedrich-Alexander University (FAU), Erlangen-Nuremberg/Germany**
Master of Science in Chemical Engineering

- Master thesis work on the topic “Experimental and numerical investigations and optimization of flow processes in radial porous burner”. (grade: 1.7 = good)
- Graduation grade: 1.8 = good

07/2000 – 08/2000 **Basic internship**
ÜLKER Food Industry Inc., Ankara/Turkey

- Training in research and development laboratory

- 09/1997 – 06/2001 **Middle East Technical University (METU), Ankara/Turkey**
Bachelor of Science in Chemical Engineering
- Graduation grade: 3.25 = honor degree
- 04/1996 – 02/1997 **High School, Çorum/Turkey**
- Graduation grade: 4.21 = good degree
- 09/1994 – 04/1996 **Science High School, Izmir/Turkey**

Advanced training:

- 07/2006 **International Center for Mechanical Sciences, Udine/Italy**
- Participation in the advanced course on topic “Computational Models for Turbulent Multiphase Reacting Flows”

Skills:

- Languages **Turkish:** native language
English: fluent in reading, writing and speaking
German: advanced knowledge
- Computer skills Expert in
- **CFD** applications (FLUENT, CFX)
 - **MS-DOS, Linux** and **Internet** applications
 - **Microsoft Office** applications (Word, Excel, Power Point, Outlook, Visio)
- Good knowledge in **MATLAB, Maple, Tecplot, C** and **FORTTRAN** applications
- Basic knowledge in **Aspen Plus** and **Simulink** applications